Disorder driven transitions in non-equilibrium quantum systems

Thesis by

Paraj Titum

In Partial Fulfillment of the Requirements for the
degree of
Doctor of Philosophy

CALIFORNIA INSTITUTE OF TECHNOLOGY
Pasadena, California

2016
Defended May 23, 2016

Paraj Titum
ORCID: [0000-0002-7792-1532]

ACKNOWLEDGEMENTS

This PhD would have not been possible without the support of a lot of people. First, I would like to thank my advisor Gil Refael. His support has been invaluable in my growth as a physicist. Second, I would like to thank my collaborators, Netanel Lindner, Victor Quito, Mikael Rechtsman, David Pekker, Mark Rudner, and Erez Berg. I had a lot of fun working with and learning from them. I would also like to acknowledge my fellow, present, and former graduate students and friends, Scott Geraedts, Karthik Seetharam, Min-Feng Tu, Kun-Woo Kim, Tejaswi Venumadhav, Dave Aasen, Shankar Iyer, and Christopher White. I enjoyed learning from the many discussions in various topics in physics. Outside of research, I would like to thank my invaluable friends who have helped me in many ways during my stay here.

Most importantly, I am grateful to my parents without whose support this endeavour would not have been possible.

ABSTRACT

This thesis presents studies of the role of disorder in non-equilibrium quantum systems. The quantum states relevant to dynamics in these systems are very different from the ground state of the Hamiltonian. Two distinct systems are studied, (i) periodically driven Hamiltonians in two dimensions, and (ii) electrons in a one-dimensional lattice with power-law decaying hopping amplitudes. In the first system, the novel phases that are induced from the interplay of periodic driving, topology and disorder are studied. In the second system, the Anderson transition in *all* the eigenstates of the Hamiltonian are studied, as a function of the power-law exponent of the hopping amplitude.

In periodically driven systems the study focuses on the effect of disorder in the nature of the topology of the steady states. First, we investigate the robustness to disorder of Floquet topological insulators (FTIs) occurring in semiconductor quantum wells. Such FTIs are generated by resonantly driving a transition between the valence and conduction band. We show that when disorder is added, the topological nature of such FTIs persists as long as there is a gap at the resonant quasienergy. For strong enough disorder, this gap closes and all the states become localized as the system undergoes a transition to a trivial insulator.

Interestingly, the effects of disorder are not necessarily adverse, disorder can also induce a transition from a trivial to a topological system, thereby establishing a Floquet Topological Anderson Insulator (FTAI). Such a state would be a dynamical realization of the topological Anderson insulator. We identify the conditions on the driving field necessary for observing such a transition. We realize such a disorder induced topological Floquet spectrum in the driven honeycomb lattice and quantum well models

Finally, we show that two-dimensional periodically driven quantum systems with spatial disorder admit a unique topological phase, which we call the anomalous Floquet-Anderson insulator (AFAI). The AFAI is characterized by a quasienergy spectrum featuring chiral edge modes coexisting with a fully localized bulk. Such a spectrum is impossible for a time-independent, local Hamiltonian. These unique characteristics of the AFAI give rise to a new topologically protected nonequilibrium transport phenomenon: quantized, yet nonadiabatic, charge pumping. We identify the topological invariants that distinguish the AFAI from a trivial, fully localized

phase, and show that the two phases are separated by a phase transition.

The thesis also present the study of disordered systems using Wegner's Flow equations. The Flow Equation Method was proposed as a technique for studying excited states in an interacting system in one dimension. We apply this method to a one-dimensional tight binding problem with power-law decaying hoppings. This model presents a transition as a function of the exponent of the decay. It is shown that the the entire phase diagram, i.e. the delocalized, critical and localized phases in these systems can be studied using this technique. Based on this technique, we develop a strong-bond renormalization group that procedure where we solve the Flow Equations iteratively. This renormalization group approach provides a new framework to study the transition in this system.

PUBLISHED CONTENT AND CONTRIBUTIONS

[1] Paraj Titum et al. "Anomalous Floquet-Anderson Insulator as a Nonadiabatic Quantized Charge Pump." In: *Phys. Rev. X* 6 (2 May 2016), p. 021013. DOI: 10.1103/PhysRevX.6.021013.
PT participated in the conception of the project, contributed with the required analytical and numerical techniques associated with it, and participated in the writing of the manuscript.

[2] Paraj Titum et al. "Disorder-Induced Floquet Topological Insulators." In: *Phys. Rev. Lett.* 114 (2015), p. 056801. DOI: 10.1103/PhysRevLett.114.056801.
PT participated in the conception of the project, contributed with the required analytical and numerical techniques associated with it, and participated in the writing of the manuscript.

CONTENTS

LIST OF FIGURES

LIST OF TABLES

Part I

Introduction

Chapter 1

DISORDERED QUANTUM SYSTEMS

The role of disorder in condensed matter systems has been a topic of research for over half a century. In experiments, it is never possible to have a completely clean sample. Disorder may be present in a material due to imperfections in an ideal lattice or through the presence of impurity atoms or dislocations. In order to study the low temperature quantum phases in these materials, it becomes necessary to account for the effects of disorder.

Let us consider the example of a metal. What role does disorder play in determining the electronic properties of a metal? As we will describe in the Sections 1.1 and 1.3, the perturbative effects of disorder lead to corrections to the density of states at the Fermi energy and transport parameters such as conductance. These corrections are universal, depending only on the symmetries and the dimensionality of the system. However, strong disorder can drastically change the properties of the system. It may lead to a metal-to-insulator phase transition (MIT). Such an insulating phase due to the presence of disorder is called an Anderson insulator.

Anderson insulators do not conduct due to the phenomenon of localization, which was first pointed out by Anderson [4]. Classically, a particle moves diffusively in the presence of a set of random impurities. For example, electrons in a disordered metallic system undergo diffusive transport. However, when one considers an electron in the presence of a disorder, quantum-interference effects may lead to exponentially localized states. The wave-functions of such localized states are peaked at random sites. Naturally, these states do not conduct. Diffusion in such a material is absent giving rise to insulating behavior.

Anderson insulators have several characteristic properties which we elaborate in Section 1.2. Band insulators do not conduct because the fermi energy lies in the gap between valence and conduction bands. Unlike band insulators, Anderson insulators do not have a gap in the density of states. Instead, the density of states of generic disordered systems have localized and extended states separated by a critical state, which is defined as the mobility edge. Therefore, one can define a notion of a mobility gap in disordered systems, which is the energy difference between two mobility edges. The concept of mobility gaps is essential when studying the nature

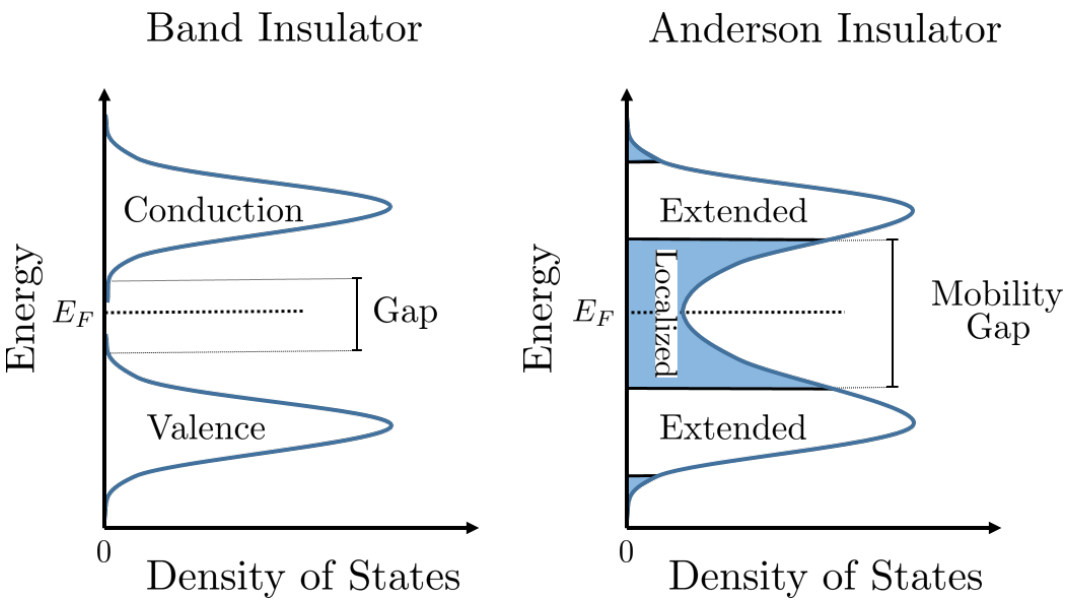

Figure 1.1: Schematic Density of States (DOS) of a band insulator and Anderson Insulator. The DOS of band insulators consists of two bands with a gap where there are no states. In contrast, Anderson insulators generically have no gap in the density of states. The DOS is split into 'bands' of extended and localized states separated by mobility edges. The system is insulating as long as the Fermi energy is in the localized band. When there are multiple bands of extended states, one can define a mobility gap which is the separation between the extended states.

of bulk states in disordered insulators.

In the following chapters we study the effect of disorder on a variety of driven systems. The model for disorder is a random potential in position space, $\mathbf{x}$. The disorder potential, $V_{\rm dis}(\mathbf{x})$ is a randomly distributed potential. Universal properties of the system are extracted from averaging quantities of physical interest over an ensemble of disorder configurations. We choose the disorder potential to be a random on-site energy, $V_{\rm dis}(\mathbf{x})$, with the following statistics,

$$\begin{aligned} \overline{V_{\rm dis}(\mathbf{x})} &= 0, \\ \overline{(V_{\rm dis}(\mathbf{x}))^2} &= \sigma_{\rm dis}^2, \\ \overline{V_{\rm dis}(\mathbf{x})V_{\rm dis}(\mathbf{x}')} &= \sigma_{\rm dis}^2\delta(\mathbf{x}-\mathbf{x}'), \end{aligned} \tag{1.1}$$

where $\overline{(\cdots)}$ indicates averaging over the probability distribution of the disorder potential, and $\sigma_{\rm dis}^2$ is the variance of the distribution of the disorder potential. In the numerical treatments that follow, we choose the probability distribution of the disorder to be uniformly distributed, $[-U_0/2, U_0/2]$, with $\sigma_{\rm dis}^2 = U_0^2/12$. In the definition of the disorder potential in Eq. (1.1), we choose δ-correlated disorder.

In general, all the phenomenon we describe will not be dependent on the type of correlation as long as the correlation remains short ranged. In Part III, we introduce disorder in the hoppings on a one-dimensional lattice. In that case, we discuss the effects of long-range disordered hoppings.

The chapter is organized as follows. In Section 1.1, we introduce the Born approximation to compute the perturbative corrections to density of states. In Section 1.2, we discuss the localization in disordered systems. We elaborate the different diagnostics to explore the Anderson insulating phase. In Section 1.3 we discuss the transition from metallic to localized states and its dependence on dimensionality and symmetry.

1.1 Born approximation

In this section, we calculate the single particle density of states of a disordered system perturbatively to second order in the disorder potential. A single impurity disorder configuration breaks translation symmetry in the system. However, averaging over an ensemble of disorder configurations restores the translation symmetry in the system.

Consider a system in the absence of disorder. The Hamiltonian for such a system has translation symmetry which allows us to transform to momentum space. Assume that the Hamiltonian is $H_0(\mathbf{k})$, where $\mathbf{k}$ denotes the crystal momentum. Given that the Hamiltonian, has an energy dispersion $\epsilon_{\mathbf{k}}$, we can define the bare Green's function,

$$G_0(E, \mathbf{k}) = \frac{1}{E - \epsilon_{\mathbf{k}}}, \tag{1.2}$$

where E denotes the energy. In real space, the bare Green's function connecting two points, $\mathbf{x}$ and $\mathbf{x}'$ is only a function of $(\mathbf{x} - \mathbf{x}')$, $G_0(E, \mathbf{x}, \mathbf{x}') \equiv G_0(E, \mathbf{x} - \mathbf{x}')$. The real-space and momentum space definitions of G_0 are related by a Fourier transform,

$$G_0(E, \mathbf{x} - \mathbf{x}') = \int \frac{d\mathbf{k}}{(2\pi)^d} G_0(E, \mathbf{k}) e^{i\mathbf{k}\cdot(\mathbf{x}-\mathbf{x}')}, \tag{1.3}$$

where d denotes the number of dimensions in real-space.

Now, consider the effect of the disorder potential, $V_{\mathbf{dis}}(\mathbf{x})$. In the presence of disorder potential, the translation symmetry is broken. The single particle propagator in real space must depend on both position variables, $\mathbf{x}$ and $\mathbf{x}'$. In Fig. 1.2 (a), we represent the bare and full propagators in real space as a thin and thick line respectively. It is expected that the translation symmetry is recovered by averaging over an ensemble of disorder realizations. Let us obtain the self-energy contribution due to disorder

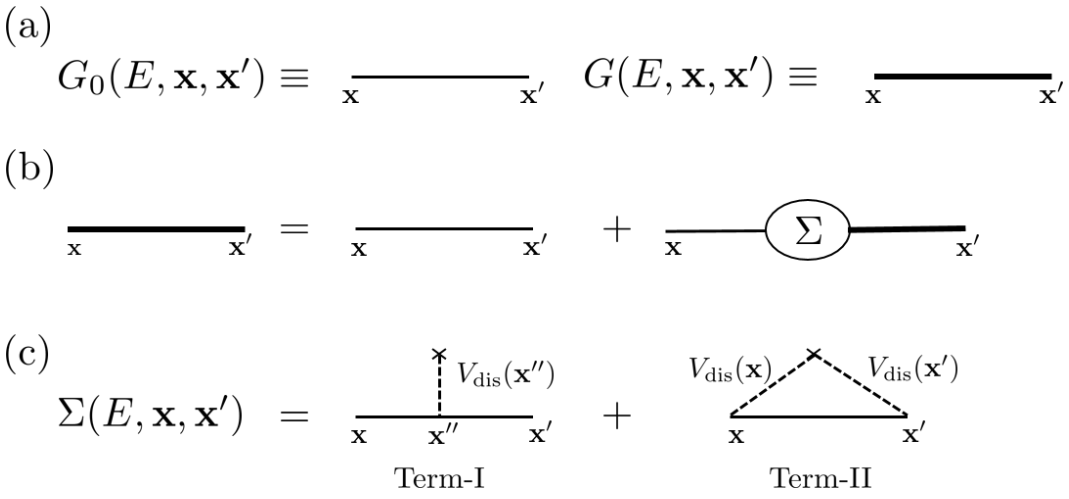

Figure 1.2: Figure shows the Feynman diagrams associated with disorder potential. (a) Schematic representation in real-space for the bare Green's function, $G_0(E, \mathbf{x}, \mathbf{x}')$, and full Green's function $G(E, \mathbf{x}, \mathbf{x}')$. (b) Representation of the Dyson equation using Feynman diagrams, as represented in Eq. (1.4). (c) Contributions to the self-energy, $\Sigma(E, \mathbf{x}, \mathbf{x}')$ to second order in the disorder potential $V_{\rm dis}(\mathbf{x})$.

potential on the disorder-averaged Green' functions. The Dyson equation for the propagator in real space is,

$$G(E, \mathbf{x}, \mathbf{x}') = G_0(E, \mathbf{x}, \mathbf{x}') + \sum_{\mathbf{x},\mathbf{x}'} G_0(E, \mathbf{x}, \mathbf{x}'')\Sigma(E, \mathbf{x}'', \mathbf{x}''')G(E, \mathbf{x}''', \mathbf{x}'), \tag{1.4}$$

where $\Sigma(\mathbf{x}, \mathbf{x}')$ is the self energy correction due to disorder and E is the energy. The contributions to the self-energy to second order in the disorder potential are shown in Fig. 1.2 (c). As shown in the figure, there are two terms in the self-energy correction,

$$\Sigma(E, \mathbf{x}, \mathbf{x}') = \Sigma^{(I)}(E, \mathbf{x}, \mathbf{x}') + \Sigma^{(II)}(E, \mathbf{x}, \mathbf{x}') \tag{1.5}$$

$$\text{Term-I } : \Sigma^{(I)}(E, \mathbf{x}, \mathbf{x}') = G_0(E, \mathbf{x}, \mathbf{x}'')\overline{V_{\rm dis}(\mathbf{x}'')}G_0(E, \mathbf{x}, \mathbf{x}'), \tag{1.6}$$

$$\text{Term-II } : \Sigma^{(II)}(E, \mathbf{x}, \mathbf{x}') = \overline{V_{\rm dis}(\mathbf{x})V_{\rm dis}(\mathbf{x}')}G_0(E, \mathbf{x}, \mathbf{x}') = \Sigma(E, \mathbf{x} - \mathbf{x}'), \tag{1.7}$$

where we have averaged over the distribution of the disorder potential, $V_{\rm dis}(\mathbf{x})$. In Eq. (1.7), we have utilized the property of the the correlation of the disorder potential (see Eq. (1.1)) to recover translation symmetry, $\Sigma^{(II)}(E, \mathbf{x}, \mathbf{x}') \equiv \Sigma^{II}(E, \mathbf{x} - \mathbf{x}')$. Furthermore, Term-I is vanishing because the average of the disorder potential is assumed to be zero. If the disorder potential has a non-zero expectation value, Term-I will be non-zero. However, this term has no observable consequences, as it can be removed by shifting the reference for measuring energy. Therefore, Term-II

is the lowest order contribution in the disorder potential to the self energy. Now, using Eqs. (1.7) and (1.1), the self-energy in momentum space becomes

$$\Sigma(E, \mathbf{k}) = \sigma_{\text{dis}}^2 \int \frac{d\mathbf{k}'}{(2\pi)^d} G_0(E, \mathbf{k}'), \tag{1.8}$$

where the self energy is independent of momentum, $\mathbf{k}$, because of the choice of δ-correlation in the disorder potential.

The self-energy correction in general in complex valued. Let us write the self-energy as a sum of real and imaginary parts, $\Sigma = \text{Re}(\Sigma) + i\,\text{Im}(\Sigma)$. The imaginary part is related to the momentum relaxation time, τ, $\text{Im}(\Sigma) = -1/(2\tau(E, \mathbf{k}))$. The momentum relaxation time is the time-scale denoting that the impurity averaged propagator decays exponentially, $G(E, \mathbf{x} - \mathbf{x}') \sim \exp(-|\mathbf{x} - \mathbf{x}'|/(2l))$, where the length scale $l \propto \tau$, is the mean free path. The real part of the self-energy renormalizes the dispersion relation. It is defined as

$$\text{Re}(\Sigma) = P\left[\sigma_{\text{dis}}^2 \int \frac{d\mathbf{k}'}{(2\pi)^d} G_0(E, \mathbf{k}')\right], \tag{1.9}$$

where P denotes the Cauchy principal value of the integral. In the following chapters, we will chiefly be interested in band insulating Hamiltonians which have sub-lattice or pseudospin degree of freedom. In these systems, the real part of the self-energy determines the corrections to the parameters of the Hamiltonian.

So far, we studied the effects of disorder on the single-particle density of states. The real part of the self energy renormalizes the spectrum of the Hamiltonian. The imaginary part of the self-energy is related to the mean-free time at a particular disorder strength. How does disorder modify the transport properties of the system? To analyze this, we must go beyond single particle Green's functions. In the following section, we discuss the effects of strong disorder on the conductance of the material.

1.2 Localization due to disorder.

One of the striking effects of disorder is to exponentially localize the wavefunctions of a material. It was first pointed out by Anderson [4], that in the presence of disorder in certain random lattices, it is possible to prevent diffusion of electrons across the system. This is because the electron wavefunctions, $\psi(\mathbf{x})$ are localized in the position basis,

$$\psi(\mathbf{x}) \sim \exp(-|\mathbf{x}|/\xi) \tag{1.10}$$

where ξ denotes the localization length. The localization length depends on the strength of disorder of the system.

Numerically, it is convenient to consider the Hamiltonian in the position basis. The spectrum and eigenfunctions are obtained by exactly diagonalizing the Hamiltonian. There are several ways to infer the localized nature of an eigenfunction at a particular energy. In the following, we summarize some of the properties that distinguish localized states from extended states.

1. **Inverse Participation Ratio (IPR)** : The inverse participation ratio is defined as the second moment of the probability density. Consider a wavefunction, $\psi(\mathbf{x})$. The generalized inverse participation ratio is

$$P_q = \sum_{\mathbf{x}} |\psi(\mathbf{x})|^{2q}, \tag{1.11}$$

   where q defines the order of the moment. Note that $P_1 = 1$ as the wavefunction is normalized. For most cases, we are interested in the second moment and therefore, set $q = 2$. The IPR measures a length scale characterizing the region in real-space where $|\psi(x)|$ differs markedly from zero. The scaling of IPR with system size, L reveals the localized or delocalized nature of the wavefunction, $P_q \sim L^{-D_q(q-1)}$. The dimension D_q is known as the fractal dimensionality of the state and it depends on the nature of the wave-function. When the wavefunction is delocalized, $P_2 \sim L^{-d}$, so that $D_q = d$. On the other hand, $D_q = 0$ when it is localized, because the localization length is much smaller than the system size, $\xi \ll L$. Remarkably, at the critical point of the transition from localized to delocalized, the fractal dimension is in general less than the Eucledian dimensions, $D_q = d_c \leq d$.

2. **Transmission probability** : The probability of transmission of an electron with energy E, from site $\mathbf{x}$ to $\mathbf{x}'$ is defined as

$$t(E, \mathbf{x}, \mathbf{x}') = \overline{|G(E, \mathbf{x}, \mathbf{x}')|^2}, \tag{1.12}$$

   where $G(E, \mathbf{x}, \mathbf{x}')$ is the Green's function for the disordered system as defined in Eq. (1.4). The transmission probability for a localized system must decay exponentially with distance with a length scale proportional to the localization length, $t(E, \mathbf{x}, \mathbf{x}') \sim \exp(-2|\mathbf{x} - \mathbf{x}'|/\xi)$. The transmission probability is important because it is proportional to the dc conductance of the sample.

3. **Level spacing statistics** : The statistics of adjacent level spacings have distinctive behavior in localized and extended phases. While generic extended eigenstates cannot be degenerate since they experience level repulsion, localized states far from each other can be arbitrarily close to each other in energy. This leads to different behaviors in the distributions of the level-spacings at these energies. This distinction in the level-spacing statistics is used to distinguish between extended and localized states.

   Let us consider the eigenvalues of the Hamiltonian as an ordered list indexed by n, $\{\epsilon_n\}$. The level-spacing, s_n, is defined as the difference of adjacent energies, $s_n = \epsilon_{n+1} - \epsilon_n$. Let the average level spacing over all energies and disorder realizations be δ. We now define level-spacing at a given energy, measured in units of δ, $s(\epsilon) = \frac{1}{\delta} \sum_{n,|\epsilon_n - \epsilon| \leq d\epsilon} s_n$, where we choose the window of energy such that $d\epsilon \gg s_n$. For localized states, the level-spacings must follow Poisson statistics [79],

$$P_{\text{loc}}(s) = \exp(-s). \tag{1.13}$$

   Clearly, $\lim_{s\to 0} P(s)ds$ is non-zero. This non-zero probability density of zero spacing is an indication of degenerate eigenvalues in the thermodynamic limit. This means that these states do not repel and this is a signature that the states at this energy are localized.

   Extended states experience level repulsion which means that $P(s)$ must vanish as s vanishes because extended states cannot occur arbitrarily close to another extended state. In fact, $\lim_{s\to 0} P(s) \propto s^{\theta}$, where θ is determined by the symmetries of the Hamiltonian. The symmetries determine the ensemble of random matrices to which the Hamiltonian belongs. Such random matrices were classified by Dyson [20] and further extended by Altland and Zirnbauer [3]. In the next section, we discuss the symmetry classification of random matrices and its consequence on localization.

   In this section we outlined several different diagnostics for detecting localized states. IPR requires the knowledge of eigenfunctions. In contrast, the level spacing statistics is more numerically efficient for detecting localized and extended phases. There are efficient numerical techniques to obtain the transmission probability. We compute numerically the propagator in real space through a real-time evolution which we discuss in Part-II.

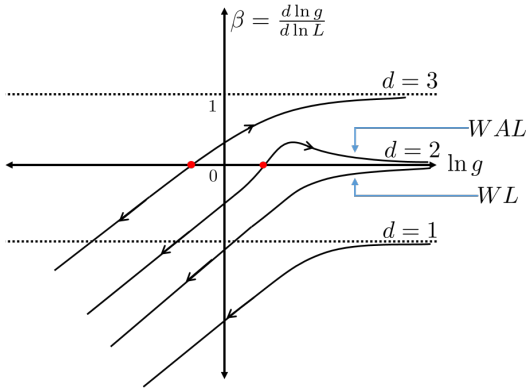

Figure 1.3: Abrahams et al. [1] formulated the scaling theory of localization. Renormalization group flows of the β function for the zero temperature conductance of a disordered system with dimensionality $d = 1$, 2 and 3. Here, $d = 2$ is the lower critical dimension and there are two possible cases depending on the sign of β in the metallic limit: (i) Weak Localization (WL, $\beta \to 0^-$ as $g \to \infty$) and (ii) Weak Anti-Localization (WAL, $\beta \to 0^+$ as $g \to \infty$). The fixed point at $\beta = 0$ defines the critical point corresponding to the Anderson transition. These are shown as red circles. Systems exhibiting WAL must undergo an Anderson transition at some critical disorder strength.

1.3 The localization transition

Is the metal to insulator transition due to disorder a quantum phase transition? Abrahams et al. [1] proposed a one-parameter renormalization group approach to study disordered systems. This scaling picture of localization provides a phenomenological setup to understand the localization transition. The relevant parameter in the flow is postulated to be the average conductance (g) of the sample. The finite size scaling of the conductance is different in the metallic (classical Ohmic) and insulating regimes,

$$g \sim \sigma L^{d-2} \qquad \text{when metallic,} \tag{1.14}$$

$$g \sim \exp(-2L/\xi) \text{ when insulating,} \tag{1.15}$$

where σ denotes the conductivity of the material and L is the system size taken as a hypercube of volume L^d. Now, we can define the β function for the scaling variable, g,

$$\beta(g) = \frac{d \ln g}{d \ln L} \sim \begin{cases} d-2, & \text{when metallic, i.e. } g \to \infty \\ \ln g, & \text{when insulating, i.e. } g \to 0. \end{cases} \tag{1.16}$$

The schematic flow diagram is shown in Fig. 1.3, where we plot the dependence of the β function on $\ln g$. The asymptotic behavior of the β function is described

by Eq. (1.16). When the system is metallic, conductance is large, which means that when $\ln g \to \infty$, the β function is a constant. When a sample is insulating, conductance is vanishing. Therefore, when $\ln g \to -\infty$, the β function must be a straight line with a positive slope.

The β function, which gives the flow as g as L is changed, is shown in Fig. 1.3. Consider the flow of β as the system size is increased. If $\beta > 0$ ($\beta < 0$), the conductance must increase (decrease) flowing to a metallic (insulating) phase in the thermodynamic limit. The critical point for the transition occurs when the system is scale invariant, at $\beta(\ln g_c) = 0$. Clearly, the fixed point of the β function is unstable.

One of the predictions of this theory is the strong dependence of localization on the dimensionality of the sample. As seen in Fig. 1.3, for dimensions, $d < 2$, there is no critical point for an Anderson transition. This means that even for infinitesimal disorder, all eigenfunctions of the system are localized. On the other hand, for $d = 3$, there must be a localization transition with distinctive metallic and insulating phases. The one-parameter scaling theory has been verified numerically [57, 77].

Two dimensions is the marginal case for the one-parameter scaling theory. It is impossible to tell if there is a transition or not without further information. In the classical limit, β function vanishes in the metallic limit as expected from Eq. (1.16). Therefore, the sign of the lowest order corrections to the in the metallic phase are important. These determine the nature of states in the disordered system. The two distinct cases corresponding to the sign of the β function in the metallic limit are

$$\lim_{g\to\infty} \beta(g) = \begin{cases} 0^-, & : \text{Weak Localization (WL)}, \\ 0^+, & : \text{Weak Anti-localization (WAL)}. \end{cases} \tag{1.17}$$

The sign of the β function also determines whether there exists a critical point as shown in Fig. 1.3. In WL systems, $\beta < 0$ for all disorder strengths. Therefore the phase is localized for any finite disorder. On the other hand, WAL systems must cross $\beta = 0$ for some critical disorder strength. Therefore, generic WAL systems exhibit a localization transition even in two dimensions.

The phenomena of Weak Localization (WL) and Weak Anti-Localization (WAL) can be understood from the perturbative corrections by disorder. The sign of this correction to the conductance determines the sign of the β function. Intuitively, the correction is due to quantum interference effects on the return probability of the electron scattering through the disordered medium. The return probability of an electron is obtained from the transmission probability, $t(E, \mathbf{x}, \mathbf{x})$ (defined in Section 1.2). The

Class	Time-reversal	Spin rotation	θ	A_θ	B_θ
Orthogonal (GOE)	✓	✓	1	$\frac{\pi}{2}$	$\frac{\pi}{4}$
Unitary (GUE)	✗	NA	2	$\frac{32}{\pi^2}$	$\frac{4}{\pi}$
Symplectic (GSE)	✓	✗	4	$\frac{2^{18}}{3^6\pi^3}$	$\frac{64}{9\pi}$

Table 1.1: Classification of the different Random matrix ensembles as first proposed by Wigner and Dyson [20, 115]. The classification is based on the symmetries of the random matrix: Time reversal (T) and spin-rotation (S). We also list the parameter θ that uniquely identifies the ensembles, and the level spacing statistics ($P(s)$ defined in Eq. (1.18).

non-zero contributions to the return probability comes from self-intersecting paths and their corresponding time-reversed partners. Clearly, the presence or absence of time-reversal symmetry becomes important. In the presence of time-reversal symmetry, the contributions from both these paths may either constructively or destructively interfere depending on the phase difference between the two paths. A constructive interference corresponds to a higher return probability. This leads to localization and a negative correction to the conductance. This phenomenon is termed as Weak Localization. In contrast, destructive interference corresponds to lower return probability and leads to delocalization. This case corresponds to Weak Anti-Localization. In physical systems, the phase-difference between the two paths can be tuned using a magnetic field. When time-reversal symmetry is present, spinless systems are expected to be WL and systems with spin-orbit coupling are WAL. The spin-orbit coupling can be viewed as an effective magnetic field for the electron. This means that in order for a system to have delocalized states in two dimensions, the spin-rotation symmetry must be broken.

Symmetry plays an important role in determining the nature of the delocalized metallic states, as evidenced by the drastically different behaviors of disordered systems in two dimensions. The general classification of random matrices into distinct invariant ensembles on the basis of symmetry was done by Wigner and Dyson [20, 115]. The different ensembles of random matrices are based on the presence or absence of time-reversal (T) and spin-rotation (S) symmetry. The three ensembles are (i) Gaussian Unitary Ensemble (breaks T, S is irrelevant), (ii) Gaussian Orthogonal Ensemble (respects both T and S), and (iii) Gaussian Symplectic Ensemble(respects T, breaks S). Some properties of the ensembles are listed in Table 1.1. The general properties of the eigenvalues of disordered Hamiltonians (in

the delocalized phase) can be understood from this classification. For example, the energy levels corresponding to delocalized states of a disordered Hamiltonian have 'level repulsion'. This is because it is impossible for two delocalized states to have the same energy, unless the degeneracy is protected by some symmetry. This level repulsion among nearly degenerate levels can be obtained from the random matrix ensemble corresponding to the same symmetries of the Hamiltonian.

The repulsion among the eigenvalues puts constraints on the form of the level-spacing statistics. As we discussed in Section 1.2, localized levels do not have any repulsion and therefore, must obey Poisson statistics. In comparison, extended states of disordered systems must repel. Wigner postulated that the level-spacing statistics of the random matrices can be approximated by

$$P_\theta(s) = A_\theta s^\theta \exp\left(-B_\theta s^2\right), \tag{1.18}$$

where $\theta = 1, 2, 4$ corresponding to Orthogonal, Unitary or Symplectic ensembles respectively. The constants $A(\theta)$ and $B(\theta)$ are determined from normalization of the distribution and mean spacing to 1. The exact values of these coefficients for the different ensembles are shown in Table 1.1. Comparing $P(s)$ in Eqs. (1.13) and (1.18), we see that the level spacing distribution is drastically different. For the delocalized states, the level spacing distribution is vanishing, $\lim_{s\to 0} P(s) \sim s^\theta$.

1.4 Summary

In this chapter, we discussed the emergence of Anderson localization in strongly disordered systems and various methods to characterize it. The physical dimensions and symmetries play a crucial role in determining the nature of states in disordered systems. For example, no localization transition exists for disordered systems in one dimension. The lower critical dimension for the metal to insulator transition is two. In two dimensions, the presence or absence of spin-rotation and time-reversal symmetry determines if a metallic phase is stable to infinitesimal disorder. Delocalized states of disordered Hamiltonians have identical statistical properties to invariant ensembles of random matrices. The symmetries of the Hamiltonian determine the exact statistics of the eigenvalue spacings.

In Part II and Part III we discuss the effects of disorder on two independent classes of systems. In Part II, we study the effects of disorder in driven topological phases, and the role of Anderson localization in these systems. We will chiefly be interested in Hamiltonians in two dimensions. So, as discussed in this chapter, the symmetries

of the Hamiltonian will determine the properties of the delocalized states. In Part-part:WegnerFlow, we study an Anderson transition in one dimension in the presence of long range power-law hoppings. By introducing long range hoppings, we bypass the constraint from the scaling picture that there is no localization transition in one dimension. This is because the scaling picture presented here is only valid for electrons with short range hopping.

Chapter 2

TOPOLOGY IN QUANTUM SYSTEMS

The classification of different phases of matter is one of the fundamental problems in condensed matter physics. The conventional classification scheme is based on symmetries of the Hamiltonian describing the system. This theory was proposed by Landau and it is successful in explaining a large class of classical phases and phase transitions. For example, a classical magnet may be in either a ferromagnetic or a paramagnetic phase. These two phases have different behavior under spin rotation symmetry. While a paramagnet is rotationally symmetric, a ferromagnet spontaneously breaks the rotation symmetry. A critical point separates the two phases and has universal properties determined by the symmetries and dimensionality of the system.

What is a quantum phase and how do we distinguish it from other quantum phases? At zero temperature, a quantum phase corresponds to the ground state of the Hamiltonian. Depending on the system, the low energy excitation spectrum maybe gapped or gapless. We will be concerned with insulating systems only. In the following, we describe the general classification of bulk gapped quantum phases. Let us consider two Hamiltonians with a different set of parameters. Naturally, the corresponding ground states are functions of these parameters. These two states describe the same phase, if one ground state is adiabatically connected to the other by a smooth variation of the parameters. This adiabatic path in the parameter space connecting the two states is well defined only when the gap between the ground state and the first excited state never closes along the path. Conversely, if two quantum phases are distinct, it is not possible to connect the two phases without closing the gap at some point in the parameter space. This gapless state is the critical point that separates the two phases. This discussion can be generalized to phases that are protected by a particular symmetry. In this case, the two states are distinct only in the presence of that symmetry. Such phases are labelled symmetry protected phases.

The notion of symmetry breaking from Landau theory can also be extended to quantum phases. For example, analogous to classical magnetism, there are different zero-temperature quantum phases in quantum magnets. However, not all quantum phases of matter can be classified by symmetry. This fact was realized after the

discovery of the integer quantum Hall effect by Klitzing et al. [54]. They measured a quantized Hall response in a two-dimensional electron gas in the presence of a very strong magnetic field and low temperatures. The Hall conductance develops plateaus with integer quantization as a function of magnetic field as shown in Fig. 2.1. As we explain in Section 2.1, these plateaus correspond to different quantum phases even though there is no distinction between them on the basis of symmetry

In quantum Hall effect and more generally in topological materials, different phases having the same set of symmetries may have very different 'topological' properties. These are global properties of the ground state wavefunction such as a topological invariant computed by integrating over the first Brilluoin zone (FBZ). In the following sections we discuss three different examples of non-interacting topological phases and the invariants associated with them. It is impossible to connect two ground states with different values of the topological invariant without closing the gap. Therefore, phases corresponding to different values of the invariant are distinct phases of matter. Consequently, small local perturbations cannot change the nature of the topological phase. This leads to a robustness of the phase to local disorder potential. A topologically trivial phase corresponds to the state that is featureless and can be deformed continuously to the trivial vacuum.

Topological phases of matter may have exotic properties such as boundary states or fractional excitations. In the non-interacting topological phases we describe, a non-trivial phase implies the presence of a boundary mode. The details of the type of boundary mode depends on the symmetries and the physical dimensions of the system. For example, at the boundary of integer quantum Hall states, there exists charged chiral edge states. Other topological phases such as, topological insulators have counterpropagating helical edge states with opposite spin but the same charge. The presence of boundary modes can be traced back to the presence of a quantum anomaly. The bulk theory is anomalous when one tries to define it in a geometry with a boundary [116].

The classification of non-interacting topological phases of matter in different dimensions and symmetries was done by Kitaev [51], Schnyder et al. [97] and Ryu et al. [96]. The 'periodic' table of topological phases, gives the classification of phases on the basis of topology given the dimensions and the presence or absence of different symmetries such as time-reversal, sublattice and particle-hole conjugation. The different classes correspond to tenfold classification of Altland and Zirnbauer for random matrices [3]. Dimensions play an important role in determining the

topological invariant classifying all non-trivial phases.

In this chapter, we describe three different examples of non-interacting topological phases. We start by introducing the integer quantum Hall effect in Section 2.1. In Section 2.2, we introduce the Haldane model for anomalous quantum Hall effect on the honeycomb lattice. This model realizes the Chern insulator phase, which is the lattice analog of the quantum Hall effect without any external magnetic field. Finally in Section 2.3, we discuss the case of time-reversal invariant topological insulators.

2.1 Integer quantum Hall effect

The integer quantum Hall effect is a manifestation of quantum effects in two dimensions, in the presence of strong magnetic fields and low temperatures. The Hall measurement is used to characterize transport of two-dimensional electron gas (2DEG) in a magnetic field. The set up is schematically shown in Fig. 2.1 (a). Current passes through the sample in the x direction. The presence of a magnetic field in the z direction, induces a voltage in the y direction, the Hall voltage, V_H. Therefore, in this four terminal set up, conductance in the longitudinal (σ_{xx}) and transverse (σ_{xy}) directions can be measured as a function of the magnetic field.

In the classical Hall set up, $\sigma_{xy} = \rho c/B$ where ρ denotes the charge density in the material and c is the speed of light. Conversely, the Hall resistance is proportional to the magnetic field. However, at strong magnetic fields and low temperatures, the Hall conductance behaves in a drastically different way. Experiments conducted by Klitzing et al. [54] showed that the Hall resistance is quantized. As shown in Fig. 2.1, the Hall resistance has plateaus as a function of magnetic field, at values, $R_H = h/(\mathrm{i}e^2)$, where i is an integer. The precise quantization of the Hall plateaus is due to single particle quantum mechanics of an non-relativistic electron gas in a magnetic field. The 2DEG energy spectrum rearranges into highly degenerate Landau levels, indexed by integer i. When the fermi-energy is in the gap between two Landau levels, i and i + 1, the bulk of the 2DEG is gapped and insulating. However, the Landau levels must distort at the boundaries. This gives rise to gapless edge states carrying current and a quantized Hall conductance ($\sigma_H = \mathrm{i}e^2/h$).

The quantization of the Hall conductance in a more general setup without assuming translation symmetry, was shown by Laughlin [62] and Halperin [36]. Consider the Hall setup in a cylindrical geometry, with periodic boundary condition along x direction and open boundary conditions along y. The Hall conductance is propor-

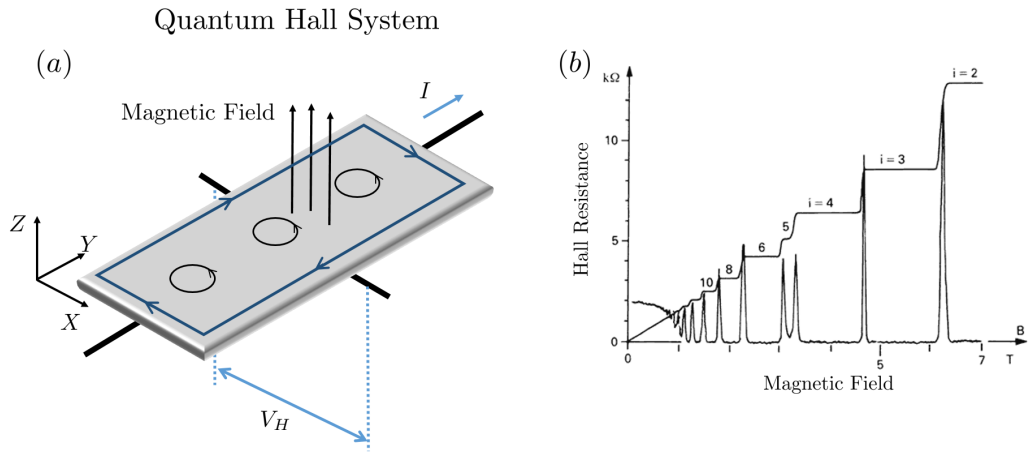

Figure 2.1: The quantum Hall effect. (a) Schematic set up for the quantum Hall effect. V_H is the Hall voltage, from which the Hall resistance is obtained. (b) Shows the experimental measurement of Hall resistance which plateaus at $h/(ie^2)$. The plateaus are for i=2, 3, 4, 5, 6, 8, and 10 [54]

tional to the number of charges pumped across the cylinder along y direction as a twist (by introducing a fictitious flux) is introduced to the boundary condition along x . Since the number of charges are quantized to an integer, the Hall conductance must be quantized.

The quantization of Hall conductance shown by Laughlin [62] and Halperin [36] relies on specific boundary conditions. The connection between the quantum Hall effect and topology of the bulk wavefunctions was shown by Thouless, Kohmoto, Nightingale, and de Nijs [107]. They computed the bulk conductance of a lattice in a commensurate magnetic field using the Kubo formula. Consider occupied bands indexed by j with Bloch wavefuctions, $u_j(\mathbf{k})$. The Hall conductance is

$$\sigma_{xy} = \frac{e^2}{h}\sum_j n_j, \tag{2.1}$$

$$n_j = \frac{i}{2\pi}\int dk_x dk_y(\langle\partial_{k_x}u_j|\partial_{k_y}u_j\rangle - \langle\partial_{k_y}u_j|\partial_{k_x}u_j\rangle), \tag{2.2}$$

where in Eq. (2.2), the k_x and k_y is integrated over the first Brilluoin zone. The expression for n_i is a topological invariant, the Chern number (C) which is restricted to integer values. Clearly, the Hall response of the bulk wavefunction is quantized as shown in Eq. (2.1), which is the same behavior seen in a Hall conductance measurement.

The quantum Hall effect is a state exhibiting bulk-boundary correspondence. This

is a feature shared by many non-interacting topological phases. At the boundary of two topological phases with different 'bulk' topological invariants, there must exist gapless edge states. Consider an interface of $i = i_1$ and $i = i_2$ quantum Hall plateaus. At the boundary of these two states, precisely $|i_1 - i_2|$ edge states exist. This connection between topological phases and boundary modes is very useful for experimental detection of toplogical phases. Often in experiments, it is easier to measure properties of non-trivial boundary states than it is to characterize the value of the bulk topological invariant.

2.2 Haldane model for anomalous quantum Hall effect

In this section, we describe a lattice model that exhibits quantized Hall response as proposed by Haldane [35]. This model considers non-interacting electrons in a tight-binding model on a honeycomb lattice. A schematic figure of the lattice model is shown in Fig. 2.2 (a). The minimal model consists of nearest and next-nearest neighbor hopping in the honeycomb lattice.

The Hamiltonian in second quantized notation for the electrons in real space is

$$H = \sum_{i,\alpha\neq\alpha'} t_1 c^\dagger_{i,\alpha} c_{i,\alpha'} + \sum_{\langle i,j\rangle} \tilde{t}_2 c^\dagger_{i,\alpha} c_{j,\alpha} + \sum_{i,\alpha,\alpha'} M\sigma^z_{\alpha\alpha} c^\dagger_{i,\alpha} c_{i,\alpha}, \tag{2.3}$$

where $c^\dagger_{i,\alpha}$ creates an electron at the i^{th} unit cell, and in the A ($\alpha = 1$) or B ($\alpha = 2$) sublattice and $\langle \cdots \rangle$ denotes nearest neighbor unit cells. The z Pauli matrix is defined as $\sigma^z_{\alpha\alpha'} = 0$ when $\alpha \neq \alpha'$ and $\sigma^z_{\alpha\alpha} = 1$ (-1) for $\alpha = 1$ (2). The sublattice hopping unit vectors are denoted as $\mathbf{a}_1/a = \sqrt{3}/2\hat{x} + 1/2\hat{y}$, $\mathbf{a}_2/a = -\sqrt{3}/2\hat{x} + 1/2\hat{y}$, and $\mathbf{a}_3 = -a\hat{y}$, where a denotes the spacing between the A and B sublattices in a unit cell.

Let us discuss the terms in the Hamiltonian defined in Eq. (2.3). The first term, t_1 is the magnitude of hopping between nearest neighbor A and B sublattices and is chosen to be real. The second term, $\tilde{t}_2$ denotes the next nearest neighbor hopping between A-to-A and B-to-B sublattices. The hopping parameter is chosen to be a complex phase, $\tilde{t}_2 = t_2 \exp(i\phi)$ for the direction shown in Fig. 2.2 (a). This term breaks time-reversal symmetry and is necessary to induce a quantized Hall response. Finally, the third term is a mass term, M which breaks the inversion symmetry between A and B sublattice sites.

The spectrum of the model is obtained in momentum space. When t_2 and M is zero, the hopping model is identical to that of electrons in graphene [13]. The spectrum has two Dirac points at the K and K' points in the Brilluoin zone. A gap can be

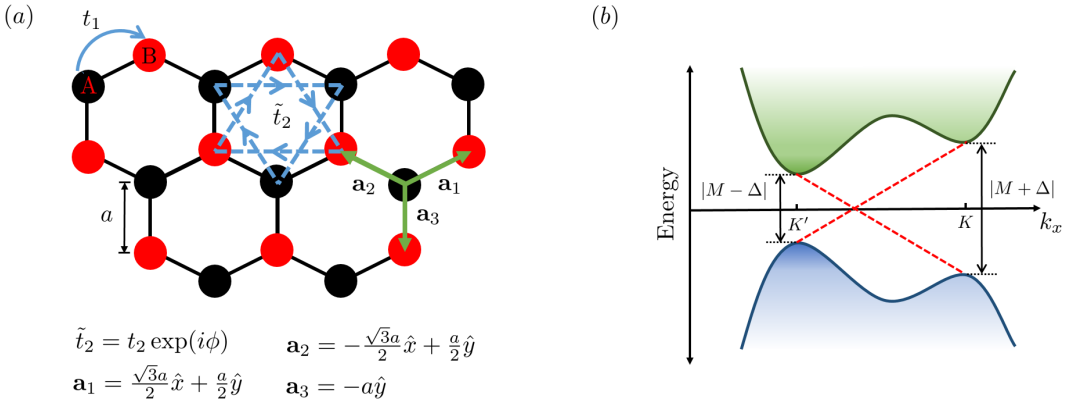

Figure 2.2: Model for anomalous quantum Hall effect [35]. (a) shows the schematic of the tight binding model on a honeycomb lattice. A and B sublattices are represented as black and red circles. The model has nearest neighbor hopping (A→B), t_1 which is a real number. The next-nearest neighbor hopping is (A→A or B→B) chosen to be complex $\tilde{t}_2 = t_2 \exp(i\phi)$. The lattice spacing is a and the unit vectors connecting nearest neighbors are labeled as $\mathbf{a}_1$, $\mathbf{a}_2$, and $\mathbf{a}_3$. (b) shows the schematic bandstructure for the Haldane model in a cylindrical geometry when in the topological phase. The energy spectrum is shown as a function of the momentum in the x direction, k_x. The topological phase is realized when $M > \Delta$ (See 2.4). The gaps open at the K and K' points. In the cylindrical geometry, edge states (shown in red) must exist in the gap. These states are chiral in nature and the doubly degenerate states correspond to the different edges of the cylinder.

opened in the spectrum by breaking inversion or time-reversal symmetry. The mass term, M, breaks inversion symmetry and opens a trivial gap at the Dirac point. The hopping term, t_2 on the other hand breaks time-reversal symmetry. This gap opened is a topological gap, and the resulting insulator has bands with non-zero Chern number. This is precisely the term necessary for a Hall response. These features can be understood by studying the spectrum linearized around the Dirac points,

$$H(\mathbf{k}) = v(k_x\sigma_x\tau_z + k_y\sigma_y) + M\sigma_z + \Delta\sigma_z\tau_z, \tag{2.4}$$

where σ denotes the sublattice (A or B) pseudospin, τ denotes the K or K' valley degree of freedom and $\Delta = 3\sqrt{3}t_2 \sin(\phi)$. Examining Eq. (2.4), it is clear that when, M and Δ are zero, the spectrum is gapless with a linear dispersion relation. The terms M and Δ opens up gaps at the Dirac points. At the K valley point the gap is $m_1 = M + \Delta$ and at the K' point the gap is $m_2 = M - \Delta$. The schematic spectrum is shown in Fig. 2.2 (b).

In the presence of the two mass terms, M and Δ, the spectrum is that of a band insulator with a gap at zero energy. Consider the scenario when the Fermi energy

is in the gap and all the states in the lower band are filled. The topological nature of the band is revealed by the sublattice pseudospin (σ) texture in this band. The pseudospin direction in the band defines a map from the Brilluoin zone to the sphere, $T^2 \to S^2$. The topological invariant classifying these maps is the Chern number. We discuss these maps in greater detail in the next section when we discuss anomalous quantum Hall phases in the BHZ model. In order to have a non-zero Chern number, it is necessary to have the pseudospin map to both poles of the sphere, S^2, an odd number of times. This is realized when the two mass gaps, m_1 and m_2, have opposite signs. This is because at the K and K' points the pseudo-spin must point at $\mathrm{sgn}(m_1)\hat{z}$ and $\mathrm{sgn}(m_2)\hat{z}$ directions respectively. Therefore, a topological phase is realized when $|\Delta| > |M|$. When this condition is satisfied, chiral edge states will be observed with energies smaller than the band gap.

2.3 BHZ model for Topological Insulators

The topological insulators were first proposed by Kane and Mele [46] in the honeycomb lattice and Bernevig, Hughes and Zhang in HgTe/CdTe quantum well models [10]. The latter has been experimentally observed in the quantum wells by König et al. [56]. Topological insulators have also been proposed [26] and observed in three dimensions [38]. We focus only on two-dimensional topological phases. These models are time-reversal invariant. Unlike the integer quantum Hall effect, where time-reversal symmetry is broken, these topolgical phases are classified by a $\mathbb{Z}_2$ index. This means that there exists only one topological and one trivial phase and two copies of the topological phase can be adiabatically connected to the trivial phase.

Let us discuss the BHZ quantum well model for a topological insulator. This is a model of a strong spin-orbit coupled insulator with an inverted mass gap. The minimal model is a 4×4 Hamiltonian consisting of 4 bands $|E_1, m_J = \pm 1/2\rangle$ and $|H_1, m_J = \pm 3/2\rangle$. The model breaks up into two independent time-reversed Kramers' partners, $\{|E_1, +\rangle, |H_1, +\rangle\}$ and $\{|E_1, -\rangle, |H_1, -\rangle\}$. The Hamiltonian is defined on a square lattice. In momentum space it becomes

$$H(\mathbf{k}) = \begin{pmatrix} h(\mathbf{k}) & 0 \\ 0 & h^*(-\mathbf{k}) \end{pmatrix}, \tag{2.5}$$

$$\text{with, } h(\mathbf{k}) = \mathbf{d}(\mathbf{k}) \cdot \boldsymbol{\sigma}, \tag{2.6}$$

$$\mathbf{d}(\mathbf{k}) = \Big(A \sin k_x, A \sin k_y, M - 2B(2 - \cos k_x - \cos k_y)\Big), \tag{2.7}$$

where the Pauli matrix, $\boldsymbol{\sigma}$ is in the pseudospin basis $\{|E_1, +\rangle, |H_1, +\rangle\}$. In the above

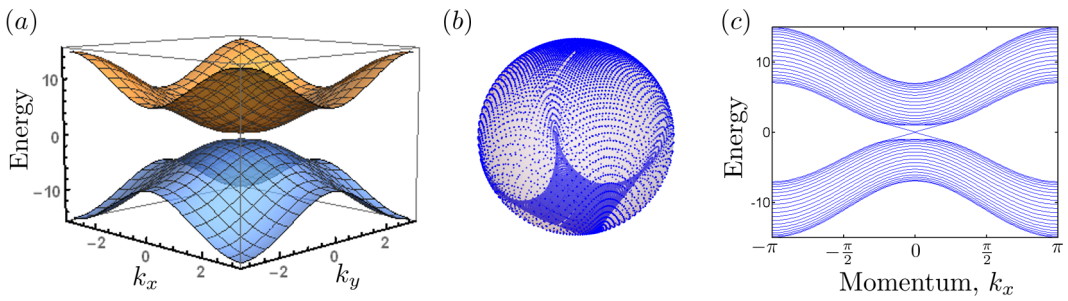

Figure 2.3: Properties of one block of the BHZ model. The Hamiltonian is given in Eq. (2.6) (a) Bulk bandstructure of the model. The parameters are chosen to $A/|M| = 2$, $B/|M| = -2$, $M/|M| = -1$. In this model, we set lattice spacing, $a = 1$. The non-zero mass, M results in a band-gap which is smallest at $(k_x, k_y) = (0, 0)$. (b) The unit vector, $\hat{d}(k_x, k_y)$ is a map from $\{k_x, k_y\}$ in the FBZ to the unit sphere. This plot shows $\hat{d}$ as blue points on the sphere. Since the Hamiltonian is chosen in the topological phase, the Chern number is non-zero, $C = 1$. This corresponds to $\hat{d}$ wrapping around the unit sphere. (c) The bandstructure of the Hamiltonian defined on a cylinder. Open boundary conditions are along y direction, with the number of lattice points along y, $L_y = 20$. There exists no gap in this spectrum. This is because there are additional states in the bulk gap which correspond to the edge states.

equation, we have chosen the convention that the lattice spacing is, $a = 1$. The model depends on three parameters A, B, and M, which are determined by the geometry of the quantum well.

The topological or trivial nature of the bands can be obtainedby examining a single block of the full BHZ model, defined by the Hamiltonian in Eq. (2.6). This reduced model describes the anomalous quantum Hall phase in a square lattice [71]. This phase is analogous to the model described by Haldane in the honeycomb lattice discussed in Section 2.2. The spectrum of this reduced two band model is shown in Fig. 2.3 (a). The topological classification of the anomalous quantum Hall phase is indexed by a $\mathbb{Z}$ number. This can be seen as follows. The pseudo-spin direction, $\hat{d}(\mathbf{k})$ defines a map from the Brilluoin zone to a unit sphere, $\hat{d}(\mathbf{k}) : T^2 \to S^2$. The topological number that classifies this map, is the Chern number,

$$C = \frac{1}{4\pi} \int_{FBZ} d\mathbf{k}\, \hat{d}(\mathbf{k}) \cdot \left(\partial_{k_x} \hat{d}(\mathbf{k}) \times \partial_{k_y} \hat{d}(\mathbf{k}) \right), \tag{2.8}$$

where the integral is done over the first Brilluoin zone. Intuitively, the Chern number (C) counts the number of times the unit vector $\hat{d}(\mathbf{k})$ wraps around the unit sphere as one maps the pseudospin texture in the first Brilluoin zone. Clearly, this can happen only an integer number of times. Therefore, the phases must be classified by a $\mathbb{Z}$

topological invariant, which precisely is the Chern number.

A topologically non-trivial phase is realized when the Chern number is non-zero. In the reduced model, $C = 1$, when, $0 < M/(2B) < 2$ and $C = 0$, $M/(2B) < 0$. We show some of the characteristics of the model when in the topological phase in Fig. 2.3. The parameters of the model chosen are $A/|M| = 2$, $B/|M| = -2$ and $M/|M| = -1$. In Fig. 2.3 (b) we show the mapping of $\hat{d}(\mathbf{k})$ on the unit sphere. Clearly, $\hat{d}$ wraps around the sphere, indicating a topological phase. The topological phase must have chiral edge-states at the boundaries. This can be seen in the spectrum for the model on a cylindrical geometry. In contrast with the gapped bulk spectrum (as shown in Fig. 2.3 (a)), the spectrum on a cylinder is clearly gapless. These new states in the bulk gap correspond to chirally propagating states, that are exponentially decaying away from the edges of the cylinder. These edge states are a hallmark of a topological phase.

The full 4×4 BHZ model as described by Eq.(2.5) is time-reversal invariant. This is because the two decoupled 2×2 blocks are time-reversed partners. As long as time-reversal symmetry is present, there is no coupling that connects these two blocks. This implies that the bands are doubly degenerate with corresponding Kramers' partners. The BHZ model corresponds to class AII in the periodic table of topological insulators. These models are described by a $\mathbb{Z}_2$ topological invariant. The topological phase corresponds to the scenario when the upper 2×2 block, $h(\mathbf{k})$, is in the phase with a Chern number, $C = +1$. The lower 2×2 block is the time-reversed partner of the upper block, and therefore has a Chern number, $C = -1$. This means that the boundary of this topological phase must have counter-propagating edge states. The edge states are protected by time-reversal symmetry. As long as disorder respects this symmetry, the edge state cannot scatter with its Kramers partner moving in the opposite direction. This is no longer true if time-reversal symmetry is broken. In this section, we described a topological phase that is protected by a symmetry (time-reversal). Such phases are generically labelled as Symmetry Protected Topological (SPT) phases.

2.4 Disorder and topological phases

Topological phases by nature are robust to local imperfections. This is because the topological invariant of a phase cannot be changed by disorder as long as the mobility gap in the spectrum is not closed. One must note that in a disordered system, a gap is smeared out by localized states (see Fig. 1.1). Therefore, the stability of a topological

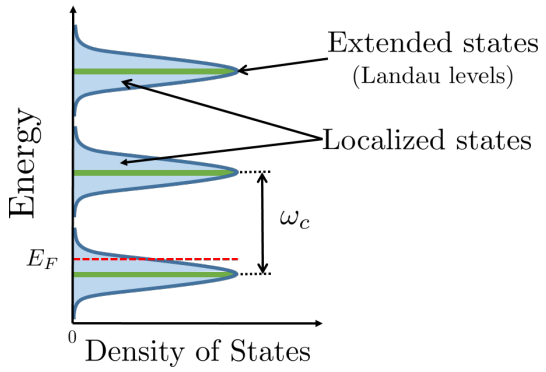

Figure 2.4: The generic density of states of a 2DEG exhibiting integer quantum Hall effect. There exists a bulk delocalized state at the energy for the Landau levels (shown in green). The Landau levels are separated by the cyclotron frequencey $\omega_c = eB/m$, where we set $\hbar = 1$. The spectrum is broadened by localized states (shown in light blue). When the Fermi energy, E_F, is pinned between two landau levels, it corresponds to a localized state in the bulk. This means that the bulk behaves like an Anderson insulator.

phase is defined in terms of the mobility gap in the spectrum. The robustness to disorder implies that the edge states are protected against backscattering in the presence of impurities. Unlike bulk states, which propagate diffusively in the presence of disorder, the edge states propagate ballistically.

In the following, we outline two different effects due to disorder in models that host topological phases. Firstly, we elaborate on the role of disorder in the Integer quantum Hall plateaus. Secondly, we show that disorder can induce a topological phase in a trivial BHZ Hamiltonian. This phase is labeled the Topological Anderson Insulator (TAI).

Disorder in IQH

Disorder plays a crucial role in Integer Quantum Hall effect. As first pointed out by Halperin [36], disorder must broaden the Landau levels. The generic density of states is shown in Fig. 2.4, with peak positions at the position of the Landau levels. Generically the gap between Landau levels maybe smeared out by localized states. The localized states are essential to pin the chemical potential between two Landau level without which it would be impossible to observe the quantized Hall conductance.

The topological nature of the Landau levels have a very important consequence on the nature of bulk states in the Landau levels. The presence of a nontrivial topological

invariant provides an obstruction to the localization of all bulk states in the Landau levels. This is in contrast to what is expected in topologically trivial systems. As discussed in Section 1.3, there is no Anderson transition in two dimensions, and all states localize at infinitesimal disorder strength in the thermodynamic limit. In quantum Hall effect, as a consequence of the non-trivial topology, there must exist an energy where the bulk state is delocalized. This is shown schematically in Fig. 2.4. The non-zero value of the Chern number is due to this state, since Anderson localized states are topoogically trivial. It is expected that there exists only a single critical energy in each Landau level that is delocalized.

The presence of a delocalized bulk state indicates that a localization-delocalization transition can be accessed by tuning the Fermi energy. This is done experimentally to access the critical exponents of the quantum Hall localization transition. At the critical point, the localization length must diverge, $\xi \sim |E - E_c|^{-\nu}$, where ν is the critical exponent and E_c is the critical energy. Koch et al. [55] experimentally measured this exponent through size dependent scaling. The exponent, $\nu \approx 2.3$. The critical exponents obtained for this transition also describes the localization transition for other topological models in this symmetry class (class A) and dimension ($d = 2$).

The localization transtion in quantum Hall effect can be understood in terms of the network model that was introduced by Chalker and Coddington [14]. In this model, it is assumed that disorder is a smoothly varying potential landscape. The quantum Hall state, breaks up into islands of topological and trivial states. As a consequence, there exists edge states at the boundaries of these islands. The localization transition occurs at the quantum percolation transition of these edge states. This picture of a percolation transition applies to localization transitions of other topological phases as well such as topological insulators [95].

Topological Anderson Insulator

Disorder counter intuitively may induce topological phases in a clean trivial system and such phases have been labeled as Topological Anderson insulators (TAI) [33, 67]. Such disorder induced phases are quite universal and similar phases have been observed in other models such as the Haldane model [102, 117].

As an explicit example we consider a trivial semiconducting quantum well described by the BHZ model. We consider only the upper block Hamiltonian, $h(\mathbf{k})$, as shown in Eq. (2.6). In this case, the clean system is trivial, i.e. $M/2B < 0$. Generic

bulk states in a two dimensional trivial spinless insulators must localize for any infinitesimal disorder strength. In contrast, for models with spin-orbit coupling, on-site disorder gives rise to the possibility of a localization transition at a finite disorder strength. This distinction in the localization properties between systems on the basis of the spin rotation symmetry is described in Sec. 1.3. Before the onset of localization, disorder primarily renormalizes the parameters of the Hamiltonian modifying the single particle density of states. Notably, it renormalizes the mass, M. Disorder can change its sign leading to an induced topological phase.

At weak disorder strength, sufficiently smaller than the critical disorder for the localization transition, there must exist a region of extended states in the band-structure (similar to the critical levels in density of states in integer quantum hall effect as shown in Fig. 2.4). As discussed in Sec 1.1, the lowest order correction to the density of states due to disorder is given by the self-consistent Born approximation of the disorder-averaged Green's functions. In this approximation, the self-energy correction to the average Green's function[33],

$$\begin{aligned} \Sigma(E) &= \overline{V_{\text{dis}}^2} \int d\mathbf{k} \frac{1}{E - h(\mathbf{k}) - \Sigma}, && (2.9) \\ &= \Sigma_I \mathbb{1} + \Sigma_x \sigma_x + \Sigma_y \sigma_y + \Sigma_z \sigma_z. && (2.10) \end{aligned}$$

Here, $\overline{V_{\text{dis}}^2} = \sigma_{\text{dis}}^2$ is second moment of the disorder potential, and E is the energy. The self-energy is generically a 2×2 matrix and can be expanded in terms of Pauli matrices as shown in Eq. (2.10). The different components of Σ in Eq. (2.10) renormalize different parameters of the Hamiltonian. This renormalization is present even if the average value of the disorder potential vanishes, $\overline{V_{\text{dis}}} = 0$. For uniformly random disorder (see Eq. (1.1) for definition), an analytical formula is obtained for the Born approximation [33]. The renormalized parameters of the BHZ model are

$$\begin{aligned} &\tilde{A} = A, \quad \tilde{B} = B, \quad \tilde{E}_F = E_F, \\ &\tilde{M}(E_F) = M + \frac{U_0^2}{48\pi} \frac{1}{B} \log \left| \frac{B\pi^4}{E_F^2 - m^2} \right|, \end{aligned} \tag{2.11}$$

where in general, the renormalized parameters are functions of the fermi-energy, E_F. This is because the self energy correction due to disorder is, in general, a function of all the variables, $\Sigma \equiv \Sigma(E_F, A, B, M)$. In the trivial phase, consider the case when $M > 0$, and $B < 0$. The correction due to disorder is clearly negative. This means for sufficiently strong disorder, when $\tilde{M} < 0$, the phase undergoes a

transition into a topological phase. We note that this phase transition is independent of the localization transition at strong disorder.

2.5 Summary

In this chapter, we discussed three different examples of non-interacting topological phases and their interplay with disorder. The integer quantum Hall effect was one of the first topological phases to be discovered. The Hall conductance is proportional to the Chern number, a topological invariant. The Haldane model for the anomalous quantum Hall effect is an example of a lattice model that is topologically non-trivial. In this case, the bulk bands are topological with a Chern number that can be obtained from integrating over the band in the first Brilluoin Zone. Finally we discussed the Topological Insulator, which can be considered as two time-reversed copies of the anomalous quantum Hall phase. The topological invariant classifying these phases is a $\mathbb{Z}_2$ number. In all topological phases, the non-trivial topological invariant results in a universal robustness to weak disorder. The scale for the disorder is set by the bulk mobility gap. At strong disorder, the topological phase is destroyed due to a localization transition. The transition can be characterized as a quantum percolation transition. The topology, dimensions, and symmetry determine universal critical exponents for the transition. At weak disorder, before localization, the disorder perturbatively renormalizes the parameters of the Hamiltonian. When the clean system is topologically trivial, this can give rise to a disorder induced phase, the Topological Anderson Insulator.

Chapter 3

PERIODICALLY DRIVEN TOPOLOGICAL SYSTEMS

Topological phases have exotic properties and have the potential for applications, but there are still only a few candidate topological materials, especially in two dimensions. One method to generate new topological states is via periodic driving of a topologically trivial system out of equilibrium. These are the so-called Floquet topological Insulators (FTIs). They might be obtained by irradiating ordinary semiconductors with a spin-orbit interaction [69, 70], or graphene-like systems [19, 32, 53, 84]; analogues in superconducting systems have also been proposed [44, 61]. These proposals have stimulated intense activity in the study of such driven topological phases. [34, 44, 47, 53, 60, 68–70, 72, 84, 110].

Just like topological insulators, FTIs have gapless edge states. These driven phases not only exhibit the standard phenomena associated with static topological phases, but could also exhibit anomalous topological phases that are impossible in undriven, static systems [31, 94, 108]. The stability of such a non-equilibrium phase is far from guaranteed. Recent works have also explored transport in Floquet topological phases[23–25, 61, 112] and means to stabilize such phases in many-particle steady states using dissipation[17, 18, 99]. In Part II, we discuss the stability of the FTIs to disorder and other new non-equilibrium phases that may be induced in the present of disorder.

Recently, several experiments probed Floquet topological phases in solid-state[113], optical[92] and cold-atom[45] based systems. Wang et al. [113] irradiated a topological insulator surface with circularly polarized pulse. In these experiments, the surface Dirac fermions form Floquet-Bloch bands with radiation induced gaps at the Dirac point and the crossings. Rechtsman et al. [92] realized a Floquet topological insulator phase in a lattice of photonic waveguides. In this case, topological protection is obtained in the propagation of light through the waveguides. We describe this experiment in Section 3.5. Jotzu et al. [45] also realized the Floquet-Haldane model in a lattice of ultracold fermionic atoms. The driving is implemented by modulating the underlying optical lattice in a periodic manner.

We define a time-dependent Hamiltonian that is periodic with a time period T,

$$H(\mathbf{k}, t) = H(\mathbf{k}, t + T), \quad \text{with} \quad T = 2\pi/\Omega, \tag{3.1}$$

where Ω determines the frequency of the drive. In time-dependent Hamiltonians, energy is not a well defined quantum number. It is necessary to solve the full time-dependent Schrödinger equation. As we show in Section 3.1, for a time-periodic Hamiltonian, it is possible to reduce it to an effective time-independent eigenvalue equation. This is a consequence of the Floquet-Bloch theorem. The so-called Floquet Hamiltonian conserves energy modulo the frequency of the drive, which we label as quasienergy.

Periodically driven non-interacting Hamiltonians may be classified on the basis of the topology of the gapped quasienergy bandstructures analogous to time-independent Hamiltonian. In Sections 3.3 and 3.2 we describe two examples of Floquet topological insulators and Floquet Chern insulators. As was pointed out by Kitagawa et al. and Rudner et al. [52, 94], Floquet bandstructures have a broader topological classification compared to time-independent bandstructures. In Section 3.5, we describe an example of such a phase, the Anomalous Floquet topological phase. This system realizes a band structure that cannot be realized in static systems. The bulk of the Floquet Hamiltonian is topologically trivial and yet the system has non-trivial chiral edge states at the boundary.

3.1 Floquet-Bloch Theory: Definitions

Let us start with a specific form of the Hamiltonian, $H(t)$ that is periodic in time,

$$H_r(\mathbf{k}, t) = H_0(\mathbf{k}) + V(t), \text{ with, } V(t+T) = V(t) \tag{3.2}$$

with $T = 2\pi/\Omega$ as the time-period, Ω being the frequency. Here, H_0 contains the time-independent terms of the Hamiltonian. The steady states are given by the solution to the full time-dependent Schrödinger equation,

$$i\hbar\frac{\partial}{\partial t}\psi(\mathbf{k}, t) = H_r(t)\psi(\mathbf{k}, t). \tag{3.3}$$

The Floquet-Bloch theorem states that, the time-evolution operator can be written as

$$U(t,0) = \mathcal{T}\exp\left(\int_0^t ds H_r(s)\right) \tag{3.4}$$

$$= \exp\left(-iH_r^F t\right) W(t), \text{ where, } W(t+T) = W(t), \tag{3.5}$$

where in Eq. (3.4), $\mathcal{T}$ indicates time-ordering, and H_r^F is a time-independent Hermitian operator. The form of Eq. (3.5) allows us to identify H_r^F as an effective

time-independent Floquet Hamiltonian. In order to define H_r^F, for the case at hand, the Fourier decomposition of the solution to Eq. (3.3) is used,

$$\psi(\mathbf{k},t) = \sum_n \psi_n(\mathbf{k}) e^{in\Omega t}, \tag{3.6}$$

$$= \sum_n \langle n|\psi^F\rangle\langle t|n\rangle, \quad \text{with } \langle t|n\rangle = e^{in\Omega t}. \tag{3.7}$$

In Eq. (3.7), we have introduced an additional register index, $\{|n\rangle\}$, where $n \in \mathbb{Z}$. We will refer to this register index to identify the Floquet zone, or block in the matrix, H_r^F. The Floquet Hamiltonian, H^F, is defined in a way such that $|\psi^F\rangle$ are eigenstates. Necessarily, it is defined in an extended Hilbert space $\mathscr{H} \otimes \{|n\rangle\}$, where $\mathscr{H}$ is the original Hilbert space of the Hamiltonian (see Eq. (3.2)). The time-dependent Schrödinger equation is rewritten in an effective time-independent form,

$$H_r^F|\psi^F\rangle = \epsilon|\psi^F\rangle, \tag{3.8}$$

where H_r^F is now formally an infinite dimensional matrix. The eigenvalues (ϵ) are referred to as quasi-energies, and the eigenfunctions of the Floquet Hamiltonian, defined in Eq. (3.8), are the quasienergy states.

The spectrum of H_r^F is unbounded; however, we note that in Eq. (3.5), the eigenvalues (ϵ) of H_r^F describe the non-periodic evolution of these states as a function of time. Therefore, they are unique modulo Ω, $\epsilon \equiv \epsilon + m\Omega$, where $m \in \mathbb{Z}$. The explicit form of the Floquet Hamiltonian for $H(t)$ defined in Eq. (3.2) is,

$$(H^F(\mathbf{k}))_{mn} \equiv \langle m|H^F(\mathbf{k})|n\rangle,$$

$$= (H_0(\mathbf{k}) + n\Omega)\delta_{mn} + \tilde{V}_{mn}, \tag{3.9}$$

where

$$\tilde{V}_{mn} = \frac{1}{T}\int_0^T dt V(t) e^{i(m-n)\Omega t}. \tag{3.10}$$

The integers m and n indexes a particular Floquet block in the matrix H^F. In this representation, the time-independent terms, like H_0, are diagonal, but the time-dependent potential, $V(t)$, acts as a hopping amplitude between various Floquet blocks. These Floquet blocks are like replicas of the original Hamiltonian shifted in quasienergy by Ω, and the indices will also be referred to as the replica index. We refer to this representation of the Floquet Hamiltonian as the extended zone representation. The Floquet matrix, H_r^F, is formally infinite dimensional, so, in order to compute the quasi-energies numerically, we truncate the matrix after N_F blocks, with N_F determined using convergence tests.

Alternatively, we can also obtain the Floquet Hamiltonian in a folded zone representation. In this representation, we define the Floquet Hamiltonian from the stroboscopic time evolution operator for a full time period. Using the definition of the time-evolution operator in Eq. (3.5), we have

$$H_r^F = \frac{i}{T}\log(U(T,0)), \tag{3.11}$$

where the branch cut for the log is chosen such that, $-i\log e^{i\epsilon T} = \epsilon T \ \forall \ \epsilon T \in [0,\pi)$ and $-i\log e^{i\epsilon T} = \epsilon T - 2\pi \ \forall \ \epsilon T \in [\pi, 2\pi)$. The eigenvalues of $U(T,0)$ naturally are a phase, $e^{i\epsilon T}$ and therefore, the quasi-energy spectrum of H_r^F, $epsilon$ is compact, $\epsilon \in [-\pi/T, \pi/T)$.

The Floquet Green function is defined from the Floquet Hamiltonian, H^F, as

$$G_r^F(E,\mathbf{k}) = \frac{1}{(E\mathbb{1} - H_r^F(\mathbf{k}))}. \tag{3.12}$$

All elements of G_r^F can be rewritten in a closed analytical formula [53, 78] for the special case where the only non-zero components of $\tilde{V}_{mn}$ are $V_- = \tilde{V}_{m+1,m}$ and $V_+ = \tilde{V}_{m,m+1}$ with $m \in \mathbb{Z}$. For example, the $(m = 0, \ \ n = 0)$ Floquet block, of the Green function is

$$\begin{aligned}(G_F)_{00} &= \frac{1}{E\mathbb{1} - H_0 - V_{\text{eff}}^+ - V_{\text{eff}}^-}, \\ V_{\text{eff}}^{\pm} &= V_+ \frac{1}{E \pm \Omega - H_0 - V_+ \frac{1}{E\pm 2\Omega - H_0 - V_+ \frac{1}{\vdots} V_-} V_-}.\end{aligned} \tag{3.13}$$

where $V_{\text{eff}}^{\pm}$ is in the form of a continued fraction. Analogously, the different Floquet blocks of the Green function can be obtained. Therefore, the Green function can be obtained perturbatively to any order in V by truncating the continued fraction to that order.

3.2 Floquet Topological phases : Haldane model

The topological behavior in the non-equilibrium situation is obtained by choosing a drive of appropriate frequency. We show the non-trivial topology of the quasienergy band-structure for the graphene based model in the presence of circularly polarized light. When the frequency is much larger than the bandwidth of the Hamiltonian, the topological mass term of the Haldane model (Δ defined in Eq. 2.4) is generated.

The tight-binding model on a hexagonal lattice with only nearest neighbor hopping was discussed in Chapter 2 ($t_1 \neq 0$ and $t_2 = 0$ in Eq. 2.3). As defined in Eq. (2.4),

in the low energy limit by linearizing around the Dirac points,

$$H_0(\mathbf{k}) = v(k_x\sigma_z\tau_z + k_y\sigma_y) + M\sigma_z, \tag{3.14}$$

where σ_x and τ_z refer to sub-lattice isospin and valley degree of freedom respectively, $\mathbf{k} \equiv (k_x, k_y)$, v is the Fermi velocity at the Dirac points, and M is the sub-lattice mass term.

Circularly polarized radiation is introduced in the model through a spatially uniform but time-dependent vector potential, $\mathbf{A}(t) = A_0(\sin(\Omega t), \cos(\Omega t))$. In the presence of this gauge field, the Hamiltonian is modified using the Pierels substitution,

$$H_r(\mathbf{k}, t) \equiv H_0(\mathbf{k} - \mathbf{A}) = v((k_x - A_x)\sigma_x\tau_z + (k_y - A_y)\sigma_y) + M\sigma_z, \tag{3.15}$$

where $\mathbf{A} \equiv (A_x, A_y)$ is the vector potential for incident radiation. Consider a general form of the external drive defined in Eq. (3.2),

$$V(t) = V_+ e^{i\Omega t} + V_- e^{-i\Omega t}, \tag{3.16}$$

where $V_\pm$ are time-independent operators. In this model we have in terms of $\mathbf{A}$,

$$V_+ = A_0\left(\frac{i}{2}\sigma_x\tau_z - \frac{1}{2}\sigma_y\right), \tag{3.17}$$

$$V_- = V_+^\dagger. \tag{3.18}$$

Note that the analysis discussed here (see Eq. (3.14) to Eq. (3.18)) is valid only in the perturbative low energy regime with $|\mathbf{A}| \ll 1$. This is because we have ignored the corrections to the spectrum that are higher order in $\mathbf{k}$.

This model breaks time-reversal symmetry, and its topological phases are classified by the Chern number. Let us consider the case that corresponds to irradiating the system with off-resonant light. The incident frequency of the drive, $\Omega \gg W$, where W is the bandwidth of the time-independent band-structure. The correction to the energies of the non-equilibrium states are obtained by inspecting the poles of the Floquet Green function. In this case, to lowest order in the radiation potential, the off-diagonal terms in G^F can be ignored. The diagonal element, G^F_{00} is obtained from the formula given by Eq. (3.13). We write, G^F to second order in the radiation potential,

$$G^F_{00} = \left(E\mathbb{1} - H_0 - \frac{[V_+, V_-]}{\Omega}\right)^{-1} = (E\mathbb{1} - H_{\text{eff}})^{-1}, \tag{3.19}$$

where we have a new effective Hamiltonian, H_{eff}. Using equations (3.17), (3.18) and (3.19), we note that H_{eff} is equivalent to the Haldane model for anomalous quantum Hall effect (see Section 2.2) with a topological mass $\Delta = \frac{v^2 A_0^2}{\Omega}$,

$$H_{\text{eff}} = v(k_x\sigma_x\tau_z + k_y\sigma_y) + M\sigma_z + \Delta\sigma_z\tau_z \tag{3.20}$$

$$= \begin{pmatrix} \Delta_+ & k_x - ik_y & 0 & 0 \\ k_x + ik_y & -\Delta_+ & 0 & 0 \\ 0 & 0 & \Delta_- & -k_x - ik_y \\ 0 & 0 & -k_x + ik_y & -\Delta_- \end{pmatrix}, \tag{3.21}$$

where τ denotes the valley space, and $\Delta_\pm = M \pm \Delta$. The mass gap opens at the Dirac points of the band-structure near $\epsilon = 0$.

The bands will be topological or trivial when $M < \Delta$ and $M > \Delta$ respectively. In Fig. 3.1, we plot representative bandstructures of this model for different cases of M, A_0 and Ω. In Fig. 3.1 (a) we plot the simplest case of the Floquet Haldane model. The inversion symmetry breaking mass, M, is set to zero. The parameters are, $A_0 = 1.43$, $M = 0$, $\Omega/\tilde{t} = 12$ and $\tilde{t}/t_1 = J_0(A_0)$, where J_0 is the Bessel function of the first kind. The bulk is gapped and in a cylindrical geometry, there are edge states in the gap. When inversion symmetry is broken the system can become topologically trivial. An example bandstructure is shown in Fig. 3.1 (b) where there is a gap at quasienergy, $\epsilon = 0$, even in cylindrical geometry. This indicates a trivial phase.

The bulk topological invariant is the Chern number. Since the quasienergy spectrum is unbounded, in order to define a Chern number, it is necessary to project to the band of relevant states. Let us define the projection operator (P), that projects to states with quasienergies (ϵ) satisfying the bounds, $\epsilon_l < \epsilon < \epsilon_u$. The Chern number can now be defined for these states. Let us set $\epsilon_l = -\Omega/2$. For $M < \Delta$, the Chern number, $C = 1$, when measured at quasi-energies in the gap, $-(\Delta - M) < \epsilon_u < \Delta - M$, and is zero at all other quasi-energies.

The quasienergy spectrum is also sensitive to the magnitude of the drive frequency. It is possible to induce topological phases with higher Chern numbers in the presence of resonances in the bandstructure. This is shown in Fig. 3.1 (c). We discuss this case in detail in Section 3.4.

3.3 Floquet topological phases : BHZ model

We start with the single block of the Bernevig-Hughes-Zhang (BHZ) [10] model of a two-dimensional, spin-orbit coupled, semi-conducting quantum well in the presence

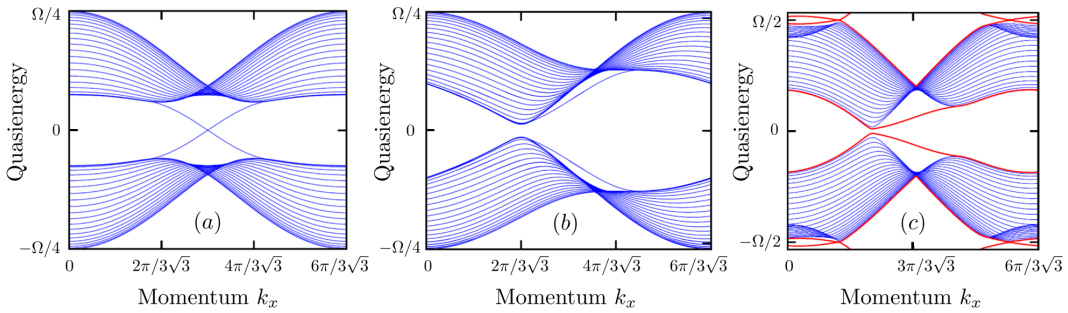

Figure 3.1: Quasienergy bandstructure for the driven honeycomb lattice model for different cases of drive and sublattice pseudospin mass. (a) The Floquet Haldane model, without any sublattice mass term. The parameters are, $A_0 = 1.43$, $M = 0$, $\Omega/\tilde{t} = 12$ and $\tilde{t}/t_1 = J_0(A_0)$, where J_0 is the Bessel functionof the first kind. The system is topological and supports edge states. The bulk gap is given by the topological mass $\Delta/\tilde{t} \approx 0.75$. (b) A trivial Floquet bandstructure where the sublattice mass satisfies, $M > \Delta$. All parameters are the same as (a) except $M/\tilde{t} = 0.85$. (c) Quasienergy spectrum when the frequency of the drive is chosen smaller than the bandwidth of the time-independent spectrum. There are edge states that wind around the quasienergy Brilluoin zone. In this case, the mass M is chosen to have a trivial gap at the Dirac points. The system parameters are $A_0 = 0.75$, $M/t_1 = 0.3$, and $W/t_1 = 9/2$.

of a periodic drive[69] ,

$$H(\mathbf{k}, t) = \mathbf{d}(\mathbf{k}) \cdot \boldsymbol{\sigma} + \mathbf{V} \cdot \boldsymbol{\sigma} \cos(\Omega t), \tag{3.22}$$

$$\equiv H_0 + V, \tag{3.23}$$

where $\mathbf{d}(\mathbf{k}) = \left(Ak_x, Ak_y, M - B(k_x^2 + k_y^2)\right)$, k_x and k_y being the crystal momentum along x and y directions. The details of the time-independent part of the Hamiltonian is defined in Section 2.3. The system is driven periodically at a frequency, Ω with $\mathbf{V} = (V_x, V_y, V_z)$. The periodic drive, $\mathbf{V}$ may be physically obtained either from a periodic Zeeman field, or an elliptically polarized radiation. In the presence of a periodically varying Zeeman field, the components, V_x, V_y, and V_z are constants. Explicitly, a magnetic field, $\mathbf{B} = B_0 \cos(\Omega t)\hat{z}$, results in a driving term, $\mathbf{V} = \hat{z}(g_E - g_H)\mu_B B_0$, where $g_{E,H}$ is the Zeeman coupling for E_1 and H_1 pseudospin bands, and and μ_B is the Bohr magneton. For an elliptically polarized radiation, $\mathbf{V}$ is dependent on the crystal momentum, $\mathbf{k}$. We discuss the details of using elliptically polarized light in Section 3.4.

Let us start with the time-independent Hamiltonian, H_0 in a topologically trivial state. This is true when, $M/2B < 0$. It is possible to induce a topologically non-trivial state by using a drive of appropriate frequency. These Floquet topological

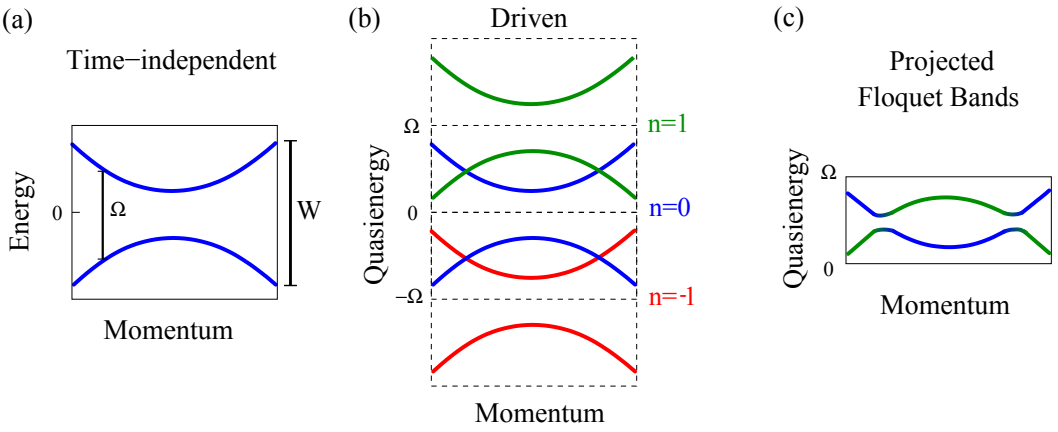

Figure 3.2: Figure shows the schematic for obtaining the quasi-energies of the driven Hamiltonian. (a) shows example of a time-independent bandstructure in momentum space. For clarity, we show a slice of the spectrum only along a particular momentum direction. (b) shows three replicas (labeled as $n = -1$, 0, and 1, representing three Floquet blocks) of the bandstructure. The replicas are obtained by shifting the time-independent bands by $n\Omega$. This represents the spectrum from the diagonal blocks of H_r^F as shown in Eq. (3.24). Adjacent Floquet blocks have resonant quasienergies. (c) shows the approximate quasienergy bandstructure for the Floquet Hamiltonian, obtained by projecting to quasienergies (ϵ) in the range $0 < \epsilon < \Omega$. Clearly, the quasienergy bands correspond to the two resonant bands (Blue and Green) in (b). The radiation potential opens up a gap at the resonance, with the gap proportional to $|\mathbf{V}_\perp|$ (see Eq. 3.27).

insulators have non-zero Chern number. This is because we have broken time-reversal symmetry by choosing only one block of the full BHZ model. Note that, within the four band model, it is possible to obtain an FTI with time-reversal symmetry.

Explicitly, using Eq. (3.9), the Floquet Hamiltonian has the following form,

$$H^F = \begin{pmatrix} \ddots & & \vdots & & \iddots \\ \frac{1}{2}\mathbf{V}\cdot\boldsymbol{\sigma} & \mathbf{d}(\mathbf{k})\cdot\boldsymbol{\sigma} - \Omega & \frac{1}{2}\mathbf{V}\cdot\boldsymbol{\sigma} & 0 & \\ 0 & \frac{1}{2}\mathbf{V}\cdot\boldsymbol{\sigma} & \mathbf{d}(\mathbf{k})\cdot\boldsymbol{\sigma} & \frac{1}{2}\mathbf{V}\cdot\boldsymbol{\sigma} & 0 \\ & 0 & \frac{1}{2}\mathbf{V}\cdot\boldsymbol{\sigma} & \mathbf{d}(\mathbf{k})\cdot\boldsymbol{\sigma} + \Omega & \frac{1}{2}\mathbf{V}\cdot\boldsymbol{\sigma} \\ \iddots & & \vdots & 0 & \ddots \end{pmatrix}, \tag{3.24}$$

with each row and column corresponding to a particular Floquet index.

The Floquet topological phase is induced in a trivial BHZ Hamiltonian (i.e. $M/2B < 0$) through a resonance in the band-structure. Let us consider the case when the radiation potential induces a single resonance in the bandstructure. This happens

when the driving frequency satisfies $\left\{M, \frac{W}{2}\right\} < \Omega < W$, where W is the bandwidth of the time-independent Hamiltonian, H_0. The quasienergy spectrum has a resonance when

$$|\mathbf{d}(\mathbf{k})| = \Omega/2, \tag{3.25}$$

which corresponds to a circle in the Brilluoin zone. Intuitively, in the perturbative limit, $|\mathbf{V}|/\Omega \ll 1$, the radiation potential creates a quasienergy gap at the resonance circle. This can be understood from the schematic diagrams in Fig. 3.2. Consider a system, H_0 with energy bandstrucutre as shown in Fig. 3.2 (a). To obtain the quasienergy spectrum for the driven system (Eq. (3.22)), we first make copies of the bandstructure by translating the original spectrum by Ω as shown in Fig. 3.2(b). The resonant quasienergies are modified strongly by the radiation potential, $\mathbf{V} \cdot \boldsymbol{\sigma}$, resulting in a quasienergy gap. Then, the quasienergy (ϵ) spectrum is obtained by projecting to one Floquet zone, $0 < \epsilon < \Omega$, as shown in Fig. 3.2 (c).

The Floquet Hamiltonian can now be rewritten in an effective two band Hamiltonian[69],

$$H^F_{\text{eff}} = \frac{\Omega}{2}\mathbb{1} + \left(|\mathbf{d}(\mathbf{k})| - \frac{\Omega}{2}\right)\hat{d}(\mathbf{k}) \cdot \boldsymbol{\sigma} + \frac{1}{2}\mathbf{V}_\perp.\boldsymbol{\sigma}, \tag{3.26}$$

$$\text{where, } \mathbf{V}_\perp(\mathbf{k}) = \mathbf{V} - \left(\mathbf{V}.\hat{d}(\mathbf{k})\right)\hat{d}(\mathbf{k}). \tag{3.27}$$

The Pauli matrices, $\boldsymbol{\sigma}$ are defined in the basis of the projected quasienergy bands (see Fig. 3.2) which we label as $\{|\psi^F_\pm(\mathbf{k})\rangle\}$. These bands have a gap at the resonance circle, $V_g = |\mathbf{V}_\perp(\mathbf{k})|$.

We obtain the eigenvalues of the Floquet Hamiltonian, defined in Eq.(3.24), in a cylindrical geometry. The spectrum for an example system is shown in Fig. 3.3. Fig 3.3 (a) shows the time-independent bandstructure in the trivially insulating phase. Fig 3.3 (b) shows the quasienergy bandstructure obtained using a resonant drive aligned along z direction, $\mathbf{V}/M = 1\hat{z}$. The presence of chiral edge-modes in the quasienergy band-gap confirms the non-trivial topology in the driven system.

Now, we can define the topological invariant for these bands, the Chern number (C). It is defined using the unit vector, $\hat{n}(\mathbf{k}) = \langle\psi^F_-(\mathbf{k})|\boldsymbol{\sigma}|\psi^F_-(\mathbf{k})\rangle$, with

$$C = \pm\frac{1}{4\pi}\int d^2\mathbf{k}\ \ \hat{n}(\mathbf{k}) \cdot \left(\partial_{k_x}\hat{n}(\mathbf{k}) \times \partial_{k_y}\hat{n}(\mathbf{k})\right), \tag{3.28}$$

where k_x and k_y are integrated over the first Brilluoin zone. A sufficient condition for the Chern number, C, to be non-zero is for the unit vector, $\hat{n}(\mathbf{k})$, on the resonance

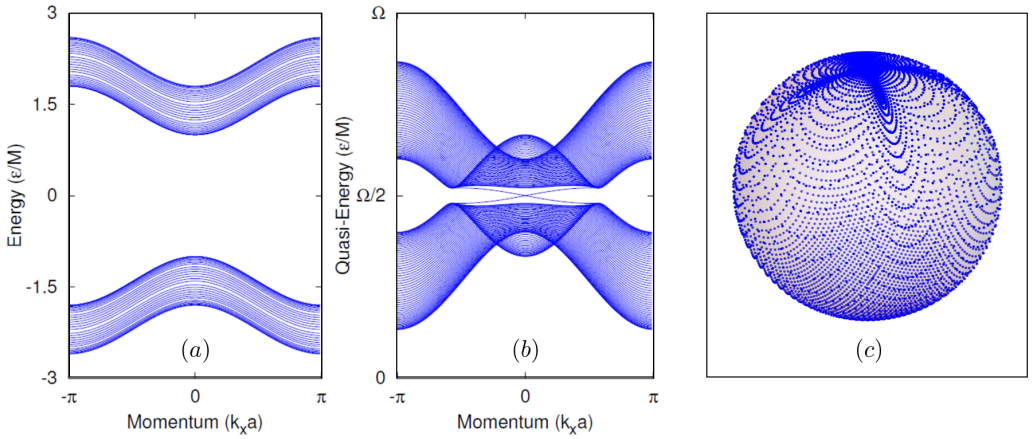

Figure 3.3: The bandstructure for the model Hamiltonian (defined in Eq. (3.22)) in different parameter regimes. (a) The original time-independent band-structure for the Hamiltonian for the parameter regimes: $A/M = 0.2$, $B/M = -0.2$. The band is topologically trivial. (b) The quasienergy bandstructure in the presence of driving for the same system parameters as (a), with $\mathbf{V}/M = (0, 0, 1)$ and $\Omega/M = 3$. This band-structure is clearly non-trivial with edge states in the gap at the resonant quasienergy, $\epsilon = \Omega/2$. (a) and (b) are plotted for the system in cylindrical geometry : periodic boundary conditions in the x direction and open boundary conditions with $L = 60$ sites in the y direction. (c) The spin texture of the lower band of the effective two-band model, H^F_{eff}, as defined in Eq. (3.27), defined in a torus geometry. This is the mapping of the unit vector $\hat{n}(\mathbf{k})$ from the Brilluoin zone to the unit sphere. The parameters are chosen to be the same as (b). Clearly it wraps around the full sphere, indicating a phase with non-zero Chern number.

circle to winds around the north pole [69], where

$$\hat{n}(\mathbf{k}) = \mathbf{V}_\perp(\mathbf{k})/|\mathbf{V}_\perp(\mathbf{k})|, \tag{3.29}$$

As a consequence, when $\hat{n}$ has zero winding along the resonance circle, the induced phase is trivial. Therefore, in the presence of driving, it is possible to obtain trivial Floquet insulators. For, example, when the radiation potential is along z direction, i.e. $\mathbf{V} = V_z\hat{z}$, the driven phase is always topological. In contrast, for $\mathbf{V} = V_x\hat{x}$, the driven system is trivial. In Fig. 3.3 (c) we plot the mapping of the unit vector $\hat{n}$ on the unit sphere, $\hat{n}(\mathbf{k}) : T^2 \to S^2$. Clearly, this wraps around the sphere indicating a topological phase.

3.4 Floquet Chern insulators with $C > 1$

The parameters of the drive can be chosen in such a way to induce Floquet topological phases with higher Chern numbers. We discuss two examples. First we elaborate

on the driven honeycomb lattice. Unlike Section 3.2, in this case we consider the scenario where the drive induces a resonance in the bandstructure. This leads to a novel topological phase with higher Chern numbers. Secondly we discuss the case of using elliptically polarized radiation on the BHZ model. We show that a topological phase with Chern number, $C = 2$ is induced.

Floquet Haldane model with a resonance

Let us consider the tight-binding model on a honeycomb lattice with a energy bandwidth, W. This scenario corresponds to a driving frequency in the regime $W/2 < \Omega < W$. In this case, the quasienergy band-structure has two gaps at (i)$\epsilon = 0$, and (ii) $\epsilon = \pm\Omega/2$, where the topologically non-trivial features may be measured. This is shown in Fig. 3.1 (c). Clearly the band-structure has two radiation induced bulk gaps at these quasienergies. The gap at $\epsilon = 0$ is the same as that discussed in Section 3.2 and is equal to Δ. We incorporate the effect of off-resonant processes on the quasienergy band-structure by making the replacement $H_0 \to H_{\text{eff}}$ in the Floquet Hamiltonian defined in Eq. (3.9). For quasi-energies close to resonance, $\epsilon \sim \Omega/2$, adjacent diagonal Floquet blocks, H_{eff}, and $H_{\text{eff}} - \Omega$, are nearly degenerate. Just like in Section 3.3, H_F must be diagonalized in this subspace of two adjacent Floquet blocks, to obtain the correction to the quasi-energies. The effective two band Hamiltonian is given by

$$(H_r^F)_{\text{eff}} = P_\Omega \begin{pmatrix} H_{\text{eff}} - \Omega & V_+ \\ V_- & H_{\text{eff}} \end{pmatrix} P_\Omega, \tag{3.30}$$

where P_Ω is the projector onto the bands with quasi-energies in the range $0 < \epsilon < \Omega$. This is exactly the same as degenerate first order perturbation theory, and therefore, the gap exactly at resonance, $\epsilon = \Omega/2$, is proportional to $|V_\pm|$.

The quasi-energies of H_r^F are periodic in Ω. As discussed in Section 3.2, to properly define the Chern number for a band (C), we must specify its upper (ϵ_u) and lower (ϵ_l) bound in quasi-energies. An alternative is to measure the Chern number (C^{trunc}) of all bands below a particular quasienergy, for a truncated H_r^F as defined in Eq. (3.24). This means to set, $\epsilon_l = -\infty$. It has been shown [94] that the Chern number for the truncated Hamiltonian, C_n^{trunc}, corresponds to the number of edge states that will be observed at that particular quasienergy irrespective of chirality. For the case of single resonance, the Chern number of the truncated H^F for $M < \Delta$ is

$$C^{\text{trun}} = \begin{cases} 1 & \text{if } \epsilon = 0 \\ 2 & \text{if } \epsilon = \pm\Omega/2, \end{cases} \tag{3.31}$$

and for $M > \Delta$

$$C^{\text{trun}} = \begin{cases} 0 & \text{if } \epsilon = 0 \\ 2 & \text{if } \epsilon = \pm\Omega/2. \end{cases} \tag{3.32}$$

The Chern number of the bands (when $\epsilon_l = \pm\Omega/2$ and $\epsilon_u = 0$) are $C = \pm 3$ when $M < \Delta$, and $C = \pm 2$ when $M > \Delta$.

Floquet Chern insulator : BHZ model under elliptically polarized light

Let us now discuss an example of a Floquet Chern Insulator obtained in the Trivial BHZ model, in the presence of elliptically polarized radiation. This method uses a periodically modulated planar electric field, that is introduced through a spatially uniform gauge potential, $\mathbf{A} = (A_x \sin(\Omega t), A_y \cos(\Omega t))$. In this case, $\mathbf{V}$ is dependent on the momentum vector, $\mathbf{k}$. As a consequence, the topological phase has a Chern number, $C = 2$ with co-propagating edge-modes.In the following, we outline the key steps to show that the quasienergy bandstructure is non-trivial.

In the presence of elliptically polarized light, the time reversal symmetry is explicitly broken. Through the rest of the section, we will only focus on only one block (upper) of the BHZ model as defined in Eq. (3.22) (with $V = 0$). The results can be generalized to the lower block by an appropriate time-reversal operation on the lower block. Let us introduce polarized light through a Peierls substitution of a time-dependent gauge field $\mathbf{A} \equiv (\phi_x, \phi_y) = \Big(A_x \sin(\Omega t), A_y \cos(\Omega t)\Big)$, where A_x and A_y are in general different, indicating an elliptic polarization. The Hamiltonian transforms under this substitution, $\mathbf{d}(\mathbf{k})\cdot\boldsymbol{\sigma} \to \mathbf{d}(\mathbf{k}-\mathbf{A})\cdot\boldsymbol{\sigma} \equiv \tilde{\mathbf{d}}\cdot\boldsymbol{\sigma}$, and the individual components of the vector, $\tilde{\mathbf{d}} \equiv \left(\tilde{d}_x, \tilde{d}_y, \tilde{d}_z\right)$, are

$$\begin{aligned} \tilde{d}_x &= A\left[\sin k_x \cos\phi_x - \cos k_x \sin\phi_x\right], \\ \tilde{d}_y &= A\left[\sin k_y \cos\phi_y - \cos k_y \sin\phi_y\right], \\ \tilde{d}_z &= M - 2B[2 - (\cos k_x \cos\phi_x + \sin k_x \sin\phi_x, \\ &\qquad + \cos k_y \cos\phi_y + \sin k_y \sin\phi_y)]. \end{aligned} \tag{3.33}$$

In the perturbative limit for the radiation field, $A_{x,y} \to 0$, we can set, $\cos(\phi_{x,y}) \approx 1$ and $\sin(\phi_{x,y}) \approx \phi_{x,y}$. This simplifies the Hamiltonian, $H(t)$,

$$H(t) = \mathbf{d}\cdot\boldsymbol{\sigma} + \mathcal{V}\cdot\boldsymbol{\sigma}e^{i\Omega t} + \mathcal{V}^\dagger\cdot\boldsymbol{\sigma}e^{-i\Omega t}, \tag{3.34}$$

where

$$\mathcal{V} = \left(\frac{iAA_x}{2}\cos k_x, -\frac{AA_y}{2}\cos k_y, B(A_y \sin k_y - iA_x \sin k_x)\right). \tag{3.35}$$

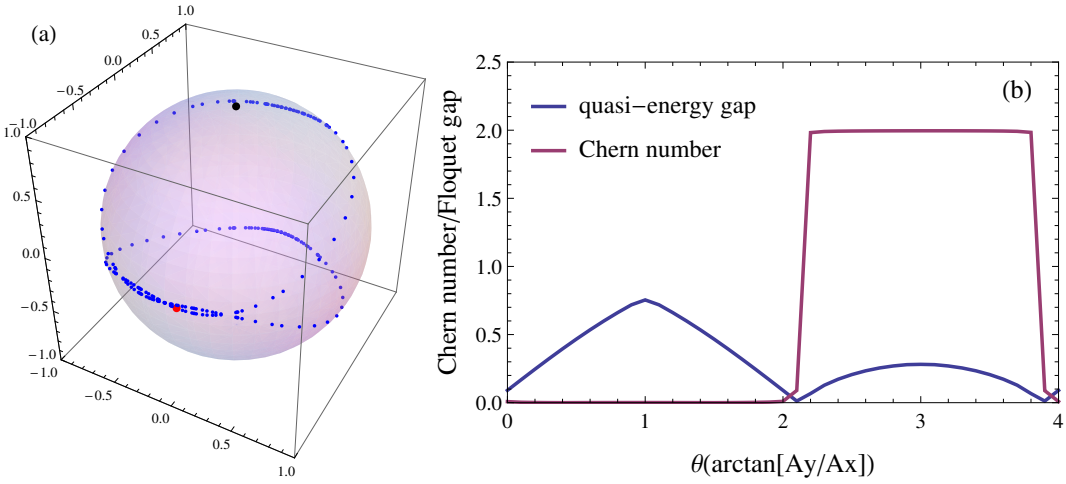

Figure 3.4: (a)Winding of $\mathbf{V}_\perp(\mathbf{k})$ on the unit sphere [See Eqs. (3.39-3.41)] as the momentum vector, $\mathbf{k}$ varies along the resonance circle [defined in Eq. (3.25)]. The black point indicates the north pole, $(0, 0, 1)$ and the red point indicates $\hat{V}_\perp(\mathbf{k}_0)$ with $\mathbf{k}_0 = (1, 0)$.(b) We show the dependence of the Chern number and the gap in the quasienergy bandstructure of the upper block on polarization of light parameterized by, $\theta_{\rm pol} = \arctan(A_y/A_x)$.

As discussed in Section 3.3, the quasienergy gap at resonance is governed by the matrix element, $|\langle\psi_+|\mathcal{V}\cdot\boldsymbol{\sigma}|\psi_-\rangle|$, where $|\psi_\pm\rangle$ are the eigenstates of the unperturbed Hamiltonian. In the original basis, the eigenstates are,

$$|\psi_+\rangle = \cos\frac{\theta}{2}|\uparrow\rangle + \sin\frac{\theta}{2}e^{i\phi}|\downarrow\rangle, \tag{3.36}$$

$$|\psi_-\rangle = \sin\frac{\theta}{2}|\uparrow\rangle - \cos\frac{\theta}{2}e^{i\phi}|\downarrow\rangle, \tag{3.37}$$

where $\mathbf{d}(\mathbf{k}) \equiv |\mathbf{d}|(\sin\theta\cos\phi, \sin\theta\sin\phi, \cos\theta)$, and the original basis is defined as, $\{|\uparrow\rangle, |\downarrow\rangle\}$. As discussed in Section 3.3, the winding around the north pole, $\mathbf{V}_\perp$ (see Eq. 3.27) is necessarily related to the Chern number of the Floquet bands. In the basis of the eigenstates of the time-independent Hamiltonian, $\mathbf{V}_\perp$ is defined as,

$$\mathbf{V}_\perp\cdot\boldsymbol{\sigma} \equiv \langle\psi_+|\mathcal{V}\cdot\boldsymbol{\sigma}|\psi_-\rangle|\psi_+\rangle\langle\psi_-| + \text{h.c.} \tag{3.38}$$

Rewriting the vector, $\langle\psi_+|\mathcal{V}|\psi_-\rangle = \mathcal{V}_R + i\mathcal{V}_I$ in the original pseudospin basis,

$\{|\uparrow\rangle, |\downarrow\rangle\}$,

$$\begin{aligned}\mathbf{V}_\perp &= \mathcal{V}_R(-\cos\theta\cos\phi, -\cos\theta\sin\phi, \sin\theta) \\ &\quad +\mathcal{V}_I(-\sin\phi, \cos\phi, 0),\end{aligned} \tag{3.39}$$

with,

$$\begin{aligned}\mathcal{V}_R &= \frac{AA_x}{2}\sin\phi\cos k_x + \frac{AA_y}{2}\cos\theta\sin\phi\cos k_y \\ &\quad +BA_y\sin k_y\sin\theta,\end{aligned} \tag{3.40}$$

$$\begin{aligned}\mathcal{V}_I &= -\frac{AA_x}{2}\cos\theta\cos\phi\cos k_x - \frac{AA_y}{2}\cos\phi\cos k_y \\ &\quad -BA_x\sin k_x\sin\theta.\end{aligned} \tag{3.41}$$

Note that the angles θ and ϕ are obtained from the definitions of $\mathbf{d}(\mathbf{k})$. We are interested in $\mathbf{V}_\perp$ along the resonance circle given by $|\mathbf{d}(\mathbf{k})| = \frac{\Omega}{2}$.

The Chern number of the bands obtained from irradiation of the quantum wells with circularly polarized light is ± 2. Figure 3.4 (a) shows the winding of the vector $\mathbf{V}_\perp$ along the resonance circle. Clearly, it winds twice around the north pole, which is consistent with a Chern number = ± 2. The Chern number of the band also depends on the polarization of the incident light as shown in Fig. 3.4 (b). The approximate value of the Chern number for a given polarization angle, $\theta_{\text{pol}} = \arctan(A_y/A_x)$, is obtained by computing C defined in Eq. (3.28). The quasienergy gap in the band structure depends on the incident polarization of the radiation, given by $|\mathbf{V}_\perp|$. Clearly, the gap closes as function of θ_{pol}, when a transition happens from a topological ($C = 2$) to the trivial ($C = 0$) phase.

3.5 Floquet TI in Photonic Lattices

The topological band-structure corresponding to the Floquet Haldane model in Section 3.2 was experimentally demonstrated in a structure composed of an array of coupled waveguides (a "photonic lattice"). The schematic structure of this photonic lattice is shown in Fig. 3.5. There, the diffraction of light is governed by the paraxial Schrödinger equation, wherein the spatial coordinate along the waveguide axis acts as a time coordinate. The guided modes of the waveguides are analogous to atomic orbitals, and thus, the diffraction is governed by a tight-binding model. By fabricating the waveguides in a helical fashion, z-reversal symmetry is broken, resulting in a photonic Floquet topological insulator [92], with topologically-protected edge states.

The equation describing the paraxial diffraction of light through an array of waveg-

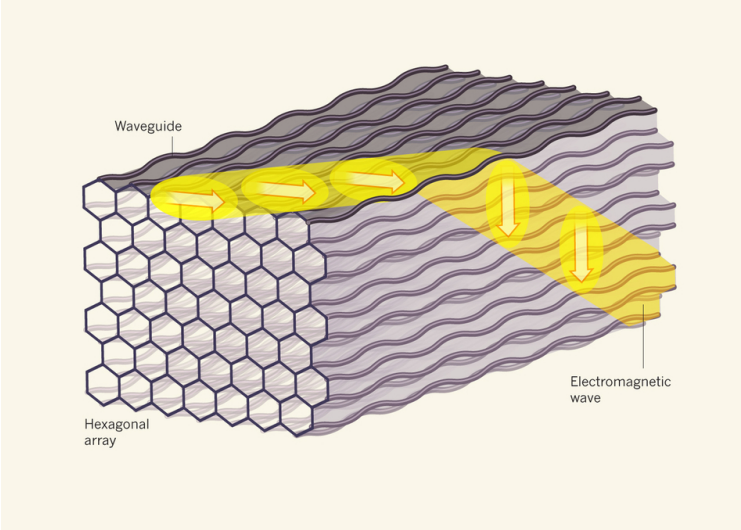

Figure 3.5: Schematic representation of the photonic lattice of the Floquet-Haldane model as realized by Rechtsman et al. [92]. The $\hat{z}$ direction of the waveguides acts as time. The optical waveguides are fabricated in a helical fashion which is equivalent to introducing a circularly polarized radiation. This system realizes a topological phase as shown by the schematic propagation of a light wavepacket on the boundary of the system. (Chong [15])

uides is a Schrodinger equation [92],

$$i\partial_z \psi(x, y, z) = -\frac{1}{2k}\nabla_\perp^2 \psi - \frac{k\Delta n(x, y, z)}{n_0}\psi, \tag{3.42}$$

where z is the distance of propagation along the waveguide axis; k is the ambient wavenumber in the medium; $\nabla_\perp^2$ is the Laplacian in the transverse (x, y) plane; n_0 is the refractive index of the ambient medium, and $\Delta n(x, y, z)$ is the refractive index variation as a function of position that describes the waveguides. In the experiments, the ambient medium was fused silica, $n_0 = 1.45$, with the variation, $\Delta n = 7 \times 10^{-4}$. The waveguides are helical in shape, with a period $2\pi/\Omega$ and radius R. This corresponds to solving Eq. (3.42) in transformed coordinate, $x' = x + R\cos(\Omega z)$, $y' = y + R\sin(\Omega z)$. This transformation is identical to introducing a gauge potential in the Schrödinger equation by the Peierls substitution. Therefore, the z propagation of light through this array is identical to the time-evolution of a single electron wavepacket in a two-dimensional lattice in the presence of circularly polarized radiation.

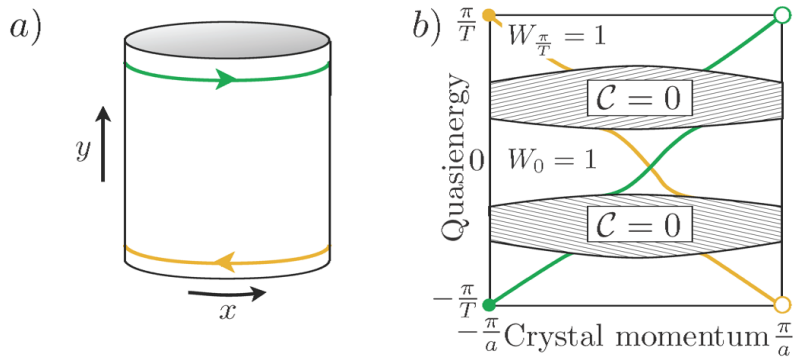

Figure 3.6: Properties of the Anomalous Floquet topological phase as introduced by Rudner et al. [94]. (a) Real space geometry of the system. In a cylinder geometry, chiral edge state propagate along the upper (green) and lower (yellow) boundaries, only at quasi-energies within the bulk gaps where all Floquet bands have Chern number zero but the winding number 3.45 is non-zero in all gaps. b) The corresponding spectrum, shown as a function of the conserved circumferential crystal momentum component. The corresponding edge states wind around the quasienergy zone.

3.6 Anomalous Floquet Topological phases

Periodically driven Hamiltonians may realize topological phases that have no analogs in time-independent Hamiltonians. Forexample, a two-dimensional driven system can support chiral edge states even if all of its bulk Floquet bands have zero Chern numbers [52, 94]. This situation stands in sharp contrast with that of static two-dimensional systems, where the existence of chiral edge states is intimately tied to the topological structure of the system's bulk bands, as captured by their Chern numbers [107]. This is because unlike time-independent systems, in a periodically driven system, the quasienergy spectrum is periodic with the drive frequency, Ω.

Let us consider the example of the anomalous Floquet topological phase introduced by Rudner et al. [94]. The schematic spectrum for this topological phase in a cylindrical geometry is shown in Fig. 3.6. The bulk Floquet bands have Chern number $C = 0$, and so appear trivial. But there exists topologically protected edge states that wind around the quasienergy zone at $\epsilon = \pm\Omega/2$. As we discuss in this section, the signature of the bulk topology of these anomalous Floquet phases are in the full time-dependent time-evolution operator, $U(t)$ and not just the Floquet Hamiltonian, H^F. A system exhibiting this anomalous behavior was recently realized using microwave photonic networks [27, 39].

Let us discuss an explicit model that realizes the anomalous Floquet topological

phase. We consider the system on a square lattice, introduced in Ref. [94]. The time-periodic, piecewise-constant Hamiltonian is of the form

$$H(t) = H_n, \text{ for, } \frac{(n-1)T}{5} \leq t < \frac{nT}{5}, \quad n = 1, \ldots, 5. \tag{3.43}$$

The square lattice is divided into two sublattices, A and B (shown as filled and empty circles in Fig. 3.7). During each of the first four segments of the driving, $n = 1, \ldots, 4$, hopping matrix elements of strength J between the A and B sublattices are turned on and off in a cyclic, clockwise fashion, as shown in Fig. 3.7 (a): during segment $n = 1$, 2, 3, or 4, each site in the A sublattice is connected by hopping to the site left, above, to the right, and below, respectively. In the fifth segment of the period, all the hoppings are set to zero, and an on-site potential $\delta_{A,B}$ is applied on the A and B sublattice sites, respectively.

We choose the hopping strength J such that $\frac{JT}{5} = \frac{\pi}{2}$. For this value of J, during each hopping segment of the driving period a particle that starts on one of the sites hops to the neighboring site with unit probability. Let us consider the case when the on-site potential, $\delta_{A,B} = 0$. With the parameter values chosen above, it is easy to find the Floquet eigenstates and quasi-energies of the time-dependent Hamiltonian $H(t)$. The bulk spectrum consists of states only with quasienergy $\epsilon = 0$, as shown in the spectrum in Fig. 3.7 (c). The corresponding Floquet eigenstates are localized on either the A or the B sublattice. Over each driving period, a particle initially localized on either an A or a B site in the bulk encircles a single plaquette and returns to its original position, see blue arrow in Fig. 3.7 (b). Now consider the case when the on-site potential, applied only while all hopping matrix elements are turned off, is chosen to be $\delta_{A,B} = \pm\frac{\pi}{2T}$. The bulk spectrum consists of two flat Floquet bands with quasi-energies $\pm\frac{\pi}{2T}$, with the Floquet eigenstates localized on either the A or B sublattices. Finally, consider the case, where the sub-lattice on-site potential is non-zero and independent of time. In this case, the bulk Floquet states are no longer localized. The model is not solvable analytically, but can be solved numerically. The spectrum is similar to that shown schematically in Fig. 3.6 (b).

In a cylindrical geometry, motion along the edge is also easily visualized: particles on the first row of sites in the A (B) sublattice along the upper (lower) edge shift one unit cell to the left (right), as shown by the green (red) arrow on the upper (lower) edge in Fig. 3.7 (b). The corresponding eigenstates are therefore plane waves, localized on the first row of sites in the A (B) sublattice along the upper (lower) edge. The two edges therefore host linearly dispersing chiral modes in the quasienergy gaps between the two bulk bands.

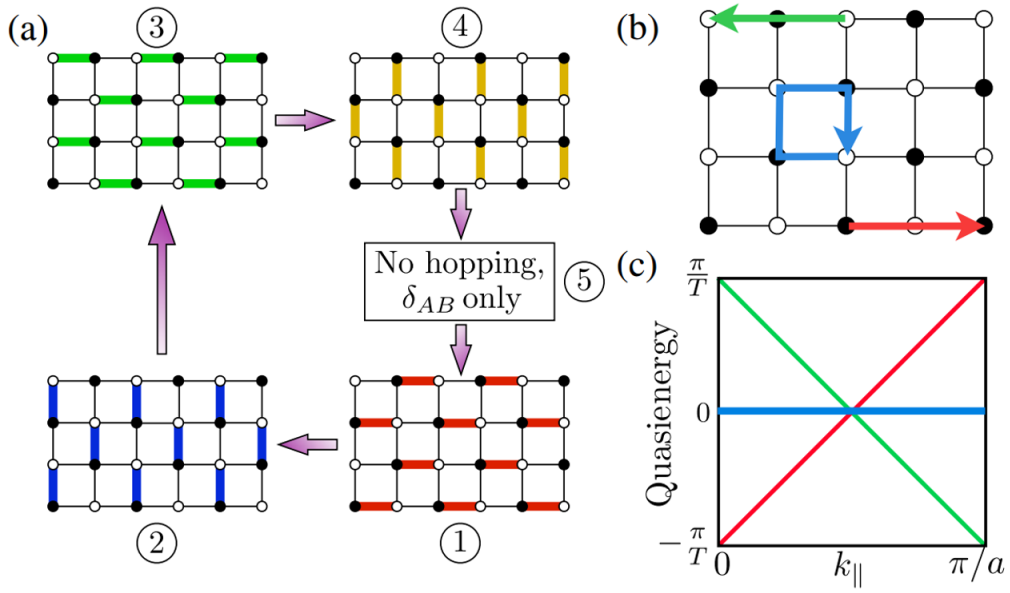

Figure 3.7: Simple explicit model for achieving the anomalous Floquet topological phase [94]. (a) The Hamiltonian is piecewise constant, defined in five equal length segments of duration $T/5$. During steps 1˜4, nearest-neighbor hopping is applied along the colored bonds as shown. The hopping strength J is chosen such that a particle hops between adjacent sites with probability one during each step. In the fifth step, all hopping is turned off and a sublattice potential δ_{AB} is applied. (b) Schematic propagation of a particle in a cylindrical geometry. Over one driving period, a particle initialized on any site in the bulk returns precisely to its original position (blue arrow). Along the upper edge, a particle initialized on the A sublattice shifts two sites to the left (green straight arrow) and similarly a particle initialized on the B sublattice shifts two sites to the right (red straight arrow). (c) shows the quasienergy spectrum for this model in this cylindrical geometry. All bulk states have zero quasienergy. The edge states have finite quasienergy, and they wrap around the quasienergy zone.

We now describe the bulk topological invariant that describes the anomalous Floquet topological phases. Consider a generic disordered two-dimensional system with a time-periodic Hamiltonian $H(t) = H(t+T)$. The associated evolution operator is a time-ordered integral, $U(\mathbf{k},t) = \mathcal{T} e^{-i\int_0^t H(\mathbf{k},t')dt'}$. As a first step in constructing the bulk topological invariant, we define an associated, "deformed" time-periodic evolution operator for the system on a torus:

$$\mathcal{U}_\epsilon(\mathbf{k},t) = U(\mathbf{k},t)\exp\left(iH_\epsilon^{\text{eff}}(\mathbf{k})t\right), \tag{3.44}$$

with $H_\epsilon^{\text{eff}}(\mathbf{k}) = \frac{i}{T}\log U(\mathbf{k},T)$. Note that, by construction, $\mathcal{U}_\epsilon(\mathbf{k},T) = \mathbb{1}$. The explicit dependence on ϵ in the above definitions comes from the necessary choice of a branch cut for log; we use a definition such that $-i\log e^{i\chi} = \chi$ if $\chi \in [0,\epsilon T)$ and $-i\log e^{i\chi} = \chi - 2\pi$ if $\chi \in [\epsilon T, 2\pi)$.

With these definitions at hand, we can define the "winding number" [94],

$$W_\epsilon = \int_0^T dt \int \frac{d^2\mathbf{k}}{8\pi^2}\text{Tr}\left(\mathcal{U}_\epsilon^\dagger\partial_t\mathcal{U}_\epsilon\left[\mathcal{U}_\epsilon^\dagger\partial_{k_x}\mathcal{U}_\epsilon, \mathcal{U}_\epsilon^\dagger\partial_{k_y}\mathcal{U}_\epsilon\right]\right). \tag{3.45}$$

In Eq. (3.45), we have used the shorthand $\mathcal{U}_\epsilon \equiv \mathcal{U}_\epsilon(\mathbf{k},t)$, and W_ϵ is an integer, which can in principle depend on the quasienergy ϵ. Note that in order for W_ϵ to be well defined, the quasienergy ϵ has to remain in a spectral gap of $U(\mathbf{k},T)$.

The winding number, W_ϵ counts the number of Floquet edge modes that exists on a given edge at the quasienergy ϵ when considered in the cylindrical geometry. Therefore, in Fig. 3.6, we consider a system with $W_{\pm\frac{\pi}{T},0} = 1$. The bulk Chern number between two quasienergies, ϵ_l and ϵ_u is $C_{\epsilon_u\epsilon_l} = W_{\epsilon_u} - W_{\epsilon_l}$.

3.7 Summary

In this chapter, we introduced several different Floquet topological phases. We discussed the driven analog of the Haldane model, realized in systems with circularly polarized radiation. This proposal is quite relevant experimentally, as these phases have been observed in photonic lattices and ultra cold fermions in optical lattices. We also introduce models for Floquet topological insulators in the driven BHZ models. Both models, are also host to phases with higher Chern numbers in the presence of driving. Finally, we discussed Anomalous Floquet phases. These phases are unique to periodically driven systems. In Part II, we study all three of the models in the presence of disorder. We are able to show that disorder induces novel topological phases in these systems. Sect

Part II

Disorder in periodically driven Hamiltonians

What are the effects of quenched disorder on topological Floquet systems? Could disorder give rise to new topological phases in periodically driven systems? These are precisely the questions we consider in this part.

We are primarily interested in the interplay of disorder and topological behavior. In two-dimensional TIs, it has been shown [85] that ballistic edge modes are robust to disorder as long as there is a bulk mobility gap. Does this notion generalize to Floquet topological Insulators (see Chapter 3)? First we consider the semiconductor quantum well models [69] for the FTI. In this 2D model, the periodic drive creates a momentum-space ring of resonances between the valence and conduction bands. This effectively induces a band-inversion that leads to a topological phase. When disorder is present, and momentum conservation is no longer applicable, however, it is not at all clear that the band inversion argument survives. In Chapter 5 , we first demonstrate the robustness of the Floquet topological insulator in quantum wells to disorder and the survival of the edge modes in the quasienergy gap. Additionally, we find that the level-spacing statistics of the quasi-energies also indicate that the transition to a trivial phase is in the same universality of the quantum-Hall plateau transition.

Disorder can also induce new phases in Floquet systems. Quenched disorder may induce a Floquet topological Anderson insulator (FTAI) phase. This is the driven analog of the Topological Anderson Insulator (TAI) phase that we examined in Section 2.4. The FTAI is realized in an off-resonantly driven honeycomb lattice with broken inversion symmetry [108]. The driven clean system is in a trivial phase, but the introduction of sufficiently large disorder creates a band inversion, and a topological phase. Photonic lattices made of helical waveguides in a honeycomb lattice have realized Floquet topological phases for transmission of light [92], and we expect that the same sytems will provide a realization of the honeycomb FTAI. A similar FTAI phase also exists in the quantum-well models, which opens the way to investigating the FTAI phase in electronic systems. In contrast to the honeycomb lattice model, where the disorder simply modifies the static gaps in the vicinity of the Dirac points, in quantum wells, the disorder renormalizes the radiation potential directly, and modifies it such that the drive produces a topological gap. We explore the FTAI phase in detail in these two models in Chapters 6 and 7.

We also show that the unique topological characteristics of periodically driven systems can lead to qualitatively new phenomena when spatial disorder is introduced. First, it is possible for robust chiral edge states to exist in a two-dimensional driven

system where *all* bulk states are Anderson localized; we refer to such a system as an anomalous Floquet-Anderson insulator (AFAI) [108]. This situation cannot occur in the absence of driving, where the existence of chiral edge states necessarily implies that there must be delocalized bulk states at some energies [36]. Crucially, in an AFAI this relation is circumvented by the periodicity of quasienergy: the edge states persist through *all* quasi-energies, completely wrapping around the quasienergy Brillouin zone. Moreover, the combination of these novel chiral edge states and a fully localized bulk gives rise to an intriguing non-equilbrium topological transport phenomenon: quantized *non-adiabatic* charge pumping. In Chapter 8, we discuss an explicit model that describes the AFAI phase.

Chapter 4

DIAGNOSTICS FOR DISORDERED FLOQUET HAMILTONIANS

In this chapter, we will outline the analytical and numerical methods used to analyze the driven-disordered systems. Let us write down the full time-dependent Hamiltonian for the system as

$$H(t) = H_r(t) + V_{\text{dis}}, \tag{4.1}$$

where $H_r(t)$ is the driven part of the Hamiltonian which is periodic in time with a period T. The disorder potential, V_{dis} is time-independent and as defined in Chapter 1 (Eq. (1.1)). We choose the disorder potential to be diagonal in real-space. In second-quantized notation we have

$$V_{\text{dis}} = \sum_i U_i \mathbb{1} c_i^\dagger c_i, \tag{4.2}$$

U_i is a uniformly distributed number, $[-U_0/2, U_0/2]$, with a variance, $\sigma_{\text{dis}}^2 = U_0^2/12$. We note that the disorder potential is chosen to be proportional to identity in the pseudospin basis.

We generalize the Born approximation (see Section 1.1) to study the disordered Floquet Green function. In Section 4.1, we calculate the perturbative correction due to weak disorder on the quasienergy density of states. Next we discuss the different numerical methods to characterize properties of the disordered periodically driven Hamiltonians. First, in Section 4.2, we outline an approximate method for the real time-evolution of wave-packets. This allows to obtain the single-particle transport properties in the presence of disorder. Second, in Section 4.3, we obtain the quasienergy eigenstates of the Floquet Hamiltonian. We obtain the Floquet Hamiltonian from the stroboscopic time-evolution operator integrated over a single time-period, T. The eigenstates and eigenvalues of the Floquet Hamiltonian provide signatures of localization and the topology of the bulk. The localization-delocalization transition as a function of disorder is examined by computing the quasienergy level-spacing statistics to identify the transitions in these systems. The topological nature of these disordered quasienergy bulk bands are investigated by computing the Bott index [73] for these bands. The Bott index is equivalent to the Chern invariant in the presence of disorder.

4.1 Floquet Born approximation

The correction to the density of states of the quasienergy band-structure in the presence of dilute disorder is obtained perturbatively in the Born approximation. We generalize the method used for time-independent systems, as described in Section 1.1, to the driven Hamiltonian. We obtain the self energy correction to the Floquet Green function as a result of disorder. The clean Floquet Green's function is defined in frequency space,

$$G_r^F(\omega, \mathbf{k}) = \frac{1}{\omega - H_r^F(\mathbf{k})}, \tag{4.3}$$

where H_r^F is the Floquet Hamiltonian corresponding to the periodic Hamiltonian $H_r(t)$ (see Eq. (4.1)). The various components of the Floquet Green function can be computed as discussed in Section 3.1. The disorder potential can now be treated perturbatively using the Born approximation. The disorder-averaged Floquet Green's function is

$$\overline{G_r^F(\mathbf{k}, \omega)} = \frac{1}{\omega - H_r^F - \Sigma^F}, \tag{4.4}$$

where Σ^F is the self-energy correction due to disorder and $\overline{(\cdots)}$ indicates disorder averaging. Generalizing Eq. (1.8) to the Floquet Hamiltonian, the lowest order contribution to the self-energy becomes

$$\Sigma^F(\omega, \mathbf{k}) = \sigma_{\text{dis}}^2 \int \frac{d\mathbf{k}'}{(2\pi)^d} G_r^F(\omega, \mathbf{k}'), \tag{4.5}$$

where the integral in momentum is done over the first Brilluoin zone and d is the dimensionality of the system. The real part of the self-energy renormalizes the various parameters in the Floquet Hamiltonian.

4.2 Numerical methods I: Real-time evolution

This method is used to numerically obtain the disorder-averaged transmission probability at a particular quasienergy. For a given disorder realization, we employ a numerically exact time evolution to determine the sample-dependent propagator as a function of disorder and quasienergy. The sample averaging is then done by repeating the procedure over many realizations.

We initialize the system with a δ-function wavepacket in real space and then, study the spreading of this wavepacket in real space. The bulk or edge properties are determined according to the choice of the initial position of the wavepacket and boundary conditions. While the bulk Green's function is obtained from the Hamiltonian in a torus geometry with periodic boundary conditions in both the x and y directions,

the edge Green's function is obtained in a cylindrical geometry with open boundary conditions along y.

The time evolution operator is defined as a time-ordered product,

$$U(t,\tilde{t}) = \mathcal{T}\exp(-i\int_{\tilde{t}}^{t} H(t')dt'), \tag{4.6}$$

where $H(t)$ is defined in Eq. (4.1). Discretizing time, $\delta T = T/N_{\rm div}$, the time evolution operator for a single time-period becomes,

$$U(T,0) = \prod_{p}^{N_{\rm div}}(p\delta t,(p-1)\delta t). \tag{4.7}$$

The time-evolution operator is obtained numerically using a split operator decomposition. We take advantage of the following facts. The Hamiltonian for the clean system, H_r has translation symmetry and therefore, is diagonal in momentum space. On the other hand, the disorder potential, $V_{\rm dis}$ is diagonal in real-space. For an infinitesimal time-step, δt, the time-evolution operator becomes,

$$\begin{aligned} U(t+\delta t,t) &= \exp\left(-iH(t)\delta t\right) \\ &= e^{-iH_r(t)\delta t/2}e^{-iV_{\rm dis}\delta t}e^{-iH_r\delta t/2} + O(\delta t^3). \end{aligned} \tag{4.8}$$

Since the exponentiation of a diagonal or a small matrix is efficient, this method gives us an accurate way to obtain the exact time-evolution operator efficiently.

Now, consider the time-evolution of a δ-function wavepacket initialized at $\mathbf{x}$, for N time periods. We obtain the the propagator in real space,

$$G(\mathbf{x},\mathbf{x}',NT) = \langle\mathbf{x}'|U(NT,0)|\mathbf{x}\rangle \tag{4.9}$$

$$= \langle\mathbf{x}'|\left(\exp(-iH^F T)\right)^N|\mathbf{x}\rangle, \tag{4.10}$$

where H^F is the Floquet Hamiltonian for the full Hamiltonian, $H(t)$. We note that the propagator for an integer number of time-periods is the same as the propagator obtained from the effective time-independent Floquet Hamiltonian. In order to explore the effect of disorder at different quasi-energies, we need the Fourier transform in time of the real-time propagator,

$$\begin{aligned} G_N(\mathbf{x},\mathbf{x}',\omega) &= \int_0^{NT} dt\ \ G(\mathbf{x},\mathbf{x}',NT)e^{-i\omega t} \\ &= \langle\mathbf{x}'|(\omega - H^F)^{-1}|\mathbf{x}\rangle, \end{aligned} \tag{4.11}$$

where in Eq. (4.11), we Fourier transformed in time to obtain the Floquet Green's function as a function of the quasienergy. The subscript, N, in Eq. (4.11) refers to the total time of evolution, $T_{\text{tot}} = NT$.

In order to study the effect of disorder, we must average the Green's function for a large number of disorder configurations. To the study the transport properties of the system at a given quasienergy we obtain the average transmission probability from $\mathbf{x} \equiv (x, y)$ to $\mathbf{x}' \equiv (x', y')$ as a function of disorder and quasienergy,

$$\tilde{g}_N(\mathbf{x}, \mathbf{x}', \omega) \quad = \quad \overline{\sum_{y'} |G_N(\mathbf{x}, \mathbf{x}', \omega)|^2}, \tag{4.12}$$

where $\overline{(\cdots)}$ denotes disorder averaging and the subscript, N is related to the total time of evolution, $T_{\text{tot}} = NT$. We sum along y' to obtain the transmission probability, g_N in the x direction. The properties of the g_N, are used to identify a localization transition in this system. g_N is first obtained for a strip geometry of size $L_x \times L_y$, with $L_x \gg L_y$. We define a decay length scale along the x direction from the inverse participation ratio of g_N,

$$\frac{1}{\Lambda_N(\omega)} = \frac{\sum_{x'} g_N(\mathbf{x}, x', \omega)^2}{\left(\sum_{x'} g_N(\mathbf{x}, x', \omega)\right)^2}. \tag{4.13}$$

This length-scale must be small in the mobility gap, and allows us to characterize the quasienergy gap as a function of disorder.

Clearly, the decay length scale Λ_N depends on the total time of evolution, $T_{\text{tot}} = NT$. Therefore, the N-dependence of the length scale, $\Lambda_N(\omega)$, reveals the diffusive or ballistic nature of states. Bulk states are diffusive, where as edge states protected from scattering are ballistic. When $\Lambda_N \propto \sqrt{N}$, the state is diffusive, and when $\Lambda_N \propto N$, the state is ballistic in nature. For localized or extended states, in the large N limit, this length scale must saturate, $\lim_{N\to\infty} \Lambda_N = \Lambda_{\text{sat}}$. This saturation length scale corresponds to either the localization length at the quasienergy or the system size corresponding to localized or extended states respectively. Therefore, the finite size scaling of Λ_{sat} reveals the localized or extended nature of these states.

4.3 Numerical methods II: Properties of Floquet eigenstates

The quasienergy spectrum can be numerically obtained very efficiently from the unitary time evolution operator, $U(T, 0)$ for a single time-period. The time-evolution operator is obtained using the procedure described in Section 4.2. Now, the Floquet quasienergy spectrum, and eigenvectors are obtained by diagonalizing, $H^F = \frac{i}{T} \log(U(T, 0))$. Here, the branch cut for the log is chosen such that,

$-i \log e^{i\epsilon T} = \epsilon T \ \ \forall \ \ \epsilon T \in [0, \pi)$ and $-i \log e^{i\epsilon T} = \epsilon T - 2\pi \ \ \forall \ \ \epsilon T \in [\pi, 2\pi)$. For our purposes, it is convenient to rewrite the disorder potential in the momentum space and obtain the eigenvectors in this space. We examine the level spacing statistics of the quasienergies. This reveals the localized or extended nature of the states. To characterize the topology of the Floquet Hamiltonian, we compute the Chern number of the quasienergy bands. It is obtained by calculating the Bott index from the eigenvectors averaged over many disorder realizations.

Quasienergy level spacing statistics.

The eigenvalues of the Floquet Hamiltonian can be used to study the localization-delocalization transition in this system. As discussed in Chapter 1, for time-independent systems the level-spacing statistics of the energies of the Hamiltonian are the signature of localization. This notion can be extended to the Floquet Hamiltonian of a single particle Hamiltonian. This is because, while generic extended eigenstates cannot be degenerate in the quasienergy since they experience level repulsion, localized states far from each other can be arbitrarily close to each other in quasienergy. This leads to different behaviors in the distributions of the level-spacings at these quasi-energies.

We follow the notation to define level spacing distribution defined in Chapter 1. We define the quasienergy level spacing (s_n) in the units of the mean level spacing (δ). The definition is exactly the same as that for energy level spacing which we defined in Sections 1.2 and 1.3. The probability distribution of the level-spacings, $P(s)$, is universal and determined completely by their symmetry classification. For Floquet systems, the ensemble corresponding to broken time-reversal symmetry is the Circular Unitary Ensemble (CUE). This is different from the Gaussian Unitary Ensemble since the quasienergies are defined on a compact manifold. However, the distributions for CUE and GUE are expected to converge to the same distribution in the thermodynamic limit[16]. We compare the quasienergy level-spacing distributions with the analytical form, P_{GUE}[79],

$$P_{\mathrm{GUE}}(s) = \frac{32}{\pi^2} s^2 \exp\left(-\frac{4}{\pi} s^2\right). \tag{4.14}$$

In contrast, for localized states, the level-spacings must follow Poisson statistics,

$$P_{\mathrm{loc}}(s) = \exp(-s). \tag{4.15}$$

We note that, while the GUE distribution has a variance, $\sigma^2(P_{\mathrm{GUE}}(s)) \approx 0.178$, the Poisson distribution has a variance, $\sigma^2(P_{\mathrm{loc}}(s)) \approx 1$.

Floquet Bott Index

The Bott index is a topological invariant that has been defined by Loring and Hastings [73] for disordered systems with broken time-reversal symmetry. For time-independent Hamiltonians, it has also been shown that this index is equivalent to the Hall conductivity of the sample, i.e. the Chern number [37]. We generalize this definition to obtain the disorder-averaged Bott index in periodically driven Hamiltonians.

The Bott index, for periodically driven systems is defined by using the eigenstates of the Floquet Hamiltonian. Consider a band of Floquet states, defined by a projector P, and having quasienergies bounded by, $\epsilon_l < \epsilon < \epsilon_h$. The Bott index, for such a set of states is an integer, that counts the difference in the number of edge states at ϵ_l and ϵ_h[94]. One can define two unitary matrices, $U_X = \exp(i2\pi X/L_x)$ and, $U_Y = \exp(i2\pi Y/L_y)$, where X and Y are diagonal coordinate matrices, $X_{ij} = x\delta_{ij}$ and $Y = y\delta_{ij}$. Here, (i, j) represents two different sites on the lattice. The projector on to this band of Floquet eigenstates, P, can be used to project the unitary matrices, to give almost unitary matrices,

$$\tilde{U}_{X,Y} = PU_{X,Y}P. \tag{4.16}$$

It was shown by Loring and Hastings [73], that these almost unitary matrices, $\tilde{U}^\dagger_{X,Y}\tilde{U}_{X,Y} \approx 1$, are also almost commuting. For brevity, we skip the exact mathematical definitions of almost unitary and almost commuting matrices [73]. The Bott index is a measure of commutativity of these projected unitary matrices, $\tilde{U}_{X,Y}$, and is quantized to integers. Explicitly,

$$C_b = \frac{1}{2\pi}\mathrm{Im}\left[\mathrm{Tr}\left\{\log\left(\tilde{U}_Y\tilde{U}_X\tilde{U}_Y^\dagger\tilde{U}_X^\dagger\right)\right\}\right]. \tag{4.17}$$

This index has been shown to be equivalent to the Kubo formula for the Hall conductivity for time-independent Hamiltonians [37]. The average Bott index at a given quasienergy and disorder strength is obtained by averaging this index over different disorder configurations. While the index is an integer for every particular disorder configuration, there is no such requirement on the average Bott index. In fact, through a topological phase transition due to disorder, the average index smoothly changes from one integer to another [73]. This smooth transition is expected to be sharp in the thermodynamic limit.

Similarly, the Bott index can also be calculated when the Floquet Hamiltonian is defined in the extended zone scheme. In the extended Floquet Hilbert space, we

must generalize the definition for the unitary matrices,

$$\left(U_X^F\right)_{mn} = U_X \delta_{mn}, \tag{4.18}$$
$$\left(U_Y^F\right)_{mn} = U_Y \delta_{mn}, \tag{4.19}$$

where (m, n) refer to a particular Floquet block. Now, we define the projected unitary matrices as,

$$\tilde{U}_{X,Y}^F = P U_{X,Y}^F P. \tag{4.20}$$

For a given disorder configuration, the Bott index of the band is given by Eq. (4.17), with $\tilde{U}$ replaced by $\tilde{U^F}$.

4.4 Summary

In this chapter, different analytical and numerical techniques were introduced. These methods would be used to analyze various driven topological phases in the following chapters of this part. We introduced the real-time evolution of wave packets as a way to study transmission probability through a disordered system. The Floquet states obtained from exactly diagonalizing a finite system also reveal the topological and localization properties of the system. The Chern number for the disordered system is computed using the Bott index. Localization is probed using the level-spacing statistics of the quasienergy spectrum.

Chapter 5

DISORDERED FLOQUET TOPOLOGICAL PHASES

We consider the robustness of the Floquet topological insulator phase to disorder. Specifically, we study the Floquet topolgical phase induced in the trivial BHZ model in the presence of disorder,

$$H_r(\mathbf{k},t) = \mathbf{d}(\mathbf{k})\cdot\boldsymbol{\sigma} + \mathbf{V}\cdot\boldsymbol{\sigma}\cos(\Omega t), \tag{5.1}$$

$$\equiv H_0 + V, \tag{5.2}$$

where $\mathbf{d} = \left(Ak_x, Ak_y, M - B(k_x^2 + k_y^2)\right)$, k_x and k_y being the crystal momentum along x and y directions and $\mathbf{V} = (V_x, V_y, V_z)$. The system is driven periodically at a frequency, Ω. We define the pseudospin basis for the pauli matrices, $\boldsymbol{\sigma} \equiv (\sigma_x, \sigma_y, \sigma_z)$, as $\{|\uparrow\rangle, |\downarrow\rangle\}$. The drive induces a resonance in the time-independent bandstructure, $M < \Omega < W$, where W is the bandwidth of the undriven Hamiltonian, H_0. This model was discussed in detail in Section 3.3, where we calculate the corresponding Floquet Hamiltonian, H_r^F and the quasienergy bandstructure. A topological phase is induced in this system when the radiation potential is in the z direction, $\mathbf{V} \equiv (0, 0, V_z)$. We plot the spectrum of the Hamiltonian, H_0 and the quasienergy spectrum for the driven Hamiltonian, $H_r(t)$ in Fig. 5.1 (a) and (b) respectively.

We study the stability of this topological phase to disorder,

$$H = H_r + V_{\text{dis}}, \tag{5.3}$$

where the disorder, V_{dis} is a uniformly random on-site energy and is time-independent, as defined in Eq. (4.2). The random potential is taken uniformly distributed, $[-U_0/2, U_0/2]$, the variance determining the strength of the disorder potential, $\sigma_{\text{dis}}^2 = U_0^2/12$.

In the following sections we employ the different analytical and numerical methods to study the effect of disorder on the quasienergy spectrum and states. In Section 5.1, we calculate the renormalization of the paramters of the Floquet Hamiltonian, H_r^F, perturbatively in the disorder potential. Specifically, we show that disorder must renormalize the radiation potential, $\mathbf{V}$. Next we employ the different numerical techniques discussed in Chapter 4 to study the topological phase. In Section 5.2,

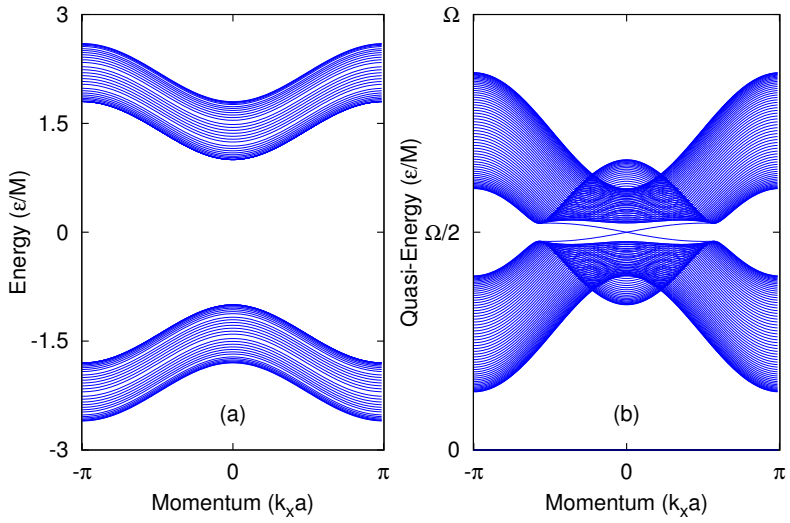

Figure 5.1: The bandstructure for the model Hamiltonian (defined in Eq. (3.22)) in different parameter regimes. (a) The original time-independent band-structure for the Hamiltonian for the parameter regimes: $A/M = 0.2$, $B/M = -0.2$. The band is topologically trivial. (b) The quasienergy bandstructure in the presence of driving for the same system parameters as (a), with $\mathbf{V}/M = (0, 0, 1)$ and $\Omega/M = 3$. This band-structure is clearly non-trivial with edge states in the gap at the resonant quasienergy, $\epsilon = \Omega/2$. They are done on a lattice with periodic boundary conditions in the x direction and open boundary conditions with $L = 60$ sites in the y direction.

we show that topological phase remains robust, as long as the disorder strength is smaller than the quasienergy gap in the spectrum.

5.1 Born approximation in resonantly driven BHZ model

The correction to the density of states of the quasienergy band-structure in the presence of dilute disorder is obtained perturbatively in the Born approximation. We generalize the method used for time-independent systems to the driven Hamiltonian by obtaining the self energy correction to the Floquet Green's function as a result of disorder. The effect of the disorder potential is to renormalize the parameters of the Hamiltonian. To lowest order in the disorder potential, the self-energy corrections to the single particle Floquet Green's function is obtained in the Born approximation. As discussed in Section 3.3, the quasienergy gap at resonance is determined to lowest order by the radiation potential, $\mathbf{V}_\perp$ [see Eq. (3.27)]. Therefore, in the Born approximation, we consider the dominant contribution to the self-energy correction to the radiation potential, Σ_V. This is responsible for the renormalization of the density of states at resonance.

Let us focus on the specific case with the radiation potential $\mathbf{V} = (0, 0, V_z)$, along z direction. We define the self-energy correction to $\mathbf{V}$ as Σ_V. This correction, Σ_V is proportional to $-\sigma_{\text{dis}}^2 \sigma_z$, where σ_{dis}^2 is the variance of the distribution of the disorder potential. Therefore, this term renormalizes (negatively) the magnitude of V indicating that the quasienergy gap must close with disorder. Thus qualitatively, the Born approximation captures the transition from topological to trivial insulator as a result of closing of the quasienergy gap. The Born-approximation, however, fails to capture the transition to an Anderson localized insulator as the gap closes.

In the following, we first describe the formalism to obtain Floquet-Green functions as an expansion in the the radiation potential, $V = \frac{1}{2}\mathbf{V} \cdot \boldsymbol{\sigma}$. Next, we calculate the self energy correction to the Green function in the presence of disorder.

Floquet Green function

We defined the Floquet Green function in Section 3.1. Let us compute the different elements of the Floquet Green function for the clean Floquet Hamiltonian, H_r^F (see Eq. (3.24)). We have

$$G_r^F(\epsilon, \mathbf{k}) = \frac{1}{\epsilon - H_r^F(\mathbf{k})} \tag{5.4}$$

where H_r^F is formally an infinite dimensional matrix, as shown in Eq. (3.24). Now, we obtain an approximate expression for the Green's function in the perturbative regime, where the radiation potential, $|V|/\Omega \ll 1$. We consider parameter ranges which induces only one resonance in the bandstructure, and therefore are concerned with the effect of disorder at quasi-energies near the resonance. A weak resonant drive only mixes adjacent Floquet bands appreciably, and therefore it is sufficient to project this infinite dimensional Floquet Hilbert space to just two adjacent Floquet blocks, say with indices n and $n+1$. The Floquet Hamiltonian defined in Eq. (3.24) reduces to

$$H_r^{F,\text{trunc}} = \begin{pmatrix} H_0 & V \\ V & H_0 + \Omega \end{pmatrix}, \tag{5.5}$$

where we note that H_0 and V defined in Eqs. (5.1) and (5.2) are 2×2 matrices. In Eq. (5.5) choose the two zones to be, $n = 0$ and $n = 1$. The choice of these two zones is arbitrary and not important as these two blocks are equivalent to any other pair of adjacent zones, n and $n + 1$. It only results in a shift of the origin of the quasienergy by $n\Omega$.

Now, we write the components of the Floquet Green's function, G_r^F, order by order in the radiation potential, $V = \mathbf{V} \cdot \boldsymbol{\sigma}/2$. Let us start by defining the matrix

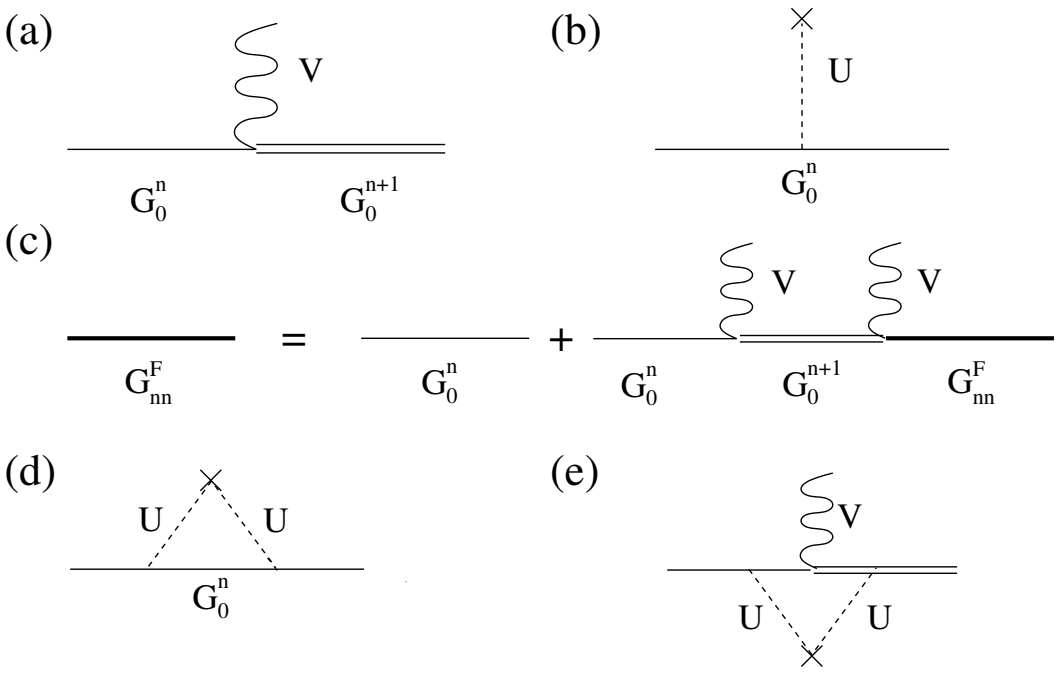

Figure 5.2: This figure illustrates the diagramatic representation different terms in the Floquet Green's function. (a) The vertex of the driving field V. It connects G_0^n with G_0^{n+1}. (b) shows the typical vertex due to the presence of the disorder potential. (c) The Dyson's equation Eq. (5.11) for the clean Floquet Green's function. (d) shows the self energy correction due to disorder to the bare parameters of the Hamiltonian. (e) The Self energy correction to the radiation potential vertex. The change of the density of states near the Floquet gap can be viewed as a renormalization of the radiation potential.

elements of the bare Floquet Green's functions in terms of the the time-independent Hamiltonian, H_0 as

$$[G_0^F(\epsilon, \mathbf{k})]_{mn} = \frac{\delta_{mn}}{\epsilon - H_0 - n\Omega} \tag{5.6}$$

$$\equiv \delta_{mn} G_0^n, \tag{5.7}$$

where$m$ and n index the particular Floquet block. The bare Floquet Freen function, G_0^F is zeroth order contribution to the full Floquet Green function (setting $V = 0$). A analytical expression for the different components of the Green function is known for the Floquet Hamiltonian [53, 78]. We simplify them to the case where only contributions are kept from the two Floquet blocks, $n = 0$ and 1. In this projected subspace, the Floquet Green's function becomes

$$G_r^F \approx G_r^{F,\text{trunc}} = \begin{pmatrix} (G_r^{F,\text{trunc}})_{00} & (G_r^{F,\text{trunc}})_{01} \\ (G_r^{F,\text{trunc}})_{10} & (G_r^{F,\text{trunc}})_{11} \end{pmatrix}, \tag{5.8}$$

where $(G_r^F)_{00}$, $(G_r^F)_{01}$, and $(G_r^F)_{11}$ are obtained from an analogous Dyson's equation in terms of the radiation potential. The Dyson equation for the $(0,0)$ component of the Floquet Green's function is schematically shown in Fig. 5.2 (c). Explicitly, the $(0,0)$ component becomes

$$\begin{aligned}(G_r^{F,\text{trunc}})_{00} &= G_0^0 + G_0^0 V G_0^1 V (G_r^{F,\text{trunc}})_{00} && (5.9)\\ &= G_0^0 + G_0^0 (V G_0^1 V G_0^0 + \cdots) && (5.10)\\ &= \frac{1}{\epsilon - H_0 - V G_0^1 V}, && (5.11)\end{aligned}$$

where in the above equations, we have dropped the contributions of (G_0^n), $n \neq \{0,1\}$. Compared to the exact expression for $(G_r^F)_{00}$, in $(G_r^{F,\text{trunc}})_{00}$, we have dropped the contribution from the terms proportional to powers of $V G_0^{-1} V$. This is because, for quasienergies near resonance between $n = 0$ and 1 blocks, $\epsilon = \Omega/2$, the contributions from terms in the $n = -1$ block are suppressed by $O(1/\Omega)$. Similarly, the other matrix elements of $G_r^{F,\text{trunc}}$ can be obtained

$$\begin{aligned}(G_r^{F,\text{trunc}})_{1,1} &= \frac{1}{\epsilon - H_0 - \Omega - V G_0^0 V}, && (5.12)\\ (G_r^{F,\text{trunc}})_{0,1} &= G_0^0 V \frac{1}{\epsilon - H_0 - \Omega - V G_0^0 V}, && (5.13)\\ &= G_0^1 V (G_r^{F,\text{trunc}})_{1,1}. && (5.14)\end{aligned}$$

Therefore, we now have the Floquet Green's function perturbatively in the radiation potential. We note that the projection to the subspace of two resonant bands only is equivalent to taking the Hamiltonian in the rotating wave approximation in the time-dependent Hamiltonian.

Floquet Born approximation

The disorder potential can now be treated perturbatively using the Born approximation. We write the disorder-averaged Floquet Green's function as

$$\overline{G_r^F(\mathbf{k},\epsilon)} = \frac{1}{\epsilon - H_r^F - \Sigma^F}, \tag{5.15}$$

where Σ^F is the self-energy correction due to disorder and $\overline{(\cdots)}$ indicates disorder averaging. In the Born approximation, the self energy is given by

$$\Sigma^F(\epsilon,\mathbf{k}) = \sigma_{\text{dis}}^2 \int \frac{d\mathbf{k}'}{(2\pi)^2} G_r^F(\epsilon,\mathbf{k}'), \tag{5.16}$$

as discussed in Chapter 4. The contribution of the self energy can be split into different Floquet blocks, similar to the Floquet Green's function as shown in Eq. (5.8). Projecting to two adjacent Floquet blocks, the self energy is

$$\Sigma^{F,\text{trunc}} = \begin{pmatrix} \Sigma_0^F & \Sigma_V^F \\ \Sigma_V^{F\dagger} & \Sigma_1^F \end{pmatrix}, \tag{5.17}$$

where Σ^F renormalizes the Hamiltonian defined in Eq. (5.5). The terms Σ_0^F and Σ_1^F, renormalizes the time-independent Hamiltonian, H_0, and Σ_V^F renormalizes V. Therefore, the effect of disorder on the single-particle Green's function is two fold. First, it renormalizes the parameters of the bare, time-independent Hamiltonian H_0, $M \to \tilde{M}$, and $B \to \tilde{B}$. This is due to the diagonal terms in the Self energy, Σ_0^F and Σ_1^F. Note that, at lowest order, this correction is identical to that from disorder-averaging the Green's function of the time-independent Hamiltonian [see Fig. 5.2 (d)]. This renormalization of the parameters is not important to the modification of the quasienergy density of states near the resonance ($\epsilon \sim \Omega/2$). We assume that this effect can be neglected. The second effect is to renormalize the radiation potential, $\mathbf{V} \to \tilde{\mathbf{V}} = \mathbf{V} + \Sigma_V^F$. Since the magnitude of the Floquet band-gap, V_g, of the Hamiltonian is proportional to $|\mathbf{V}|$, we will primarily be interested in this particular renormalization. Therefore, the diagram shown in Fig. 5.2 (e) is the leading order contribution to the self energy correction to the inter-Floquet block terms of H_r^F [see Eq.(3.24)]. Explicitly, in the Born approximation, using Eqs. (5.14) and (5.16) the self energy correction to the radiation potential becomes,

$$\begin{aligned} \Sigma_V &= \sigma_{\text{dis}}^2 \int_{FBZ} d\mathbf{k}\ \ (G_r^{F,\text{trunc}})_{0,1} && (5.18)\\ &= \sigma_{\text{dis}}^2 \int_{FBZ} d\mathbf{k}\ \ G_0^0 \frac{1}{2}\mathbf{V}\cdot\boldsymbol{\sigma}(G_r^{F,\text{trunc}})_{11} && (5.19)\\ &= \Sigma_V^I \mathbb{1} + \sum_{i=x,y,z} \Sigma_V^i \sigma^i, && (5.20) \end{aligned}$$

where $\overline{U^2} = \sigma_d^2 = \frac{U_0^2}{12}$, is the variance of the uniformly random distribution. In Eq. (5.19), we expand the 2×2 matrix, Σ_V, in Pauli matrices. The components in the expansion, $\Sigma_V^{x,y,z}$ determines the renormalization of the different components of $\mathbf{V} \equiv (V_x, V_y, V_z)$.

Let us now use the form of the Hamiltonian, H_0, defined in Eq. (5.1). We have the

following expressions for the bare Green's functions,

$$G_0^0(\epsilon, \mathbf{k}) = \frac{\epsilon + \mathbf{d}(\mathbf{k}) \cdot \boldsymbol{\sigma}}{\epsilon^2 - |\mathbf{d}(\mathbf{k})|^2}, \tag{5.21}$$

$$G_0^1(\epsilon, \mathbf{k}) = \frac{(\epsilon - \Omega) + \mathbf{d}(\mathbf{k}) \cdot \boldsymbol{\sigma}}{(\epsilon - \Omega)^2 - |\mathbf{d}(\mathbf{k})|^2}, \tag{5.22}$$

where $\mathbf{d}(\mathbf{k}) \equiv (d_x, d_y, d_z) = (A \sin k_x, A \sin k_y, M - 2B(2 - \cos k_x - \cos k_y)$. Using these we have

$$(G_r^{F,\text{trunc}})_{11} = \frac{1}{\epsilon - H_0 - \Omega - V G_0^0 V} \tag{5.23}$$

$$= \frac{\left(\epsilon^2 - |\mathbf{d}(\mathbf{k})|^2\right)\left(\left[(\epsilon-\Omega)\left(\epsilon^2 - |\mathbf{d}(\mathbf{k})|^2\right) - \epsilon|\mathbf{V}|^2\right] + \mathbf{Q}\cdot\boldsymbol{\sigma}\right)}{\left((\epsilon-\Omega)\left(\epsilon^2 - |\mathbf{d}(\mathbf{k})|^2\right) - \epsilon|\mathbf{V}|^2\right)^2 - |\mathbf{Q}|^2}, \tag{5.24}$$

$$\text{with, } \mathbf{Q} = \left(\epsilon^2 - |\mathbf{d}(\mathbf{k})|^2 - |\mathbf{V}|^2\right)\mathbf{d}(\mathbf{k}) + 2\left(\mathbf{V} \cdot \mathbf{d}(\mathbf{k})\right)\mathbf{V}, \tag{5.25}$$

Using the expression for $(G_r^{F,\text{trunc}})_{11}$, we get

$$G_0^0 \mathbf{V} \cdot \boldsymbol{\sigma} (G_r^F)_{11} = \frac{(\epsilon \mathbf{V}\cdot\boldsymbol{\sigma} + (\mathbf{d}(\mathbf{k})\cdot\boldsymbol{\sigma})(\mathbf{V}\cdot\boldsymbol{\sigma}))\left(\left((\epsilon-\Omega)\left(\epsilon^2 - |\mathbf{d}(\mathbf{k})|^2\right) - \epsilon|\mathbf{V}|^2\right) + \mathbf{Q}\cdot\boldsymbol{\sigma}\right)}{\left((\epsilon-\Omega)\left(\epsilon^2 - |\mathbf{d}(\mathbf{k})|^2\right) - \epsilon|\mathbf{V}|^2\right)^2 - |\mathbf{Q}|^2}. \tag{5.26}$$

Now, let us compute the correction due to the disorder potential, when the radiation field is along the z direction, $\mathbf{V} = (0, 0, 2V_z)$. The Floquet Hamiltonian we consider has a particle-hole symmetry around $\epsilon = \Omega/2$. Since the disorder potential has a zero mean, $\overline{U} = 0$, the disorder does not renormalize the 'chemical potential' at $\epsilon = \Omega/2$. Therefore, the gap must close at $\epsilon = \Omega/2$. This is also confirmed numerically in Fig. 5.3 (a). Simplifying, Eqs. (5.24), (5.25) and (5.26), we can write down the expression for the self energy. Only the Σ_V^z survives

$$\Sigma_V^z = \frac{U_0^2 V_z}{48\pi^2} \int d^2\mathbf{k} \frac{d_z^2 - d_x^2 - d_y^2 - \frac{\Omega^2}{4} - V_z^2}{\left(\frac{\Omega^2}{4} - |\mathbf{d}|^2\right)^2 + V_z^4 - 2V_z^2\left(d_z^2 - \frac{\Omega^2}{4} - d_x^2 - d_y^2\right)}, \tag{5.27}$$

where we note that there is no contribution to Σ_V^x, Σ_V^y and Σ_V^I since the integral vainshes. Let us estimate the disorder strength at which the gap closes. We compute the strength of disorder , U_0, when the renormalized radiation potential, $\tilde{V}_z = V_z + \Sigma_V^z$, vanishes. We calculate Σ_V^z in Eq. (5.27) numerically for the parameters, $A = 0.2$, $B = -0.2$, $M = 1, \Omega = 3$, and $V_z = 1$. We obtain that the gap closes for $U_0/M \approx 7.3$. As we see in the next section, this value is different from the value seen numerically in Fig. 5.3 (a). We note that to make the calculation more precise, it is necessary to calculate in the self-consistent Born approximation, where all the parameters in Eq. (5.27) are the disorder renormalized counterparts and not their bare values.

5.2 Numerical Analysis : Destruction of topological order by disorder

In this section, we study the effect of adding on-site quenched disorder to a clean driven system in the Floquet topological phase. To be explicit, we consider the case of the periodically varying Zeeman field, in z direction. This corresponds to setting $V_{x,y} = 0$, in Eq. (5.1), where we are focusing on a single 2×2 block of the full time-reversal invariant 4×4 Hamiltonian. The driving frequency is chosen to induce only a single resonance, such that the Floquet bands have a non-trivial Chern number, $|C| = 1$. Our main contention is this:

> The topological phase is robust to disorder, with gapless edge states, for disorder strengths $\sigma_d \ll V_g$, where V_g is the quasienergy gap. The Floquet gap closes for $\sigma_d \gg V_g$, and all eigenstates are completely localized.

We study the quasienergy spectrum numerically. The numerical simulations were done for Hamiltonian with the parameters $A/M = 0.2$ and $B/M = -0.2$ on a torus with dimensions $L_x \times L_y$. Let us summarize the numerical results which we further elaborate below. Firstly in Section 5.2, we show that the gap in the quasienergy bandstructure closes with increasing disorder. We examine the average bulk localization length, Λ_N as a function of disorder and quasienergy as shown in Fig. 5.3 (a) and show as a function of disorder the quasienergy gap vanishes. Secondly, the point where the gap closes is identified as a topological-to-trivial phase transition. In Section 5.2, we calculate the topological invariant for all states below the resonant quasienergy. The average value of the invariant changes as a function of disorder, as shown in Fig. 5.3 (b). Thirdly, in Section 5.2, the level-spacing statistics indicate that at weak disorder, the qausi-energy bands are extended; however, at strong disorder after the gap closes, all Floquet eigenstates become Anderson localized. This transition to localized states is shown in Fig. 5.4. This result is in line with what is expected from a localization phase transition in the quantum-hall universality class [36, 85].

Results from bulk localization length.

We study the time-evolution of a localized wave-packet under the Hamiltonian defined in Eq. (5.3). The initial wavepacket is chosen to be a δ-function in real space, peaked at position $\mathbf{x}$, and in the 'up' pseudospin, $|\mathbf{x} \uparrow\rangle$. The numerical simulations are done with periodic boundary conditions along both x and y directions. This allows us to probe the bulk Floquet states. The average transmission probability

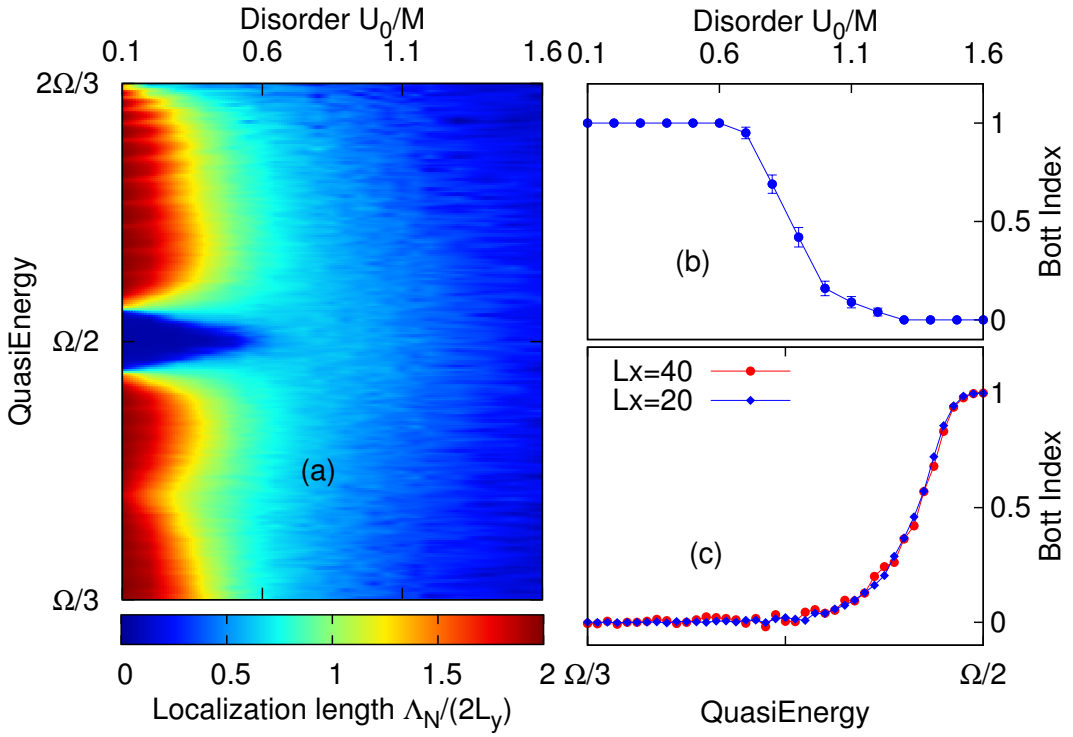

Figure 5.3: (a) Localization length $\Lambda_N/(2L_y)$ as a function of Quasi-energy and disorder strength. This figure shows the gap closing transition at $U_0/M \approx 1$. Simulations were done for system sizes $L_x \times L_y = 400 \times 50$, and evolved for $N = 2500$ time periods. (b) The topological phase transition accompanied by the gap closing. At small disorder the system is topological with a Bott index, 1. As $U_0/M \approx 1$, the gap closes and the system becomes trivial with the index going to 0. (c) Bott index as a function of quasi energy for disorder strength, $U_0/M = 0.6$. The index, $C \approx 1$ near the quasienergy gap at $\epsilon = \Omega/2$ and smoothly goes to zero as a function of quasienergy. We plot for two different system sizes, $L_x = 20, 40$.

along x direction at x', $g_N(x, x', \omega)$, is obtained from Eq. (4.12). We define the bulk localization length, Λ_N, as the inverse participation ratio (IPR) of g, the details of which are discussed in Section 4.2. Fig 5.3 (a) shows $\Lambda_N/(2L_y)$ as a function of quasienergy and disorder. At small disorder ($U_0/M < 0.6$), near the resonance, $\epsilon \sim \Omega/2$, the transmission is vanishing with a localization length, $\Lambda_N \to 0$, indicating the presence of a Floquet band gap. We identify this gap as a 'mobility gap'. In contrast, the eigenstates in the bands, for quasi-energies well away from resonance are extended. It is clear that with increasing disorder strength this gap vanishes. The localization length, $\Lambda_N(\epsilon)$ is also a function of the total time of evolution ($T_{\text{tot}} = NT$), as discussed in section III A. The bulk localization length at a given quasienergy ϵ, appears to be diffusive for short times, $\Lambda_N \sim DN^2$,

where D is the diffusion constant. At long times,the localization length saturates, $\lim_{N\to\infty} \Lambda_N \to \Lambda_{\text{sat}}$, either to the system size or the true localization length at that quasienergy.

Bott index of Floquet bands.

The clean Hamiltonian is topologically non-trivial with a quasienergy band-structure shown in Fig. 5.1 (b). In a cylindrical geometry, there are edge modes in the quasienergy gap at $\epsilon = \Omega/2$. As long as this gap exists, the topological phase remains robust to disorder. This is confirmed by measuring the exact disorder-averaged topological invariant, the Bott index which is shown in Fig 5.3 (b). For weak disorder strength, the average index at the quasienergy $\epsilon = \Omega/2$, is 1, indicating a topological phase. After the gap closes the index smoothly goes to zero. This indicates a transition from a topological to a trivial phase and is expected to be sharp in the thermodynamic limit.

It is expected that in each quasienergy band there exists a single critical quasienergy where the bulk state is delocalized. This extended state carries the bulk topology of the Hamiltonian, analogous to equilibrium systems such as the integer quantum Hall effect. To probe this critical energy, we plot the index as a function of quasienergy in Fig 5.3(c). We see a smooth transition from topological to trivial as a function of quasienergy. This transition as a function of the quasienergy is expected to happen at the critical quasienergy. However, the system sizes we consider are not sufficient to reveal the critical energy in the quasienergy bands.

Level-spacing statistics.

We analyze the level spacing statistics to probe the nature of the localization transition in these driven Hamiltonians. The Floquet Hamiltonian, H_r^F does not possess time-reversal symmetry. Therefore, the quasienergy bands, in the topological phase, has a non-zero Chern invariant. This indicates that the localization-delocalization transition must be of the quantum-Hall universality class. We confirm this by studying the level spacing statistics as a function of quasienergy for different disorder strengths as shown in Fig. 5.4. As discussed in Section 4.3, extended and localized states have different level spacing statistics. At weak disorder [Fig. 5.4 (a)], there exists a band-gap with extended states in both bands. These states have level-spacing statistics identical to the GUE ensemble, P_{GUE} as shown in Fig. 5.4 (d). At $U_0/M \approx 1$, the mobility gap is closed as shown in Fig. 5.4 (b). At much stronger disorder, $U_0/M \approx 2$, we notice that the Floquet bands are completely localized and

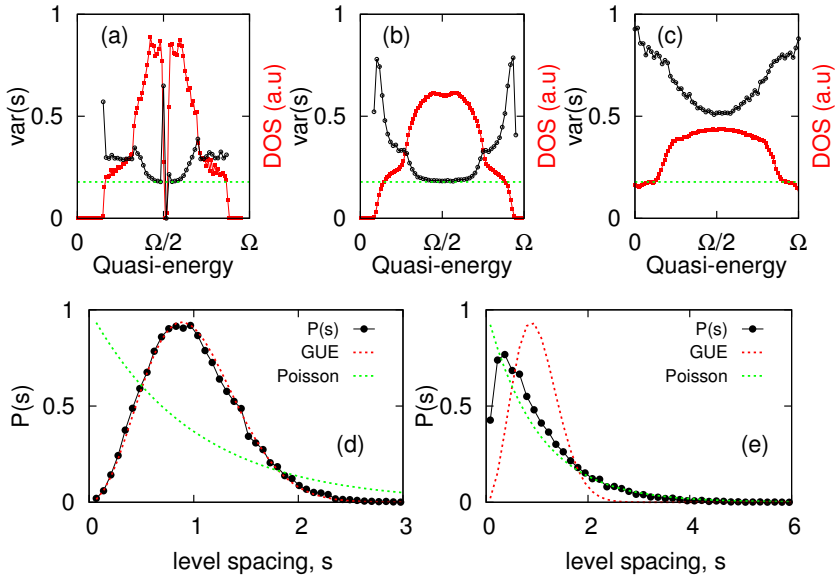

Figure 5.4: Level spacing statistics for the Floquet eigenvalues at different disorder strengths. The extended Floquet states must have level repulsion, with level statistics following the GUE ensemble, in which case, the variance of the level spacing distribution, $\sigma^2(P(s)) = 0.178$. The level spacing $s = \Delta\epsilon/\delta$ is measured in units of average level-spacing, δ, as defined in Section III. Figs. (a), (b), and (c) compare the density of states of the Hamiltonian (in red) with the variance of $P(s)$ (in black) for disorder strengths, $U_0/M = 0.3$, 1, and 2 respectively. Clearly, there are extended states with a band-gap in (a). In (b) the band gap is closed by the extended states, and in (c) all the Floquet eigenstates have localized. (d) shows the level spacing distribution, $P(s)$, at a given quasienergy, $\epsilon/\Omega = 0.43$ and disorder strength $U_0/M = 0.3$. It exactly fits with the GUE distribution. (e) shows $P(s)$ for $\epsilon/\Omega = 0.25$, at disorder strength $U_0/M = 2$. This distribution has better agreement with Poisson statistics, indicating localized states. All the simulations were done for systems sizes $L_x \times L_y = 40 \times 40$.

obey Poisson statistics as shown in Fig. 5.4 (e). This is in agreement with the expectation that as long as the system is topological, with a mobility-gap in the quasienergy spectrum, the system remains robust to localization.

5.3 Conclusions

In conclusion, we have studied the effects of quenched disorder on the quasienergy spectrum of Floquet topological phases in the BHZ model. The Floquet Topological Insulator is robust to disorder, as long as there exists a quasienergy gap in the spectrum. The numerical evidence is in agreement with a localization transition analogous to quantum hall and Chern insulator transitions. This means that the

quasienergy bands must have a delocalized state. Consequently, the topological phase is robust so long as the mobility gap between these two delocalized states is non-vanishing.

Chapter 6

FLOQUET TOPOLOGICAL ANDERSON INSULATOR-I : FLOQUET-HALDANE MODEL

In two-dimensional insulators, it has been shown that in the presence of strong spin-orbit coupling, disorder can induce a phase transition from a trivial to a topological Anderson insulator (TAI) phase, which exhibits quantized conductance at finite disorder strengths. TAIs were predicted in electronic models [33, 67], but have not been observed experimentally.

Can disorder induce topological phases in trivial periodically driven systems? We find concrete examples where disorder induces a topological phase. The model we consideris a graphene-like lattice subject to circularly polarized light, with a staggered potential and on-site disorder. We obtain the phase diagram as a function of disorder strength by calculating the disorder-averaged bulk topological invariant viz., the Bott index. The time evolution of wave packets reveals gapless edge modes in the topological phase. As weexplain below, our model is especially appealing as it is amenable to experimental realization in photonic lattices.

Our starting point is the tight binding Hamiltonian of a honeycomb lattice subject to circularly polarized light,

$$H_r(t) = \sum_{<i\alpha, j\alpha'>} t_1 e^{iA_{ij}} c^\dagger_{i\alpha} c_{j\alpha'} + M\sigma^z_{\alpha\alpha'} c^\dagger_{i\alpha} c_{i\alpha'}, \tag{6.1a}$$

$$H(t) = H_r(t) + V_{\text{dis}}, \tag{6.1b}$$

where $\alpha \in \{1, 2\}$ indicates sublattices A and B, $A_{ij} = \frac{e}{\hbar}\mathbf{A}(t) \cdot (\mathbf{r}_i - \mathbf{r}_j)$ and $\vec{A} = A_0(\sin(\Omega t), \cos(\Omega t))$ is the vector potential for the incident circularly polarized light of frequency Ω. We consider nearest neighbour hopping with magnitude t_1. σ^z is the Pauli matrix, and M is the staggered sublattice potential. $H_r(t)$ represents the clean limit for the system and $H(t)$ is the full Hamiltonian with V_{dis} the disorder potential. The disorder is chosen as an on-site chemical potential, and is diagonal in the real-space representation. We choose the natural system of units $\hbar = e = c = 1$ and set lattice spacing $a = 1$. The bandwidth of the time-independent part of $H_r(t)$ is W. As we explain below, the model of Eq. (6.1) can be directly implemented in the photonic lattice realization considered by Rechtsman et al. [92].

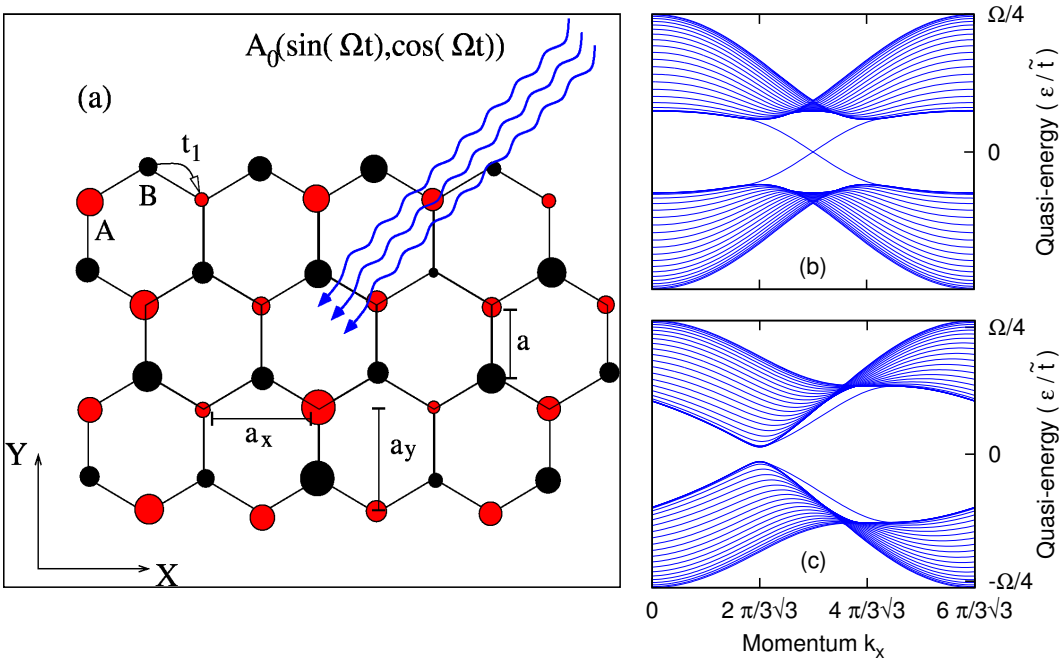

Figure 6.1: (a) Schematic representation of the system indicating uniformly disordered graphene in the presence of a staggered mass potential and a circularly polarized light. Red-Black coloring indicates the staggered mass in the sublattices A and B, and the variable radius the disorder potential. (b) The Floquet band structure for the pure system with parameters, $A_0 = 1.43$, $M = 0$, and $\Omega/\tilde{t} = 12$. The system is topological and supports edge states. The bulk gap is given by the topological mass $\Delta/\tilde{t} \approx 0.75$. (c) A trivial Floquet band structure. All parameters are the same as (b) except $M/\tilde{t} = 0.85$.

The idea behind our construction of a Floquet topological Anderson phase is the following. A honeycomb lattice with a staggered potential , Eq. (6.1), has a gap M at both Dirac cones. A periodic drive alone also induces a gap, with masses of opposite sign at the two Dirac cones. To second order, this gap is simply $\pm A_0^2 v_F^2/\Omega$, for the K and K' points. Thus, the drive induces effectively a Haldane model [35], and yields an example of a Floquet topological phase [53, 84]. For weak and high-frequency ($\Omega \gg t_1$) drives, where perturbation theory is valid, the drive and the staggering compete. Thus, the system is topological when $M < v_F^2 A_0^2/\Omega$, with a Chern number $|C_F| = 1$, and trivial otherwise. The key is the effect of disorder: it diminishes a band gap induced by the drive, but even more strongly it suppresses the staggering. Starting from the trivial phase, $M > v_F^2 A_0^2/\Omega$, an increase in disorder may reverse this balance, and induce a topological phase (for a static analog, see Ref. [117]). In Section 6.3, we provide a Born-approximation analysis of the disorder effects on the two gaps in the static limit.

The explanation above, however, relies on weak, high frequency drive, which effectively produces a static perturbation. It does not capture the scenario in which the topological properties of the time-dependent system are a result of a resonance, connecting states of the original bulk band structure. In addition, we find that it is necessary to consider strong driving in order to observe the disorder induced topological phase. Below, we will establish the existence of the Floquet topological Anderson phase beyond the limit of a weak, high frequency drive. We will consider strong periodic drives, and will analyze two distinct frequency regimes: the high frequency regime ($\Omega > W$), and the low frequency ($\Omega < W$) regime in which resonances occur within the band-structure. We will compare the two regimes and show that both of them exhibit a disorder-induced FTAI phase.

First, let us transform the problem defined in Eq. (6.1) into a time-independent Floquet Hamiltonian,

$$H^F_{nm} = n\Omega\delta_{nm} + \int_0^{2\pi/\Omega} dt e^{i\Omega(n-m)t} H(t). \tag{6.2}$$

The 'Floquet' indices n (and m) refer to replicas of the Hilbert space as discussed in Chapter 3. We set the boundaries of the quasienergy zone at $\pm\Omega/2$. The off-diagonal terms (in Floquet indices) of H^F_{nm} emerge from the hopping term in Eq. (6.1), $(H_r)_{ij} = t_1 \exp(iA_0 \cos(\Omega t + \phi_{ij}))$, where (i, j) indicates hopping from site i to j and $\phi_{ij} = \pm\frac{\pi}{3}$ or 0. Therefore, $\left(H^F_{m,m+n}\right)_{ij} = t_1 i^n J_n(A_0) \exp(i\phi_{ij})$, where $J_n(A_0)$ are the Bessel functions of the first kind. Here, to efficiently use exact-diagonalization, we neglect $H^F_{m,m+n} = 0$ for $n \geq 2$. We also truncate $\left(H^F\right)_{nm}$, such that the Floquet indices obey $|n|, |m| \leq n_{max}$, with n_{max} determined through convergence tests. The typical quasienergy spectrum of our model is given in Figs. 6.1 (b) and (c), where we have defined a renormalized hopping, $\tilde{t} = t_1 J_0(A_0)$.

The quasienergy band structure encodes the topological properties of time-periodic Hamiltonians. While non-interacting equilibrium 2D Hamiltonians with broken time-reversal symmetry are classified by the Chern number, periodically-driven systems require a more general topological invariant — the winding number — which counts the number of edge states at a particular quasienergy [94]. In disordered time-independent systems, the disorder-averaged Chern number is the Bott index, as defined by Hastings and Loring [73]. For the periodically-driven honeycomb lattice model, the disorder-averaged winding number is calculated using the Bott indices obtained from the eigenvalues and eigenvectors of H^F, defined in Eq. (6.2) , and truncated to a finite number of replicas. The Bott index at a particular quasienergy,

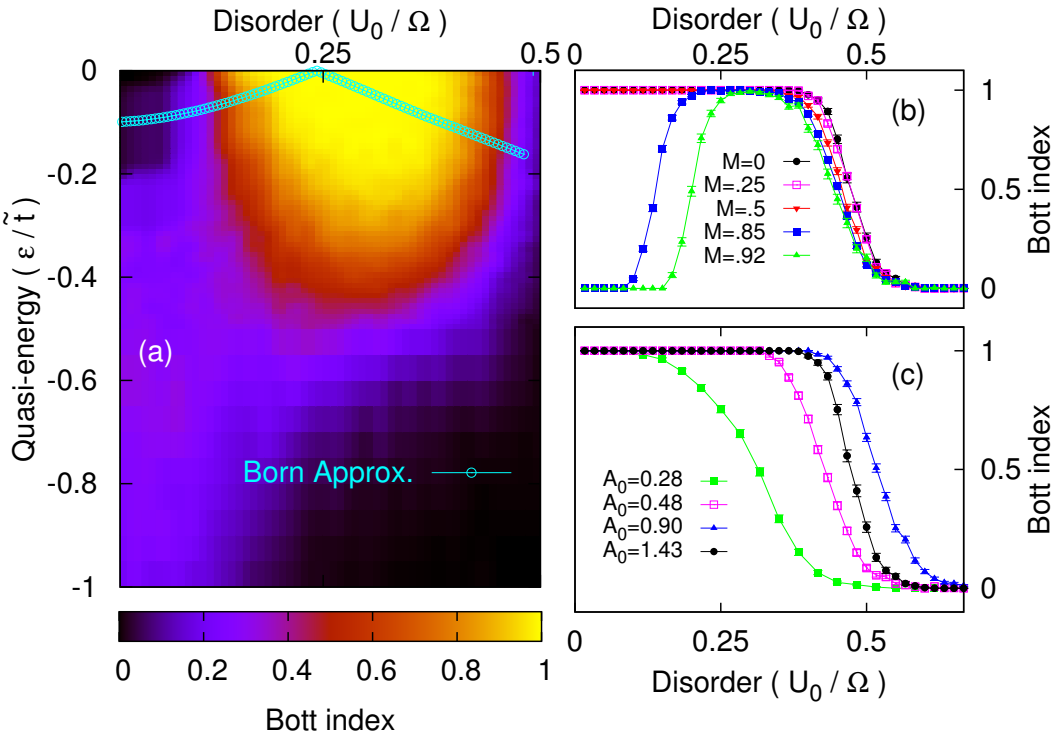

Figure 6.2: (a) The Bott index,C_b, (in color), as a function of the quasienergy and the disorder strength. Edge states are observed in the region where $C_b(0) = 1$. The quasienergy gap, in the Born approximation, is shown (cyan) as a function of disorder. The system parameters are $A_0 = 1.43$, $M/\tilde{t} = 0.85$ and the size is $(L_x, L_y) = (30, 30)$. (b) C_b as a function of disorder for different staggered masses $M/\tilde{t} = 0$, 0.5, 0.85, 1 at quasienergy $\epsilon = 0$ keeping t_1 and A_0 same as (a). (c) C_b as a function of disorder for different driving strengths, $A_0 = 0.28$, 0.48, 0.90, and 1.43, keeping fixed t_1 and $M/t_1 = 0$. We have set $\Omega/t_1 = 12J_0(1.43)$.

$C_b(\epsilon)$, for the truncated H^F, is the number of edge states at that quasienergy [94]. Also, the Chern number of a quasienergy band is simply the difference in the Bott indices at the band edges.

6.1 Case I : Off-resonant radiation

Let us first consider the case of $\Omega > W$ without resonances. The clean system forms a trivial insulator, with its quasienergy spectrum shown in Fig. 6.1 (c). The Bott index, C_b, as a function of disorder strength, U_0, and quasienergy is shown in Fig. 6.2 (a). At very weak disorder, the index, $C_b(\epsilon = 0) = 0$ in the quasienergy gap, and it is not quantized at other quasi-energies, indicating a trivial phase. A topological phase emerges as disorder increases, and is manifested by the Bott index becoming one, $C_b(0) \sim 1$. This phase is induced by both disorder and drive, and therefore we

identify it as a Floquet topological Anderson insulator (FTAI). As expected, varying M while keeping the drive strength fixed, shifts the position of the trivial-topological transition (see Fig. 6.2 (b)). A qualitative description of this transition is provided by the disorder-averaged Born approximation which we elaborate in Section 6.3. Even though, this approximation (Fig. 6.2(a)) captures this basic physics of the transition, it overestimates the exact point of the transition.

At disorder strengths that are considerably larger than the transition point, the FTAI phase is destroyed and there is localization at all quasi-energies. This transition is insensitive to the staggered potential strength, as is evident from Fig. 6.2 (b); however, it depends on the drive strength (see Fig. 6.2 (c)). To observe the FTAI, the trivial-to-topological transition must occur well before the localization transition. Thus we consider the effects of strong driving (where $A_0 \sim 1$). The topological phase is protected against disorder if there is a 'mobility gap' in the spectrum, and some states are delocalized.

Next we numerically examine the existence of edge states as a diagnostic for topological phases. The time-evolution operator for $H(t)$ is obtained in discrete time steps, δt using a split-operator decompositon. The honeycomb lattice [Fig. 6.1 (a)] is considered in a cylindrical geometry, with periodic boundary conditions along X and open ones along Y (see Fig. 6.3 (a)). Initializing with a δ-function wavepacket at $\mathbf{r}_0 \equiv (x_0, y_0)$, the Green function, $G(\mathbf{r}, \mathbf{r}_0, t)$, is obtained from the time-evolution operator, $U(t, 0)$. An evolution for N time periods ($T = 2\pi/\Omega$) yields $G_N(\mathbf{r}, \mathbf{r}_0, NT) = \langle \mathbf{r}|U(t = NT, 0)|\mathbf{r}_0\rangle$. The initial position, $\mathbf{r}_0$, is chosen to probe edge or bulk. Compared to the analysis by exact-diagonalization of H^F, in this method we do not need approximations, and large system sizes are accessible.

The propagator, $G_N(\mathbf{r}, \mathbf{r}_0, NT)$ is the Floquet Green's function obtained from H^F as discussed in Section 4.2. So, the quasienergy eigenvalues and eigenstates are analyzed by Fourier transforming the Green's function in time, $G_N(\mathbf{r}, \mathbf{r}_0, \epsilon)$. With disorder, we calculate, $g_N(\mathbf{r}, \mathbf{r}_0, \epsilon) = \langle |G_N(\mathbf{r}, \mathbf{r}_0, \epsilon)|^2 \rangle$, where $\langle . \rangle$ indicates disorder averaging. The extended or localized nature of the states at quasienergy ϵ is given by the spread of g_N defined as $\lambda_x(N)$, and $\lambda_y(N)$, along X and Y directions respectively.

The time-evolution is carried out for a system with $A_0 = 1.434$, $M/\tilde{t} = 0.85$, $U_0/\tilde{t} = 3.5$, and $\Omega/\tilde{t} = 12$. These parameters correspond to a FTAI and, thus we expect ballistic edge states at $\epsilon = 0$. The initial wavepackets are chosen in the A sublattice, on the two edges (cases (I) and (III)), and the bulk (II), as shown in Fig.

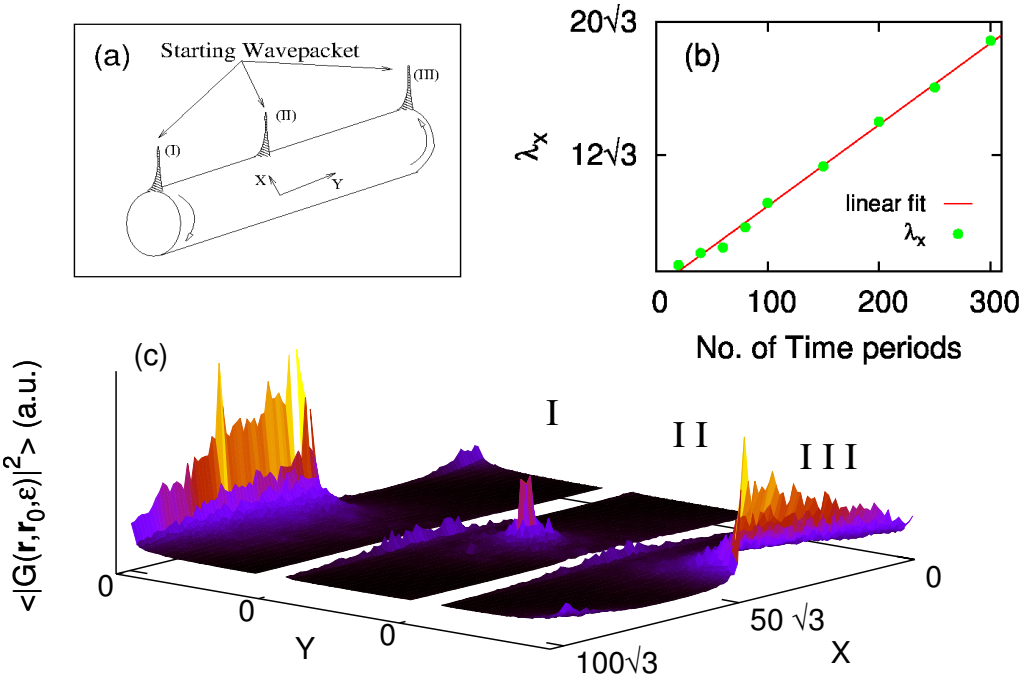

Figure 6.3: (a) The cylindrical geometry for the time evolution of a starting δ-function wavepacket. Cases (I), (II) and (III) have the starting positions, $\mathbf{r}_0 \equiv (x_0, y_0)$ in the A sublattice at the left edge, bulk, and right edge with $y_0/a_y = 0$, $N_y/2 - 1$ and N_y respectively. In all the cases, we fix $x_0/a_x = N_x/2$. (b) The spread of $g_N(\mathbf{r}, \mathbf{r}_0, 0)$ as a function of total time of evolution $T_f = NT$ along the X direction, for $\mathbf{r}_0$ corresponding to case (I). $\lambda_x(N)$ grows linearly, with a velocity $v_{\text{edge}} = (0.09 \pm 0.001)a/T$. (c) $g_N = \langle |G_N(\mathbf{r}, \mathbf{r}_0, \epsilon = 0)|^2 \rangle$ in real space as a function of $\mathbf{r}$, for the three cases, with $N = 300$ and averaged over 400 realizations of disorder . Each sublattice has $N_x \times N_y = 100 \times 30$ points. The system parameters are $A_0 = 1.43$, and $M/\tilde{t} = 0.85$.

6.3 (a). After evolution for N cycles, $g_N(\mathbf{r}, \mathbf{r}_0, 0)$, for all three cases is shown in Fig. 6.3 (c). For cases (I) and (III), g, is extended along X and localized in Y, indicating the presence of an edge state. The decay of g_N along X after some finite distance is due to finite time-evolution. The chiral nature of the edge states are also revealed by the direction in which $g_N(\mathbf{r}, \mathbf{r}_0, \epsilon)$ evolves as a function of N. Fig. 6.3 (b) shows that $\lambda_x(N)$ increases linearly with time of evolution, N, indicating that the edge states are ballistic and do not backscatter from impurities. In contrast, bulk states are diffusive in nature until Anderson localization sets in. A finite amplitude is observed on the edge when starting with a bulk wavepacket because the bulk localization length is larger than the width of the system, indicating an overlap of the edge state wavefunction with the initial wavepacket. We have shown the presence

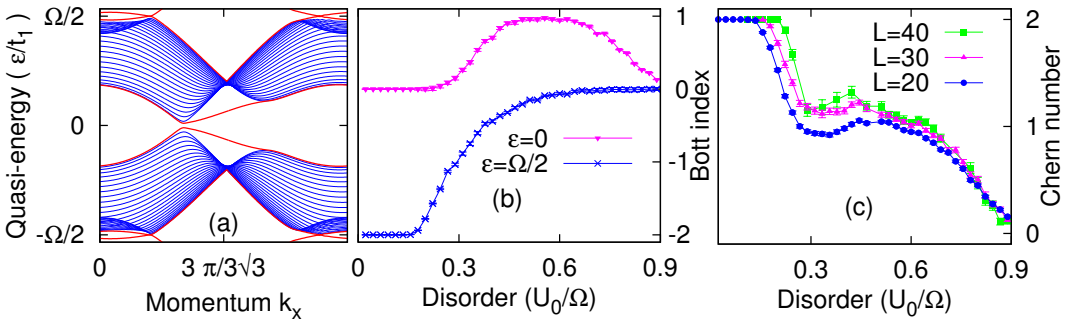

Figure 6.4: (a) Band structure for the case of a single resonance. Edge-states (shown in red) are observed at the two bulk band gaps at quasi-energies $\epsilon/t_1 = 0$ and $\Omega/2$. The gap at $\epsilon = 0$ is made trivial by a staggered mass. The system parameters are $A_0 = 0.75$, $M/t_1 = 0.3$, and $\Omega/t_1 = 9/2$. (b) Disorder-averaged Bott index at a particular quasienergy gap, $C_b(0)$ (magenta) and $C_b(\Omega/2)$ (blue).The Floquet Hamiltonian is truncated after 9 Floquet bands. System size is $(L_x, L_y) = (30, 30)$. (c) Disorder-averaged Chern number, $C_F = C_b(0) - C_b(\Omega/2)$, of a single Floquet band between $\epsilon = -\Omega/2$ and $\epsilon = 0$.

of protected edge states. This confirms the existence of the FTAI.

6.2 Case II : Resonant radiation

This novel phase persists even when there is a resonance within the band structure($\Omega < W$). There, a transition occurs between an FTI phase and the disorder-induced FTAI phase. Furthermore, the FTAI phase in this case cannot be understood using perturbative arguments since the resonance alters the topological nature of all the Floquet bands in the problem as discussed in Chapter 3. Fig. 6.4 (a) shows the quasienergy spectrum of the clean system. The gap at the resonance, $\epsilon = \Omega/2$ is topological with $|C_b(\Omega/2)| = 2$ and, thus, supports two edge states. The gap at the Dirac points is trivial, $|C_b(0)| = 0$, since the staggered mass M still dominates over the effect of the drive near $\epsilon = 0$. Fig. 6.4 (b) shows two transitions as disorder is increased. A topological-to-trivial transition removes the edge states in the gap at the resonance ($\epsilon = \pm\Omega/2$). Another transition induces topological edge states at $\epsilon = 0$. From the finite sizes investigated, the topological to trivial transition at $\epsilon = \Omega/2$ happens initially and is unrelated to the transition at $\epsilon = 0$. Finally, disorder becomes strong enough to localize the entire band, as in the high-frequency case. The Chern number of the band between these two quasi-energies, $C_F = C_b(0) - C_b(\Omega/2)$ changes from $|C_F| = 2$ to $|C_F| = 1$, and then to $|C_F| = 0$ (Fig. 6.4 (c)). The intermediate regime, with $|C_F| = 1$, is again identified as a FTAI — it is a topological state that requires both disorder and a periodic drive. The fact that this phase exists even in a system

which is non-perturbatively affected by the periodic drive indicates the universality and robustness of the FTAI.

6.3 Born approximation in the honeycomb lattice

The transition from a trivial state to a topological state is due to renormalization of parameters of the Hamiltonian due to disorder. We calculate the correction to the density of states are obtained from exact analytical expressions for the self energy. This provides an accurate description for the density of states as a function of disorder at dilute disorder. We adapt the calculation of the Self-energy to the honeycomb lattice. The disorder averaged Floquet Green function is given by,

$$\overline{G^F(\epsilon, \mathbf{k})} = \frac{1}{\epsilon - H^F(\mathbf{k}) - \Sigma(\epsilon)}, \tag{6.3}$$

and

$$\Sigma(\epsilon, \mathbf{k}) = \int_{\mathrm{FBZ}} d\mathbf{k}' \ \langle V_{\mathrm{dis}}(\mathbf{k}, \mathbf{k}') G^F(\epsilon, \mathbf{k}') V_{\mathrm{dis}}(\mathbf{k}', \mathbf{k}) \rangle, \tag{6.4}$$

where $\langle \dots \rangle$ denotes disorder averaging, $V_{\mathrm{dis}}(\mathbf{k}, \mathbf{k}')$ is the disorder potential in Fourier space, and Σ is the self energy. We are interested at the physics of the topological transition near $\epsilon = 0$ as a function of disorder. For the case of zero resonances, this is correctly modeled by the effective Hamiltonian, H_{eff}, defined in Eq. (3.20),

$$H_{\mathrm{eff}} \quad = \quad v(k_x \sigma_x \tau_z + k_y \sigma_y) + M\sigma_z + \Delta \sigma_z \tau_z, \tag{6.5}$$

where σ denotes the sublattice degree of freedom, and τ denotes the valley (K or K') degree of freedom. We have written the low-energy form of the effective Floquet Hamiltonian by linearizing around the Dirac points. Therefore, instead of using the Floquet Green function, G^F, we use the effective Green function given by,

$$G_0^{\mathrm{eff}}(\epsilon, \mathbf{k}) = \frac{1}{\epsilon - H_{\mathrm{eff}}(\mathbf{k})}. \tag{6.6}$$

The disorder potential, V_{dis}, is modeled as δ-correlated point scatterers. The short range of scattering implies that both inter- and intra-valley processes must be taken into account. It is assumed that, in the linearized regime, the disorder matrix in real space is [101],

$$V_{\mathrm{dis}}(\vec{r}) = \sum_i \begin{pmatrix} U_i^A & 0 & U_i^A e^{i\phi_i^A} & 0 \\ 0 & U_i^B & 0 & U_i^B e^{i\phi_i^B} \\ U_i^A e^{-i\phi_i^A} & 0 & U_i^A & 0 \\ 0 & U_i^B e^{-i\phi_i^B} & 0 & U_i^B \end{pmatrix} \tag{6.7}$$

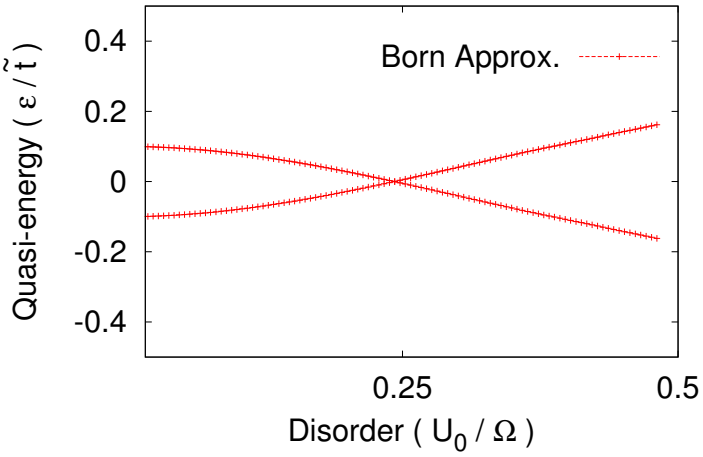

Figure 6.5: The expected quasienergy gap as a function of disorder given by the Born approximation. This is obtained by plotting the solution to the $\tilde{\omega} = \tilde{M} - \tilde{\Delta}_0$ as a function of disorder. The parameters for the system are $A_0 = 1.434$, $\Delta_0 = 0.75$ and $M = 0.85$.

where

$$U_i^{A,B} = u_i^{A,B}\delta(\mathbf{r} - \mathbf{r}_i^{A,B}), \tag{6.8}$$

$$\phi_i^{A,B} = (\mathbf{K'} - \mathbf{K}) \cdot \mathbf{r}_i^{A,B}. \tag{6.9}$$

A and B refer to the different sub-lattices, **K** and **K'** are the two valleys, and i is summed over the unit cells. The disorder potentials $u_i^{A,B}$ are taken from an uniform distribution in the range $[-U_0/2, U_0/2]$ and are δ-correlated. Therefore,

$$\langle u_i^A \rangle = \langle u_i^B \rangle = 0, \tag{6.10}$$

$$\langle u_i^\nu u_j^{\nu'} \rangle = \frac{U_0^2}{12}\delta_{ij}\delta_{\nu\nu'}, \quad \nu, \nu' \equiv A, B, \tag{6.11}$$

where we have used that the variance of the uniform distribution is $U_0^2/12$. The diagonal and off-diagonal terms in Eq. (6.7) account for intra- and inter-valley scattering respectively and are assumed to have the same magnitude.

The self energy can be calculated by rewriting V_{dis} (see Eq. (6.7)) in Fourier space and using Eq. (6.4) . In the limit of $|\mathbf{k}'| \ll |\mathbf{K} - \mathbf{K'}|$, it can be assumed that, the fast oscillating exponents in the off-diagonal terms in the self energy Eq. (6.4) averages to zero [101], i.e.,

$$\langle \sum_i e^{i(\mathbf{k}'.r_i^\nu \pm \phi_i^\nu)} \rangle = 0. \tag{6.12}$$

Therefore, the self energy is diagonal in valley space and independent of momentum $\mathbf{k}$. Consequently, after integrating out the momentum, $\mathbf{k}'$, in the first Brillouin zone, the four main contribution to the self energy are,

$$\Sigma = \Sigma_I \mathbb{I} + \Sigma_M \sigma_z + \Sigma_\Delta \sigma_z \tau_z + \Sigma_0 \tau_z, \tag{6.13}$$

with

$$\Sigma_I = -nu^2 \frac{i\omega_n}{4\pi v_F^2} \log\left(\frac{v_F^4 D^4}{f_+ f_-}\right), \tag{6.14}$$

$$\Sigma_M = -\frac{nu^2}{4\pi v_F^2}\left[M \log\left(\frac{v_F^4 D^4}{f_+ f_-}\right) + \Delta \log\left(\frac{f_-}{f_+}\right)\right], \tag{6.15}$$

$$\Sigma_\Delta = \Sigma_0 = 0, \tag{6.16}$$

where $f_\pm = \omega_n^2 + (M \pm \Delta_0)^2$. Therefore, the parameters in $H_{\text{eff}}(t)$ get renormalized as

$$i\tilde{\omega}_n = i\omega_n - \Sigma_0^I, \tag{6.17}$$

$$\tilde{M} = M + \Sigma_0^z, \tag{6.18}$$

$$\text{and,} \quad \tilde{\Delta}_0 = \Delta_0. \tag{6.19}$$

The renormalized mass, $\tilde{M}$, reduces with increasing disorder. The renormalized quasienergy is obtained by analytical continuation of $\epsilon \to \omega$ and the band gap as a function of disorder is the solution to the equation $\tilde{\omega} = \tilde{M} - \tilde{\Delta}_0$. This is shown in Fig. (6.5) with parameters $v_f = 3/2$, $\Delta = 0.75$ $M = 0.85$ and $D = 4\pi/3$. These parameters correspond to the case (I) of zero resonances. The topological phase transition occurs at the point where the band gap vanishes, which happens when $\tilde{M} = \tilde{\Delta}$. For stronger disorder, the gap reopens in the topological phase and a non-vanishing Chern number must therefore be measured at the quasi- energies in the gap.

6.4 Experimental realization in Photonic lattices

This FTAI phase is directly amenable to experimental observation. Recently, a topological band-structure was experimentally demonstrated [92] in a structure composed of an array of coupled waveguides (a "photonic lattice"). We described the setup in Section 3.5. The diffraction of light in this lattice is governed by the Paraxial Schrödinger equation. The waveguides are fabricated in a helical fashion to induce a topological phase, a photonic Floquet topological insulator, with topologically-protected edge states.

The same system may give a realization of Eq. (6.1) and the proposed FTAI phase. The gauge field, A_0, in the photonic system is determined by the helix radius and period. The sublattice potential, M, and on-site disorder, U_0, may be implemented by fabricating waveguides of different refractive indices, which is straightforwardly done in the laser-writing fabrication process [103]. Since each waveguide can be fabricated with a specified refractive index, the mass, M and disorder strength, U_0 can be tuned entirely independently. In the following, we fully discuss the relevant experimental parameters in the photonic lattice setup and demonstrate that this phase is entirely amenable to experiment. The topological transition may be probed by measuring transmission through the photonic lattice for samples of different disorder strengths. For small disorder, the presence of a bulk band gap will give rise to zero transmission through the sample. For disorder strengths above the transition, the presence of edge states in the band gap will allow transmission through the sample: a direct experimental observable.

In order to fully examine the realizability of the experimental setup, we calculate - using standard numerical techniques [48] - that the hopping parameter can be tuned over an extremely large range ($0.083cm^{-1}$ through $2.7cm^{-1}$) because the nature of the coupling between adjacent waveguides is evanescent (these values correspond to the waveguides discussed in Ref. [92], at lattice spacings $30\mu m$ and $12\mu m$, respectively). Furthermore, the on-site energies may be varied significantly by varying the refractive index difference of the waveguides relative to the background (which can be realistically varied in the range of 5.0×10^{-4} through 1.1×10^{-3} - as discussed above). Assuming a waveguide helix pitch of $1cm$ as in Ref. [92], the parameter U_0/Ω may vary over a range of $\sim \pm 1.8$ - this incorporates the full range of parameters discussed in this chapter. For a typical hopping parameter of $t_1 = 1.5cm^{-1}$, the dimensionless parameter U_0/t (the degree of on-site disorder in units of the hopping) can take on values anywhere from $U_0/t = 0$ through 1.6 - again, this includes the range discussed in this chapter.

It is important to demonstrate that the strengths of the gauge field, A_0, as used here are directly realizable under experimental conditions. As shown in Ref. [92], the dimensionless expression for the strength of the gauge field is $A_0 = kR\Omega a$, where k is the wavenumber in the ambient medium ($k = 2\pi n_0/\lambda$, where $n_0 = 1.45$ is the refractive index of fused silica, and $\lambda = 0.633\mu m$ is the wavelength of laser light used); R is the radius of the waveguide helices; $\Omega = 2\pi/1cm$ is the spatial frequency of the helices, and $a = 15\mu m$ is the lattice spacing between nearest neighbor

waveguides. In the experimental work [92], the helix radius was tuned (with a constant helix pitch of $1cm$) from $0\mu m$ through $16\mu m$. This corresponds to a gauge field strength (in the dimensionless units of the presented work) of $A_0 = 0$ through $A_0 = 2.17$. The experimental work showed that this range was fully accessible experimentally. We perform numerical calculations at a number of different gauge field strengths, including 0.28, 0.48, 0.9 and 1.43 (for the calculations shown in Fig. 6.2); 1.43 (for the calculations in Fig. 6.3); and 0.75 (for the calculations in Fig. 6.4). All of these are clearly experimentally accessible.

Taken together, we have shown here that the parameters proposed in this work are directly amenable to experimental realization. Therefore, the FTAI phase may be implemented using an optical wavefunction in a photonic crystal structure, as opposed to an electronic wavefunction in a condensed matter system.

6.5 Conclusions

We have established the existence of a disorder-induced Floquet Topological Insulator phase. Starting from a clean system that is trivial even in the presence of time-periodic driving, disorder renormalizes the parameters of the Hamiltonian to make they system topological. We show the universality of the phase by also realizing the phase when the radiation is not perturbative, and induces a resonance in the bandstructure. Experimentally the parameters are in a range that can be achieved in a photonic lattice, and this could be a first experimental realization of the Topological Anderson Insulators.

Chapter 7

FLOQUET TOPOLOGICAL ANDERSON INSULATOR-II : FLOQUET-BHZ MODEL

We showed the existence of disorder induced topological phase in periodically driven honeycomb lattice models [109]. These are labeled as the Floquet Topological Anderson Insulator (FTAI). The FTAI phase is unique because it requires both the drive and disorder to be topologically non-trivial. The honeycomb lattice model, driven with a circularly polarized light [53, 84] is equivalent to the Haldane model for anomalous quantum Hall effect[35]. In the driven model in the honeycomb lattice, disorder renormalizes the effective static mass gaps at the Dirac point. The disorder renormalizes the gaps in such a way as to induce a topological phase.

Now, we generalize the FTAI phase to the Floquet-BHZ model. We start with the driven BHZ model described in Eq. (5.1). As discussed in Chapter 5, disorder renormalizes the radiation potential, $\mathbf{V} \equiv (V_x, V_y, V_z)$. In the following, we present our claim for realizing FTAI in the driven quantum well systems, and numerical evidence for realizing such a phase. In Section 7.1 we first consider the case of a rotating Zeeman field. The FTAI in the quantum wells exists in the presence of time-reversal symmetry, in contrast to the honeycomb lattice models. Then in Section 7.2 we show the existence of a disorder-induced Chern insulator phase in a BHZ model incident with elliptically polarized radiation.

7.1 FATI in rotating Zeeman fields

Let us consider the case of generalized Zeeman field, with the components, $V_{x,y,z}$ are constants independent of momentum, $\mathbf{k}$. The clean driven phase must be topologically trivial. We have the Hamiltonian in Eq. (5.1) and restrict ourselves to the case with a single resonance, $M < \Omega < W$. Choosing V (see below for the choice of V) so that the Hamiltonian is trivial, we add on-site uniformly random disorder to the chemical potential. In the following, we show that at finite disorder strength the Floquet topological Anderson insulator is obtained.

The phase of the driven model is always trivial for a large enough V_x or V_y. This is in contrast to the topological phase induced when $\mathbf{V} = (0, 0, V_z)$. In Chapter 5, we discussed the effects of disorder when $\mathbf{V}$ is along z direction. As discussed in

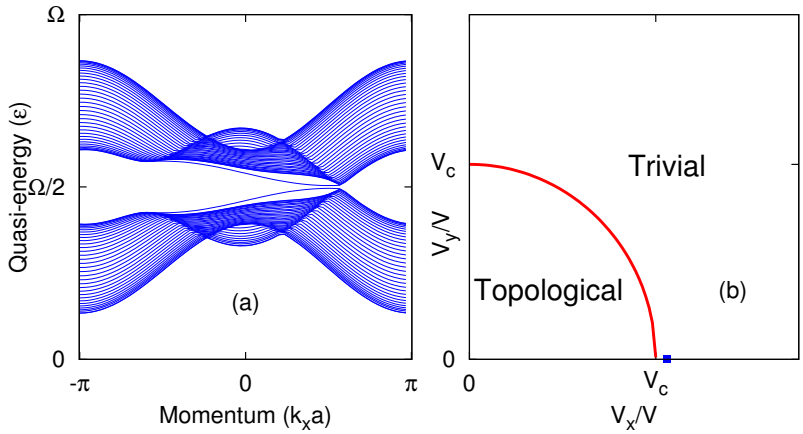

Figure 7.1: (a) Bandstructure of the driven system for $V_z/M = 2$, $V_x/V_z = 0.15$ in the trivial phase. The other parameters of the Hamiltonian is same as Fig. 5.1. (b) shows the typical phase diagram for the Floquet topological phase as a function of V_x and V_y. For $V_{x,y} < V_c$, the phase is topological and otherwise trivial. The clean system phase for obtaining the FTAI phase is chosen such that $V_x > V_c$, with $V_y = 0$. The initial point of the trivial driven system is schematically represented as the point (blue square) in this diagram.

Section 3.3, the quasienergy gap at resonance ($\epsilon = \Omega/2$), is topological as long as the map defined by the vector $\hat{n}$ [see eq. (3.29)] has a non-trivial Chern number. This condition is satisfied for,

$$\frac{V_{x,y}}{V} < V_c, \tag{7.1}$$

where $V_c = |\sqrt{V_x^2 + V_y^2}|$ is such that $\exists\, \tilde{\mathbf{k}}$ in the Brilluoin zone, for which $|\mathbf{V}_\perp(\tilde{\mathbf{k}})| = 0$. Intuitively, $|\mathbf{V}_\perp|$ [defined in Eq.(3.27)] is the magnitude of the gap that opens at resonance, $\epsilon = \Omega/2$, and therefore, at the critical condition, V_x or $V_y = V_c$, this gap closes. The schematic phase diagram for the topological phase in the presence of a radiation field, $\mathbf{V}$, as a function of V_x and V_y is shown in Fig. 7.1 (b).

Now consider the case where we choose the radiation potential, $V = (V_x, 0, V_z)$, such that it lies in the trivial phase.For example, Fig. 7.1 (a) shows the band-structure with $V_x/V_z = 0.15$ and $V_y = 0$, in a cylindrical geometry. The bulk bands are gapped with no edge states crossing the gap, and this clearly indicates a trivial phase. As a function of the disorder strength, there are several competing effects: (i) Disorder renormalizes the radiation field components V_x, V_y and V_z, (ii) Disorder renormalizes the parameters of the bare undriven Hamiltonian, and (iii) Strong disorder localizes the bands as shown in section IV. The disorder induced topological phase is driven by the effect (i), and is destroyed by effect (iii). The renormalization due to disorder

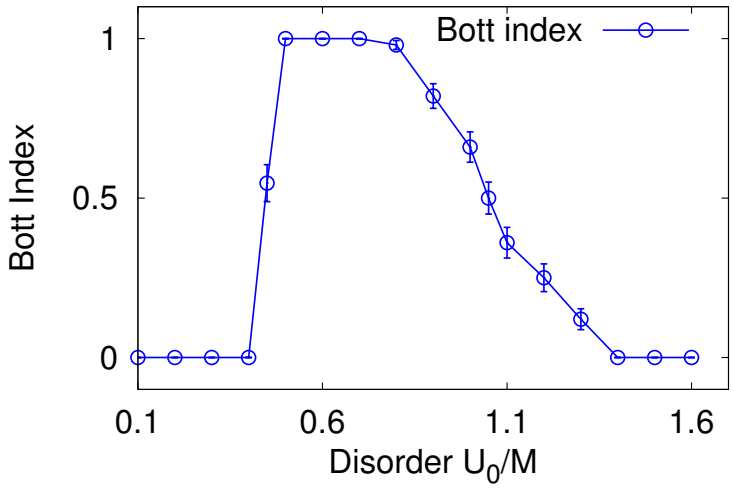

Figure 7.2: Bott index, as a function of disorder strength U_0/M for the quasienergy at $\Omega/2$. The clean system starts of as trivial, and as shown at finite disorder strength, the Hamiltonian acquires a non-zero average Bott index indicating the presence of a topological phase. The system considered in this plot was $L_x \times L_y = 40 \times 40$.

on V_x is such that for sufficiently strong disorder, a topological phase is induced. It is essential to choose the parameters close to the phase transition. This is because, for a large enough, $V_x \gg V_c$, the bands localize before a topological phase is induced.

Numerical Results

We examine, numerically, the Bott index in the quasienergy gap as a function of disorder. The parameters of the time-independent part of the Hamiltonian are, $A/M = 0.2$,$B/M = -0.2$. The parameters of the radiation potential is chosen to be in the trivial phase, with $V_x/V_z = 0.15$ and $V_y/V_z = 0$, and $V_z/M = 2$ with the frequency of the drive, $\Omega/M = 1$. The 'particle-hole' symmetry around the resonance, $\epsilon = \Omega/2$, ensures that the trivial-to-topological transition must occur at the resonance quasienergy. Fig. 7.2 shows the Bott index, $C_b(\epsilon = \Omega/2)$ as a function of the disorder strength. At small disorders, the index is 0 indicating a trivial phase. At intermediate disorder strength, the index $C_b \sim 1$ implying that a topological phase is induced at this disorder strength. Strong disorder leads to localization of all Floquet eigenstates which is again topologically trivial indicated by $C_b \to 0$. The topological nature of the induced phase may also be detected from the emergence of non-trivial edge states. In the FTAI phase, this can be verified by an exact time-evolution of wave-packets on the edge as discussed in section

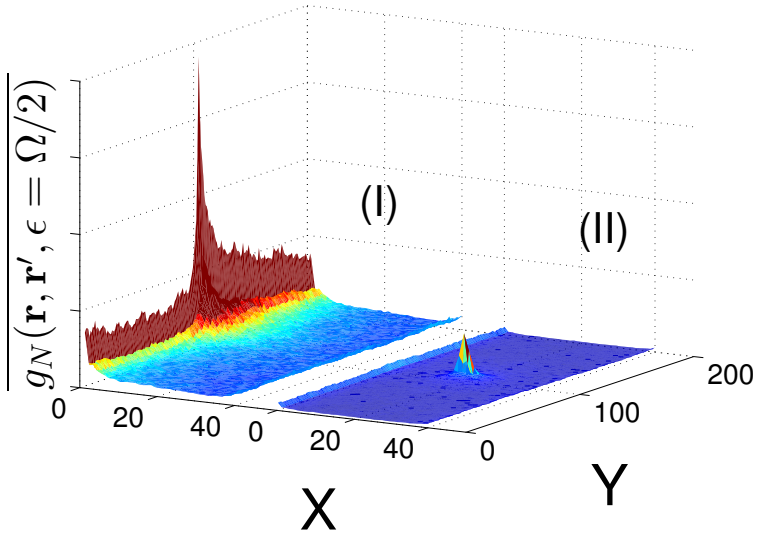

Figure 7.3: The time-evolution of a δ-function wavepacket for disorder strength $U_0/M = 0.7$. Figures (I) and (II) show $\overline{g_N(\epsilon = \Omega/2, \mathbf{r}, \mathbf{r}')}$ for different choice of initial position $\mathbf{r}$. (I) shows the presence of an extended edge mode at quasienergy, $\epsilon = \Omega/2$. (II) on the other hand, shows that choosing the starting wave-packet in the bulk, continues to remain localized in the bulk. All simulations were carried out on a lattice of size $L_x \times L_y = 40 \times 200$ and for a total number of time periods, $N = 5000$.

4.2. In Fig. 7.3, we obtain the average transmission probability (see Eq. 4.12) at quasienergy, $\epsilon = \Omega/2$, for disorder strength $U_0/M = 0.7$. For the clean system, this quasienergy corresponds to the trivial-gap in the spectrum and has no bulk or edge states. In the disordered system, Case I in Fig 7.3 shows that there exists extended states on the edge, which was obtained when the initial wave-packet was chosen on the edge. On the other hand, case II shows that choosing the initial wavepacket in the bulk keeps the state localized around the initial state. This confirms that the state observed is indeed a topological state.

7.2 Realizing the FTAI using elliptically polarized light

In this section, we outline a proposal for realizing the Floquet topological Anderson Insulator phase by irradiating semiconductor quantum wells using elliptically polarized light. In the preceding section, we introduced the FTAI phase using an idealized model of a generalized Zeeman field. We show that using elliptic polarization, it is possible to induce a topological phase at finite disorder. Experimentally, it is easier to tune the polarization of light than controlling the impurity concentration.

We show that it is possible to detect the presence of the FTAI phase by tuning the polarization of light on a disordered sample.

It has been shown [69] that circularly polarized light induces a Chern insulator, with broken time-reversal symmetry, with a Chern number, $C = 2$. On changing the ellipticity of the incident light, it is possible to tune the driven phase from a topological to a trivial phase. Since we are irradiating with elliptically polarized light, this model breaks time-reversal symmetry explicitly. This provides an ideal starting point to realize an analogous FTAI phase with broken time-reversal symmetry. By choosing a polarization where the incident light induces a trivial phase, the FTAI phase would be obtained by adding disorder. As discussed in Section V, the disorder renormalizes the various components of the drive,. This corresponds to renormalizing the ellipticity of the radiation, thereby inducing a topological phase at finite disorder strength which is the FTAI phase.

An elliptically polarized light is introduced into the quantum well model, H_0 [see Eq. (5.1)] through a time-varying gauge field, $\Big(A_x \sin(\Omega t), A_y \cos(\Omega t)\Big)$. The magnitude of A_x and A_y determine the ellipticity of the light. In the following, we always choose the magnitude of $|\mathbf{A}| = \sqrt{A_x^2 + A_y^2} = 1$, and the ellipticity is determined by $\theta = \arctan(A_y/A_x)$. In the perturbative regime, the Hamiltonian can be written in a generalized form analogous to that defined in Eq. (5.1). In fact, the unit vector, $\hat{n}$ defined in Eq. (3.29) wraps around the sphere twice resulting in a topological phase with Chern number, $C = 2$. The details of the derivation of the quasienergy gap and winding for this model are provided in the Section 3.4.

We numerically compute the Bott index from the Floquet spectrum of this model. The undriven system is chosen with the following parameters, $A/M = 1$, $B/M = -0.2$, and the driving frequency is $\Omega/M = 3.1$. The time-dependent gauge field is also chosen such that, $|A|/M = 1$ with varying θ. The topological nature of the Floquet bands is determined by the angle θ. Fig.7.4 (a) shows the Bott index as a function of θ. The Chern number of the band of the clean system is shown in red. Clearly, the clean system is trivial for $\theta = 0.1\pi/4$. We choose this angle as the starting point for obtaining the FTAI. As shown in Fig 7.4 (b), at finite disorder, for this polarization angle, $\theta = 0.1\pi/4$, a topological phase is induced, which we identify as the FTAI. Fig 7.4 (a) also shows the dependence of the disorder averaged Bott index at a disorder strength, $U_0/M = 1$ on the angle θ. A consequence of a disorder induced topological phase is that a larger fraction of the polarization angles, θ, are topological. Therefore, the existence of this phase may be detected experimentally

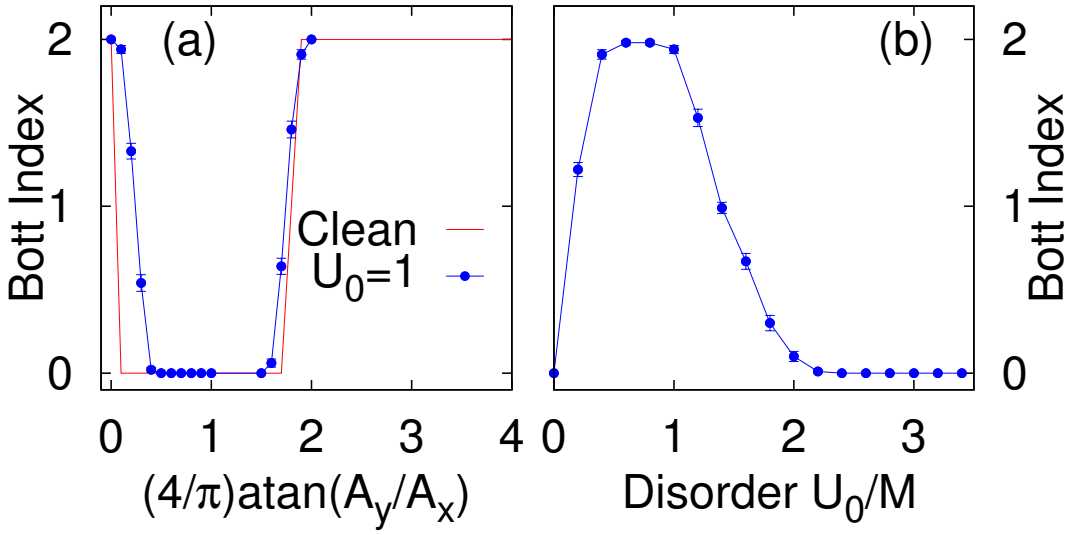

Figure 7.4: (a) Comparison of the Bott index for as a function of the polarization angle, θ for the clean sample and disorder strength, $U_0/M = 1$. Clearly, the region where the system is topological is larger in case of the disordered system, indicating the presence of a disorder-induced topological phase. (b) Bott index as a function of disorder strength when the initial polarization is $\theta = 0.1\frac{\pi}{4}$. A topological phase, with $C = 2$, is induced as a function of disorder. The simulations were run for system sizes, $L_x \times L_y = 20 \times 20$.

by comparing a disordered and clean sample by tuning the polarization of incident light.

In this section, the model we consider has explicitly broken time-reversal symmetry while candidate materials for the realization of this phenomenon are time-reversal symmetric. We have obtained a disorder induced Chern insulator phase from Floquet spectrum of the 2×2 upper-block of the full BHZ model, defined as $H_0(\mathbf{k})$ in Eq. (5.1). One possible way to experimentally observe this induced topological phase is to isolate the bands of each block using a Zeeman coupling to a constant magnetic field. The behavior of the full 4×4 BHZ model in the presence of elliptically polarized light and disorder is subtle. Let us define the Chern numbers for the upper and lower blocks of the BHZ model as C_u and C_l, respectively. The lower block is the time-reversed counterpart of $H_0(\mathbf{k})$, $H_0^*(-\mathbf{k})$. It has a Chern number, $C_l = -2$ when the polarization angle, $0 < \theta < \frac{\pi}{2}$. As a result, when we consider the clean system, at $\theta = 0.1\frac{\pi}{4}$, the bands of the full BHZ Hamiltonian are topological with a Chern number $C = C_l + C_u = -2$. Now, when a FTAI phase with $C_u = 2$ is induced at finite disorder in the upper block, for $\theta = 0.1\pi/4$, the lower block is still robust, and has a Chern number, $C_l = -2 = -C_u$. This means that in the quasienergy gap, there

exists counterpropagating edge modes. There is no symmetry to prevent scattering between these counterpropagating states. So, an infinitesimal coupling between the two sets of counterpropagating edge modes is going to gap them out. Therefore, the system with the upper-band FTAI phase is actually a trivial insulator. The induced topological phase in the upper block manifests as a topological to trivial transition for the full BHZ model.

7.3 Conclusions

The driven quantum well systems are also host to disorder induced topological phase. The FTAI requires the presence of both periodic driving and disorder to be topological. The clean driven system is topologically trivial and disorder is introduced to induce a topological phase. As discussed in this chapter, the parameters of the drive are chosen to induce a trivial quasienergy gap. This may be done using appropriate Zeeman fields or a elliptically polarized radiation. Disorder added to this system renormalizes these parameters of the drive. For sufficiently strong disorder, a topological phase is obtained. This is the FTAI phase. At much stronger disorder, the mobility gap vanishes, and all states localize to the trivial Anderson insulator.

Chapter 8

DISORDER IN ANOMALOUS FLOQUET PHASES : THE ANOMALOUS FLOQUET ANDERSON INSULATOR

A two-dimensional driven system can support chiral edge states even if all of its bulk Floquet bands have zero Chern numbers [52, 94]. These are dubbed the Anomalous Floquet topological phases, and we disucss some of its properties in Section 3.5. This situation stands in sharp contrast with that of static two-dimensional systems, where the existence of chiral edge states is intimately tied to the topological structure of the system's bulk bands, as captured by their Chern numbers [107]. A system exhibiting this anomalous behavior was recently realized using microwave photonic networks [27, 39].

In this work, we show that this unique behavior has far-reaching consequences when we consider the effects of disorder on a periodically-driven, topological system with zero Chern numbers. Primarily, we claim that, in two dimensions, robust chiral edge states may coexist with an entirely localized bulk. Bloch bands with non-zero Chern numbers cannot be spanned by a complete basis of localized Wannier functions [104, 106], and therefore they cannot be fully localized by disorder [36]. This follows from the notion that a finite bandwidth of chiral edge states cannot "terminate" without hybridizing with a delocalized bulk state. In contrast, the edge states in a periodically-driven system could wrap around the entire quasienergy zone without terminating at a delocalized bulk state (quasienergy is periodic in the drive frequency). Disorder may then localize the bulk bands which carry zero Chern numbers, without hindering the chiral edge states. In such a system, which we term an anomalous Floquet-Anderson insulator (AFAI), the chiral edge states form a uni-directional one dimensional system, whose dynamics is decoupled from the bulk at all quasienergies. Furthermore, the AFAI phase defies the standard intuition from strictly one-dimensional systems that must have an equal number of right and left moving modes.

The AFAI phase possesses an intriguing new *non-equilbrium* topological transport phenomenon: quantized charge pumping in a non-adiabatic setting. Essentially, if all the states in the vicinity of the edge are occupied by fermions (to a distance of several times the bulk localization length), the uni-directional edge states carry a

current whose long-time average is quantized in units of one particle per driving period. Contrary to Thouless' adiabatic quantized pumping in one-dimension [105], the AFAI pumping quantization does not require a small driving frequency. Here, quantization is guaranteed by two effects: First, the two counter-propagating edge modes carrying the current are *spatially separated* and cannot backscatter into each other even if the driving frequency is not small. Second, the bulk bands are localized. Indeed, the disorder is essential for current quantization: in the absence of disorder, there is no quantization due to the presence of delocalized bulk states. Below we demonstrate and explore the AFAI phase both generally and through an explicit model, and establish its quantized charge pumping property.

8.1 Physical picture and summary of the main results

To begin, in this section we summarize the main results of this work. In particular, we describe the unique spectral characteristics of the AFAI, and the novel non-adiabatic quantized pumping phenomenon that it hosts. Our aim in this section is to provide a heuristic-level picture of our findings; details and further discussion follow in sections 8.3 - 8.5.

In two spatial dimensions, disordered, periodically driven systems may exhibit a variety of phases. Some of these phases have direct analogies in non-driven systems. In cases where such analogies exist, all features of the driven system can be derived from an associated time-independent "effective Hamiltonian" H_{eff}, defined such that $U(T) = e^{-iTH_{\text{eff}}}$. Topological characteristics, such as the presence or absence of chiral edge states at sample boundaries, are in particular captured in those cases by the effective Hamiltonian and its associated Chern numbers, just as for non-driven systems (recall that Chern numbers provide a full topological characterization of non-interacting static systems without symmetries). As a result, many phenomena exhibited by static systems can be mimicked by periodically driven systems; examples include the direct correspondence between chiral edge states and bulk Chern numbers described above, as well as disorder-induced topological transitions, as exhibited by the "topological Anderson insulator" [67] and its Floquet counterpart [109].

The AFAI phase introduced here is a phase of a disordered periodically driven systems whose characteristics are qualitatively distinct from those achievable in the absence of driving. Its defining property is that *all* its bulk Floquet states are Anderson localized by the disorder; nevertheless, its edges support chiral edge

states. This unusual situation has a number of intriguing physical consequences, as we describe below.

In the absence of driving, chiral edge states *must* be accompanied by delocalized states in the bulk of the system. This can be seen by considering a system in an annular geometry and tracking how its spectrum evolves as magnetic flux is threaded through the hole of the annulus. Once a full flux quantum is inserted, the Hamiltonian is equivalent to the original one and therefore its spectrum must be unchanged compared to the original one. Tracing the evolution of a given state as the flux is inserted, there are two options once a full flux quantum is reached: (1) the state returns to its original energy; (2) the state "flows" to a new energy. The edge states evolve according to option (2). The only way for this spectral flow to terminate is if a delocalized bulk state is reached, connecting the upward and downward flowing families of states on opposite edges. Thus we see that chiral edge states cannot exist without delocalized bulk states, as otherwise the spectral flow would have to continue up and down to infinite energies.

The above argument fails when considering a periodically driven system, where the quasienergy spectrum is periodic with a period $\Omega = 2\pi/T$. In this case, the flow of the edge states need not terminate in a delocalized bulk state. Instead, the flow of the edge states can "wrap" around the quasienergy zone. In this light, it appears that it may be possible to find a system which exhibits chiral edge states, and at the same time has *all* of the bulk states localized. If this unique situation can indeed be realized, it would furthermore imply that the chiral edge states must be present at every quasienergy. Can these intriguing properties be realized in a two dimensional, disordered, periodically driven system? The current work is the first to address this question.

To prove the existence of this anomalous Floquet-Anderson insulator phase, the starting point is the model for the Anomalous Floquet topological phase described in Section 3.5. The bulk topological invariant classifying the Anomalous Floquet topological phase is the winding number (W) which is defined in Eq. (3.45). We consider this system in the presence of on-site disorder. Using numerical simulations, we explore both the weak and strong disorder regimes. We show the existence of an AFAI at weak disorder. In this phase, all the bulk Floquet states are localized, and the states on the edge pump a quantized number of charges (W) in a single time-period. As the disorder strength is increased, we find that the system undergoes a phase transition to a trivial Anderson insulator; see Sec. 8.5.

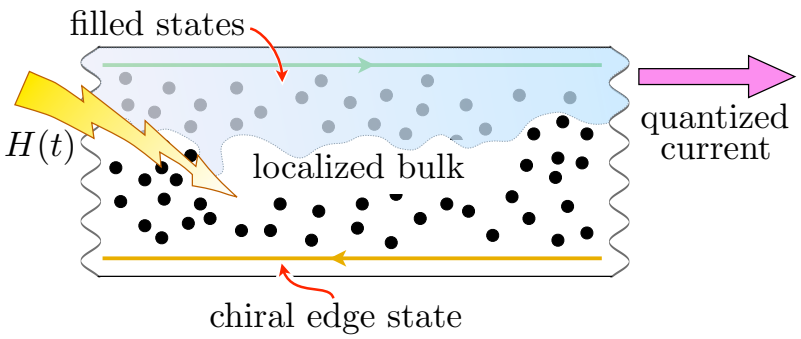

Figure 8.1: The anomalous Floquet-Anderson insulator (AFAI), in a disordered two-dimensional periodically-driven system with time-dependent Hamiltonian $H(t)$. In the AFAI phase all bulk states are localized, yet the system hosts chiral propagating edge states at all quasienergies. The nontrivial topology of the phase is characterized by a nonzero value of the winding number defined in Eq. (3.45)

The above properties describe the single particle characteristics of the AFAI, and lead to its defining characteristic as a many body system: robust *quantized charge pumping* that persists in a non-adiabatic driving regime. This behavior is in contrast to that of the one-dimensional "Thouless pump," where the pumped charge is quantized only in the limit of infinitely slow driving [105]. The setup that realizes non-adiabatic quantized pumping is illustrated in Fig. 8.1. We consider a strip of AFAI in which all of the states close to one edge are populated with fermions. In this situation, the total current flowing through the strip is quantized as an integer times the inverse driving period, $\langle I \rangle = eW/T$. Here, W is the bulk winding number characterizing the parent anomalous Floquet topological phase. The current averaged over many driving periods is $\langle I \rangle$. The quantized charge pumping is a direct result of the edge structure defined above: when the fermion occupation is of the form shown in Fig. 8.1, the edge states on one side are completely filled, while the localization of the bulk states prevents current from flowing in the direction perpendicular to the edge. In Sec. 8.4, we derive the relation between the quantization of the charge current and the bulk topological invariant, and discuss temporal fluctuations about the quantized value.

Putting together all of the characteristics described above, we may thus define the AFAI as a disordered, periodically-driven system in which all the bulk Floquet eigenstates are localized, and (i) the quasienergy independent winding number W is non-zero, (ii) chiral edge modes propagate along sample boundaries at all quasienergies, and (iii) a quantized current is pumped whenever all states along one edge are filled with fermions.

8.2 Model

In this section, we describe a simple model which allows us to explicitly demonstrate the existence and robustness of the AFAI phase. We start from a solvable model introduced in Ref. [94], which is described in Section 3.5. The schematic quasienergy spectrum for the system is shown in Fig. 8.2 (b). Without disorder, the system exhibits perfectly flat bulk Floquet bands, and hosts chiral edge modes at its boundaries. These edge modes winds around the quasienergy zone; the number of times that it winds is the bulk winding number, W.

Let us explicitly define the model that we study numerically. The clean Hamiltonian is time-periodic and piecewise-constant given by, $H_{\text{clean}}(t) = H_n$, for $\frac{(n-1)T}{5} \leq t < \frac{nT}{5}$, $n = 1, \ldots, 5$. The Hamiltonian is defined on a square lattice that is divided into two sublattices, A and B . The model for different segments is shown in Fig. 3.7. During each of the first four segments of the driving, $n = 1, \ldots, 4$, the nearest neighbor hopping matrix elements of strength J between the A and B sublattices are turned on and off in a cyclic fashion (see Fig. 3.7). To this we add a sublattice symmetry breaking potential, and disorder. The Hamiltonian for this system is

$$H(t) = H_{\text{clean}}(t) + \lambda D + V_{\text{dis}} \tag{8.1}$$

$$D = \frac{1}{2T} \sum_{\mathbf{r}} (-1)^{\eta_{\mathbf{r}}} c_{\mathbf{r}}^{\dagger} c_{\mathbf{r}} \tag{8.2}$$

$$V_{\text{dis}} = \sum_{\mathbf{r}} V_{\mathbf{r}} c_{\mathbf{r}}^{\dagger} c_{\mathbf{r}}, \tag{8.3}$$

where $H_{\text{clean}}(t)$ is the time-dependent, piecewise-constant Hamiltonian. We use the sublattice mass as D, and take the disorder potential $V_{\mathbf{r}}$ to be uniformly distributed in the interval $[-\delta V, \delta V]$. The parameters of the model are chosen to be $\lambda = \pi$, and $\delta_{AB} = 0$. We show that all in the presence of disorder, the bulk states become localized, while the edge states remain extended at all quasienergies. A fully localized bulk with chiral edge states at every quasienergy has distinct signature in transport; a quantized charge pumping every time period.

8.3 Chiral edge states in AFAI

We now concentrate on the edge structure of the AFAI, considering a system in a cylindrical geometry. To reach the AFAI phase, we envision the model in Sec. 8.2, for which all the Chern numbers of $U(T)$ vanish but with one chiral edge state on each edge running through each of the bulk gaps of the quasienergy spectrum. The setup and spectrum are shown schematically in in Figs. 8.2(a) and 8.2(b).

In the clean limit, there are chiral edge states in any bulk quasienergy gap with a non-zero winding number [94]. Clearly, these edge states cannot localize when weak disorder is added. Moreover, intuitively, if all the bulk states are localized, the chiral edge states must persist even within the spectral region of the bulk states. To see this, consider inserting a flux quantum through the hole of the cylinder. As a function of the applied flux, the chiral edge states exhibit a non-trivial "spectral flow:" even though the spectrum as a whole is periodic as a function of flux, every state evolves into the next state in the spectrum [Fig. 8.2(d)]. The spectral flow cannot terminate in the bulk bands since all the bulk states are localized and are hence insensitive to the flux. Thus there must exist a delocalized, chiral edge state at *every* quasienergy to "carry" the spectral flow.

In Fig. 8.2 (d), from the spectral flow, it is clear that the the edge states must wrap around the quasienergy zone. We label the number of times these state wrap around the zone, as the "edge winding number". It must be integer valued, and is defined as

$$n_{\text{edge}} = \sum_j \frac{T}{2\pi} \int_0^{2\pi} d\theta_x \frac{\partial \varepsilon_j}{\partial \theta_x}, \tag{8.4}$$

where the sum runs over all the eigenstates that are peaked on one edge of the cylinder, and ε_j are their corresponding quasienergy values. Note that, the edge states on the opposite edge of the cylinder wind in the opposite manner, with an edge winding number, $-n_{\text{edge}}$. This means that the *total* edge winding number of the system is zero, when the sum runs over all states [52].

A non-zero n_{edge} necessarily implies that there are delocalized states along the edge; if all states were localized, their quasi-energies would be almost insensitive to θ_x, and hence n_{edge} would be zero.

8.4 Quantized charge pumping

We now describe the quantized non-adiabatic pumping phenomenon that characterizes the AFAI phase. Consider an AFAI placed in a cylindrical geometry, as in Fig 8.2(c). In this phase, all the bulk states are localized. Now, fermions are loaded into the system such that in the initial state all the lattice sites are filled up to a distance of $\ell \gg \xi$ from one edge of the cylinder, and all the other sites are empty. Here ξ is the localization length characterizing states far from the edges of the system. Below we show that in the thermodynamic limit the current across a vertical cut through the cylinder, averaged over many driving periods, is equal to n_{edge}, the edge winding number. The exact form in which we terminate the filled

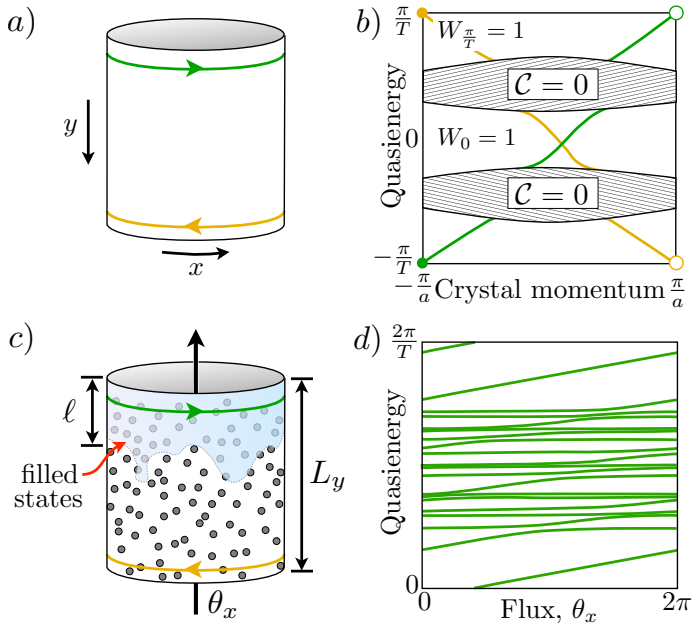

Figure 8.2: Edge states and spectral flow in the AFAI. a) The parent phase of the AFAI is a clean system without disorder, where all Floquet bands have Chern number zero but the winding number (2) is non-zero in all gaps. In a cylinder geometry, chiral edge state propagate along the upper and lower boundaries, *only* at quasi-energies within the bulk gaps. b) The corresponding spectrum, shown as a function of the conserved circumferential crystal momentum component. c) When disorder is added, all bulk states become localized while the chiral edge modes on the cylinder persist. When all states are filled near one end of the cylinder, a quantized current flows along the edge. d) With disorder, crystal momentum is no longer a good quantum number. However, the spectrum of states localized near the upper edge, displayed as a function of the flux θ_x threaded through the cylinder, clearly displays a non-trivial spectral flow. The spectral flow *fully* winds around the quasienergy zone, accounting for the quantized pumping in the AFAI phase.

region will not matter, as long as all the sites near one edge are filled, and all the sites near the other edge are empty. The system thus serves as a quantized charge pump, but unlike the quantized pump introduced by Thouless [105], there is *no requirement for adiabaticity*.

Setup

To set up the calculation of the charge pumping in the AFAI, we choose coordinates such that x is the direction along the edges of the cylinder, and y is the transverse direction. We denote the initial many-body (Slater determinant) state, in which all sites up to a distance of ℓ from the edge are filled, by $|\Psi(0)\rangle$. Then, the charge

pumped across the line $x = x_0$ between $t = 0$ and $t = \tau$ is given by

$$\langle Q \rangle_\tau = \int_0^\tau dt \Big\langle \Psi(t) \Big| \frac{\partial \tilde{H}(\theta_x, t)}{\partial \theta_x} \Big| \Psi(t) \Big\rangle. \tag{8.5}$$

Here, θ_x is the flux through the cylinder and $\tilde{H}(\theta_x, t)$ is the corresponding Hamiltonian. For concreteness, we specify a gauge in Eq. (8.5), such that on the lattice, every hopping matrix element that crosses the line $x = x_0$ has a phase of $e^{i\theta_x}$. With this choice, the current operator across the line $x = x_0$ is given by $\frac{\partial \tilde{H}(\theta_x, t)}{\partial \theta_x}$.

We are interested in the average pumped charge over N periods. Below, we show that in the limit of large N,

$$\frac{\langle Q \rangle_{NT}}{N} = Q_\infty + O\left(\frac{1}{N}\right), \tag{8.6}$$

where Q_∞ is *quantized*, $Q_\infty = W = n_{\text{edge}}$. Note that if the system is initialized in a Slater determinant of Floquet eigenstates, then the $O(1/N)$ term in Eq. (8.6) is *absent*, since then the pumped charge per period is the same in all periods: $\langle Q \rangle_T = Q_\infty$.

In order to compute the charge pumped per period, it is useful to express $|\Psi(t)\rangle$ as a superposition of Slater determinants of Floquet eigenstates. We show from numerics, in Section 8.5, that when averaging the pumped charge over N periods, the contribution of the off-diagonal terms between different Floquet eigenstates decays at least as fast as $1/N$. The diagonal terms yield a contribution that depends on the evolution over a *single* period, giving

$$Q_\infty = \sum_j n_j \int_0^T dt \langle \psi_j(t) | \frac{\partial \tilde{H}(\theta_x, t)}{\partial \theta_x} | \psi_j(t) \rangle. \tag{8.7}$$

In the above, $|\psi_j(t)\rangle$ are the single particle Floquet states, which evolve in time as $|\psi_j(t)\rangle = e^{-i\varepsilon t} |\phi_j(t)\rangle$ (where $|\phi_j(t)\rangle$ is periodic in time), and n_j are the Floquet state occupation numbers in the initial state, $n_j = \langle \Psi(0) | \psi_j^\dagger \psi_j | \Psi(0) \rangle$, where $\psi_j^\dagger$ is the creation operator corresponding to $|\psi_j(0)\rangle$.

Straightforward manipulations yield $Q_\infty = T \sum_j n_j \partial \varepsilon_j / \partial \theta_x$. At this point, the average current per period depends on θ_x. In the thermodynamic limit, we expect this dependence to disappear. As in the case of the quantization of the Hall conductance [6], we average over θ_x. We therefore get

$$Q_\infty = \frac{T}{2\pi} \sum_j \int_0^{2\pi} d\theta_x n_j \frac{\partial \varepsilon_j}{\partial \theta_x}. \tag{8.8}$$

Equation (8.8) relates the average current in a period to the spectral flow of the Floquet spectrum as the flux θ_x is threaded. It is reminiscent of the expression for the edge topological invariant, n_{edge}, Eq. (8.4). In Sec. 8.5, we present numerical evidence for the quantization of the pumped charge.

Below, we give a heuristic argument that, more generally, in the AFAI phase $Q_\infty = n_{\text{edge}}$, up to corrections that are exponentially small in ℓ. We can roughly divide the Floquet states that contribute to Eq. (8.8) into three categories:

1. States that are localized far from occupied region, $y \gg \ell$. For these states, n_j is exponentially small, and hence their contribution to Q_∞ is negligible.

2. States that are localized near the edge, $y \ll \ell$. These states have $n_j \approx 1$.

3. States that are localized near the boundary between occupied and unoccupied sites, $y \sim \ell$. For such states, n_j is neither close to 0 nor to 1; however, these states are localized in the x direction (as are all the bulk states in the AFAI). Therefore, $\partial\varepsilon_j/\partial\theta_x$ of these states is exponentially small, and they contribute negligibly to Q_∞.

As θ_x varies, there are avoided crossings in the spectrum, in which the character of the eigenstates changes. E.g., an eigenstate localized around $y_1 \ll \ell$ may undergo an avoided crossing with an eigenstate localized around $y_2 \sim \ell$. When θ_x is tuned to such degeneracy points, the two eigenstates hybridize strongly, and do not fall into either of the categories discussed above. Such resonances affect both $\partial\varepsilon_j/\partial\theta_x$ and the occupations n_j of the resonant states. However, since the eigenstates that cross are localized in distant spatial areas, the matrix element that couples them is exponentially small. Therefore significant hybridization requires their energies to be tuned into resonance with exponential accuracy, limiting the regions of deviation to exponentially small ranges of θ_x, of order $e^{-\ell/\xi}$. The number of such resonances increases only polynomially with the size of the system, and therefore for $L_y \gg \ell \gg \xi$ and $L_x \propto L_y$, their effect on Q_∞ is exponentially small. We conclude that, in the thermodynamic limit we must have, $Q_\infty = n_{\text{edge}}$.

8.5 Numerical results

Numerical simulations substantiate the conclusions of Sections 8.2–8.4. We will first briefly summarize our main findings, and then describe the simulations and results in more detail in the subsections below.

In the clean case ($\delta V = 0$), the system exhibits an anomalous Floquet-Bloch band-structure: the Chern numbers of all the bulk bands are zero, but the winding number $W_\varepsilon = 1$ for any value of ε within each of the band gaps [94]. Such a band-structure is depicted in Fig. 8.2(b). When the disorder potential is turned on, however, the system enters the AFAI phase. Below, we show numerically that the bulk states become localized, and coexist with edge states which occur in all quasi-energies. Furthermore, when the system is initialized with fermions filling all of the sites in the vicinity of one edge, while the rest remain empty, as in Sec. 8.4, the disordered system exhibits quantized amount of charge pumped per period, when averaged over long times. Finally, we examine the behavior of the system as the strength of the disorder potential is increased. We find that when the disorder strength reaches a certain critical value, the system undergoes a topological phase transition where the winding number changes from 1 to 0. For stronger disorder, a "trivial" phase (where all bulk states are localized and there are no chiral edge states) is stabilized.

Localization, edge modes, and quantized charge pumping in the AFAI

The localization properties of the bulk Floquet eigenstates of (8.1) can be extracted from the statistics of the spacings between the quasienergy levels. For localized states, the distribution of the level-spacing is expected to have a Poissonian form. In contrast, extended states exhibit level repulsion and obey Wigner-Dyson statistics [79]. To distinguish between these distributions, it is convenient to use the ratio between the spacings of adjacent quasi-energies levels [5, 16, 83]. Choosing the quasienergy zone to be between $-\pi/T$ and π/T (i.e., choosing $-i \log e^{i\varepsilon T} = \varepsilon T$ for $-\pi/T \leq \varepsilon < \pi/T$), we label quasi-energies in ascending order. We then define the level-spacing ratio (LSR) as $r = \min\{\delta_n, \delta_{n+1}\} / \max\{\delta_n, \delta_{n+1}\}$, where $\delta_n = \varepsilon_n - \varepsilon_{n-1}$. This ratio, $r \leq 1$, converges to different values for extended and localized states, depending on the symmetries of the system. For localized states, $r_{\text{loc}} \approx 0.39$ [83], while for extended states, $r_{\text{ext}} \approx 0.6$ [16]. The latter value is obtained when one assumes that the quasi-energies are distributed according to the circular unitary ensemble (CUE) [16], and in the thermodynamic limit, coincides with the value obtained by the more familiar Gaussian unitary ensemble (GUE).

Since the Floquet problem does not possess any generic symmetries such as time-reversal, particle-hole, or chiral symmetry, we expect its localization properties to be similar to those of the unitary class [3, 20, 22]. In analogy with the situation in static Hamiltonians in the unitary class [90], we expect that arbitrarily weak disorder is sufficient to localize the all Floquet states (on the torus). However, for

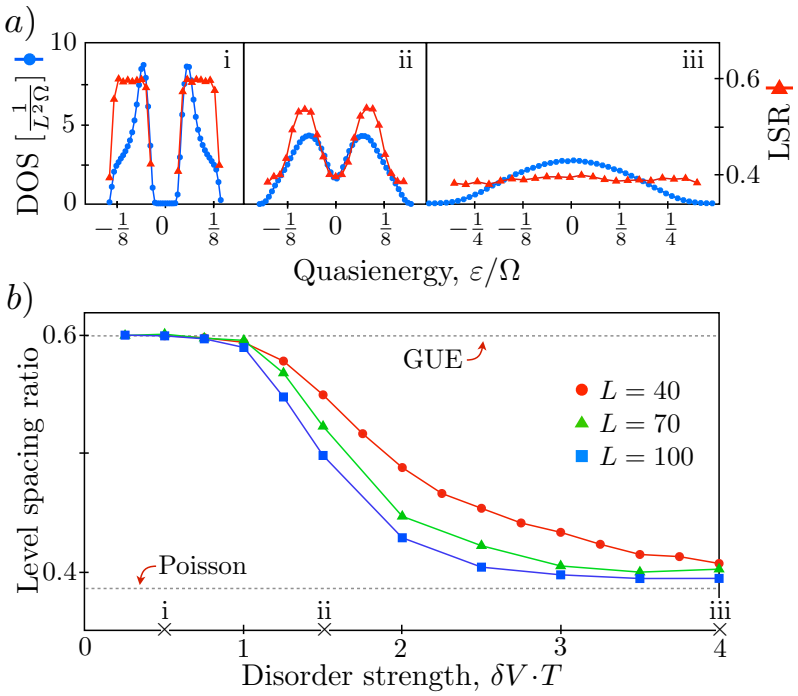

Figure 8.3: Localization of Floquet states in the AFAI as a function of disorder strength, computed for the model presented in Eq. (8.1). We use $\lambda = \pi$ and an $L \times L$ system with periodic boundary conditions. (a) Quasienergy density of Floquet states per unit area (DOS) and level spacing ratio (LSR), for three values of disorder strength as indicated by the markers on the axis of panel (b). For all cases we take $L = 70$. (b) Finite size scaling of the localization transition. Level statistics in the delocalized regime are described by the Gaussian unitary ensemble (GUE), characterized by an average level spacing ratio $r_{\text{ext}} \approx 0.60$; in the localized regime, Poissonian level statistics give $r_{\text{loc}} \approx 0.39$. These characteristic values are indicated by dashed lines.

weak disorder, the characteristic localization length ξ can be extremely long, and easily exceeds the system sizes accessible in our numerical simulations. Therefore, the level spacing ratio is expected to show a gradual crossover from having the characteristic of delocalized states, $r_{\text{ext}} \approx 0.6$, when $\xi \gg L$, to the value that indicates localized behavior, $r_{\text{ext}} \approx 0.39$, when $\xi \ll L$.

This behavior is demonstrated in Figs. 8.3(a), panels (i)–(iii), where we plot the disorder averaged level spacing ratio r and the density of Floquet states, as a function of the quasienergy for different disorder strengths. For weak disorder, $\delta V \cdot T = 0.5$, panel (i) shows that the level spacing ratio is $r \approx 0.6$ in any spectral region where Floquet states exists. On the other hand, panel (iii) shows that already for $\delta V \cdot T = 4$, the level-spacing ratio approaches $r \approx 0.39$ at all quasi energies, as expected from

localized states.

Note that, as the disorder strength increases, the level spacing ratio decreases uniformly throughout the spectrum [Fig. 8.3(a), panels (i–iii); the same behavior is seen at weaker values of the disorder (not shown)]. There is no quasienergy in which the LSR remains close to 0.6, corresponding delocalized Floquet eigenstates. This is consistent with the expectation that the bulk Floquet states become localized even for weak disorder, and the localization length becomes shorter as the disorder strength increases. The behavior of the LSR as a function of system size, Fig. 8.3(b), also shows behaviour consistent with the above expectation. In contrast, if the bulk bands of the clean systems carried non-zero Chern numbers, delocalized states would persist in the bands up to a critical strength of the disorder, at which point they would merge and annihilate.

In the AFAI phase all the bulk states are localized, but the edge hosts chiral modes at any quasienergy (cf. Sec. 8.3). To test this, we simulate the time evolution of wavepackets initialized either in the bulk or near the edge of the system. We consider the system in a rectangular geometry. The initial state, $|\psi_0\rangle$, is localized to a single site $\mathbf{r}_0 = (x_0, y_0)$. To obtain information on quasienergy resolved propagation, we investigate the disorder-averaged transmission probability, $\overline{|G_N(\mathbf{r}, \mathbf{r}_0, \varepsilon)|^2}$, which is a function both of quasienergy ε and the total time of evolution $T_f = NT$. Here, the bar denotes disorder averaging. The transmission amplitude in each disorder realization, G_N, is obtained by a partial Fourier transform of the real time amplitude, $\tilde{G}(\mathbf{r}, \mathbf{r}_0, t) = \langle \mathbf{r} | U(t) | \psi_0 \rangle$, and is given by

$$G_N(\mathbf{r}, \mathbf{r}_0, \varepsilon) = \frac{1}{N} \sum_{n=0}^{N} \tilde{G}(\mathbf{r}, \mathbf{r}_0, t = nT)\, e^{i\varepsilon nT}. \tag{8.9}$$

The real time transmission amplitude $\tilde{G}(t)$ is computed numerically by a split operator decomposition. Figs. 8.4(a),(b) show $\overline{|G_N|^2}$ at different quasi-energies, for initial states on the edge and in the bulk, respectively. The simulations are done for a disorder strength $VT = 4$. At this disorder strength, the analysis of the level-spacing statistics shown in Fig. 8.3(a) indicates that all the bulk Floquet bands are localized with a localization length smaller than the system size. Fig. 8.4(a) shows the value of $\overline{|G_N|^2}$ when the wavepacket is initialized at the edge of the system, $\mathbf{r}_0 = (1, 1)$. The wave packet propagates chirally along the edge. The figure exemplifies that the edge modes are robust in the presence of disorder, and are present at all quasi-energies. Importantly, edge states are also observed at quasi-energies where the bulk density

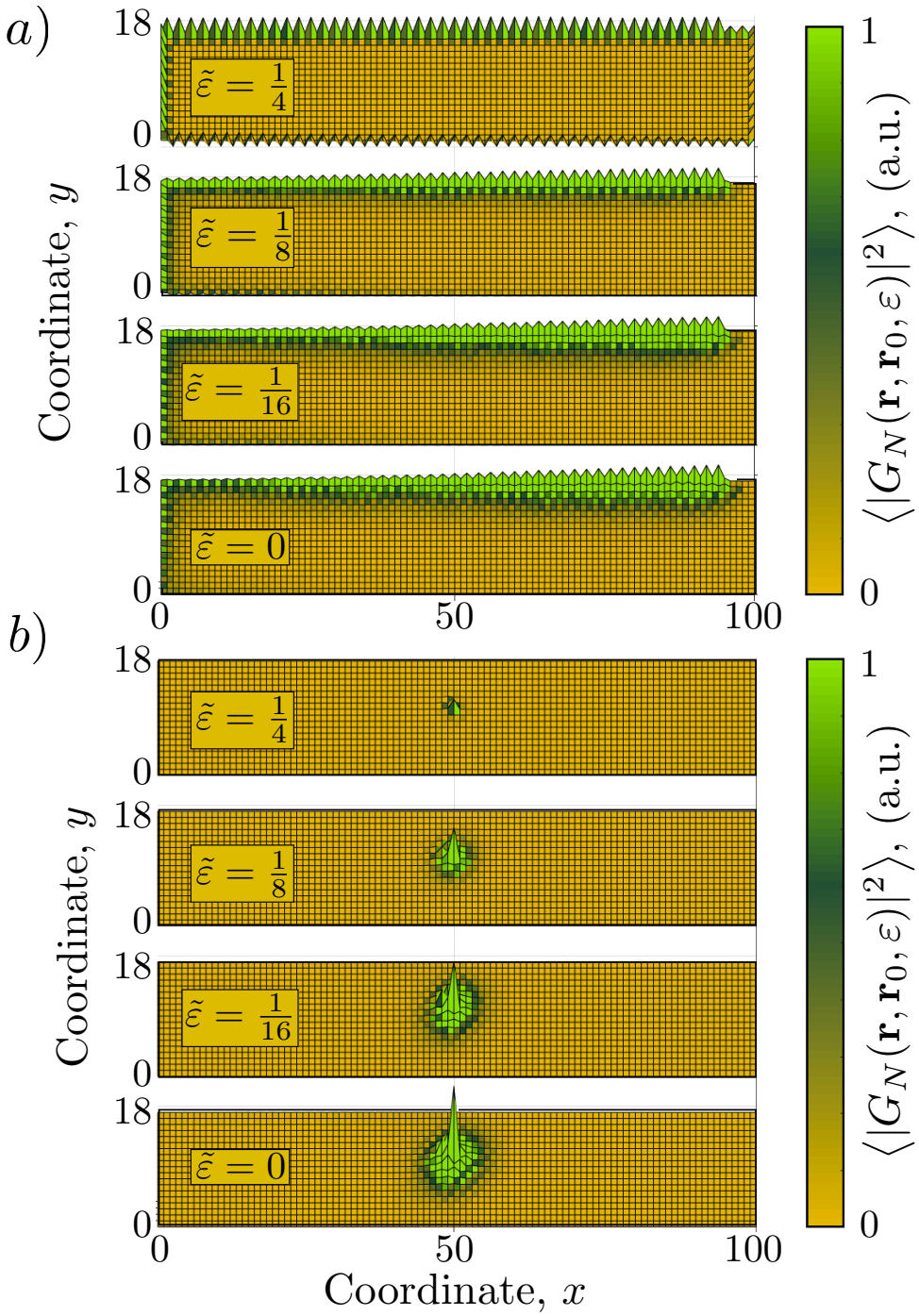

Figure 8.4: Wavepacket dynamics in the AFAI. Using the same model as in Fig. 8.3, we plot the amplitude of the transmission probability,$\langle |G_N(\mathbf{r}, \mathbf{r}_0, \varepsilon)|^2 \rangle$, c.f. Eq. (8.9) obtained after a time-evolution of $T_{\text{fin}} = 300T$ and averaged over disorder realizations. We simulate a strip of size 20×100 with open boundary conditions, and plot $\langle |G_N|^2 \rangle$ for several quasienergies $\epsilon/\Omega = 0, \frac{1}{16}, \frac{1}{8}, \frac{1}{4}$. (a) shows $\langle |G_N|^2 \rangle$ when the initial wavepacket is chosen at the edge $\mathbf{r}_0 = (96, 1)$. It indicates the presence of a robust edge mode at all the given quasi-energies. (b) shows the probability when the initial wavepacket is chosen in the bulk, $\mathbf{r} = (50, 10)$. This indicates that the bulk Floquet states are localized. These simulations were carried out with a time step of $dt = T/100$.

of states is appreciable, indicating that the chiral edge states coexist with localized bulk states [the density of states in the bulk is shown in Fig. 8.3(a)].

In contrast, Fig. 8.4(b) shows $\overline{|G_N|^2}$ for a wavepacket initialized in the middle of the system. The wavepacket remains localized at all quasi-energies, as expected if all bulk Floquet eigenstates are localized. This confirms that the model we study numerically indeed exhibits the basic properties of the AFAI phase: fully localized Floquet bulk states, coexisting with chiral edge states which exist at every quasienergy.

Next, we numerically demonstrate the quantized charge pumping property of the AFAI. Using the model described above, we numerically compute the value of $\overline{Q}_\infty$ given by Eq. (8.7) for a single value of the flux, $\theta_x = 0$. When computing $\overline{Q}_\infty$, we averaged the charge pumped across all the lines running parallel to the y direction of the cylidner (see Fig. 8.2), as well as over 100 disorder realizations. In Fig. 8.5(a), we show the cumulative average of the pumped charge per cycle in the limit of long times, $\overline{Q}_\infty$ [c.f. Eq. (8.7)] as a function of disorder strength. At weak disorder, when the localization length is smaller than the system size, $\overline{Q}_\infty$ is clearly not quantized. However, for disorder strength $\delta V \cdot T \gtrsim 5$, the value of $\overline{Q}_\infty$ quickly tends towards unity. This agrees with the results presented in Fig. 8.3(a.iii), which indicate that at this disorder strength, the localization length is substantially smaller than $L = 70$. Finite size scaling demonstrating that $\overline{Q}_\infty$ indeed asymptotes to unity in the thermodynamic limit is presented in the inset of Fig. 8.5(a).

The value of the cumulative average of the pumped charge over N periods, $\overline{\langle Q\rangle}_{NT}/N$ [c.f. Eq. (8.5)] is plotted vs. N in Fig 8.5(b), demonstrating its approach to $\overline{Q}_\infty$ for large values of N (i.e., at long times). As in panel (a), we averaged over all the lines running parallel to the y direction, and over 100 disorder realizations. We examine the asymptotic behavior of $\overline{\langle Q\rangle}_{NT}$ and find a power law behaviour of the form $\overline{\langle Q\rangle}_{NT} = \overline{Q}_\infty + cN^{-\upsilon}$ with $\upsilon = 1.72$, shown in the inset of panel (b). Therefore, this shows a power-law behaviour with a power larger than 1 and no oscillations; this is clearly the result of averaging over the frequencies appearing in $\langle Q\rangle_{NT}/N$ for each disorder realization and vertical cut. The above results numerically confirm the discussion in Sec. 8.4, and conclude our numerical analysis of the AFAI phase.

Strong Disorder Transition

For sufficiently strong disorder, we expect the AFAI to give way to a topologically trivial localized phase in which the winding number vanishes. We now analyze

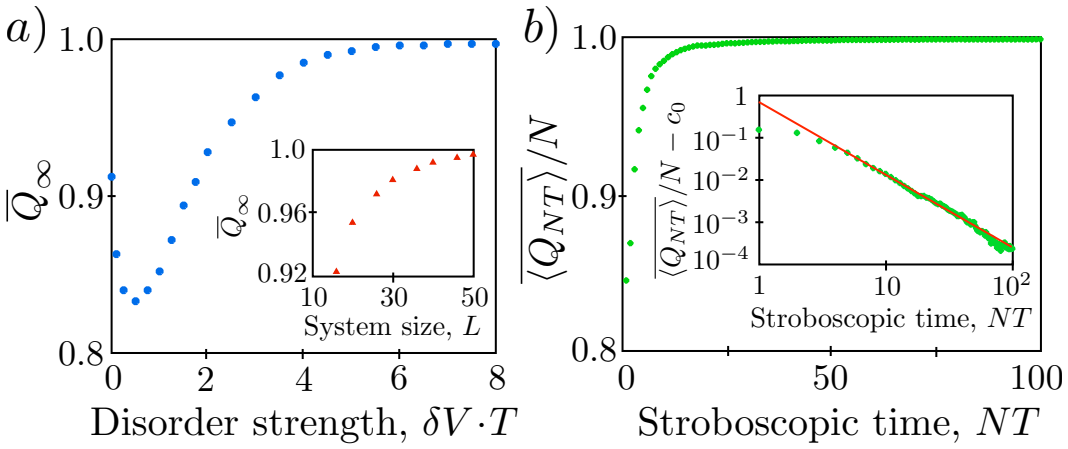

Figure 8.5: Quantized charge pumping in the AFAI. (a) Cumulative average of the pumped charge per cycle in the limit of long times, $\overline{Q}_\infty$, [c.f. Eq. (8.7)], as a function of disorder strength. For $\delta V \cdot T \gtrsim 5$, the localization length is sufficiently smaller than the system size, and $\overline{Q}_\infty$ approaches unity. The inset shows the finite size scaling of $\overline{Q}_\infty$ for $\delta V \cdot T = 8$. (b) Cumulative average of the pumped charge for N periods, $\overline{\langle Q\rangle}_{NT}/N$, as a function of N. The disorder strength used was $\delta V \cdot T = 8$. The approach to the quantized value can be fit to a power law $(NT)^{-\upsilon}$ with $\upsilon = 1.72$, see the log-log plot shown in the inset. In both panels, we averaged the charge pumped across all the lines running parallel to the y direction of the cylinder (see Fig. 8.2) and over 100 disorder realizations. The system size used $L_x \times L_y = 50 \times 50$.

the transition between the AFAI and this "trivial" phase. As explained above, the winding number W_ε can only change if a delocalized state crosses through the quasienergy ε as disorder is added. In the AFAI phase all of the bulk states are already localized. How does the transition between the two phases occur?

Clearly, at the transition, delocalized states must appear in the quasienergy spectrum. As disorder is increased, the delocalized states must sweep the full quasienergy zone, changing the topological invariant W_ε as they do so. The transition from the AFAI phase to the trivial phase can therefore occur through a range of disorder strength $\delta V_c^- < \delta V < \delta V_c^+$, where δV_c^- is the disorder strength at which the first delocalized state appears, and δV_c^+ is the disorder strength at which all Floquet states are again localized, and $W_\varepsilon = 0$ for all ε. Below we will support this scenario using numerical simulations, and furthermore provide evidence suggesting that the transition is of the quantum Hall universality class.

We study the same model used in Sec. 8.5 and examine the level-spacing ratio, r, as a function of disorder strength and quasienergy. For this model, our simulations indicate $\delta V_c^- \approx \delta V_c^+$, within our resolution (limited by the system size). In Fig. 8.6(a),

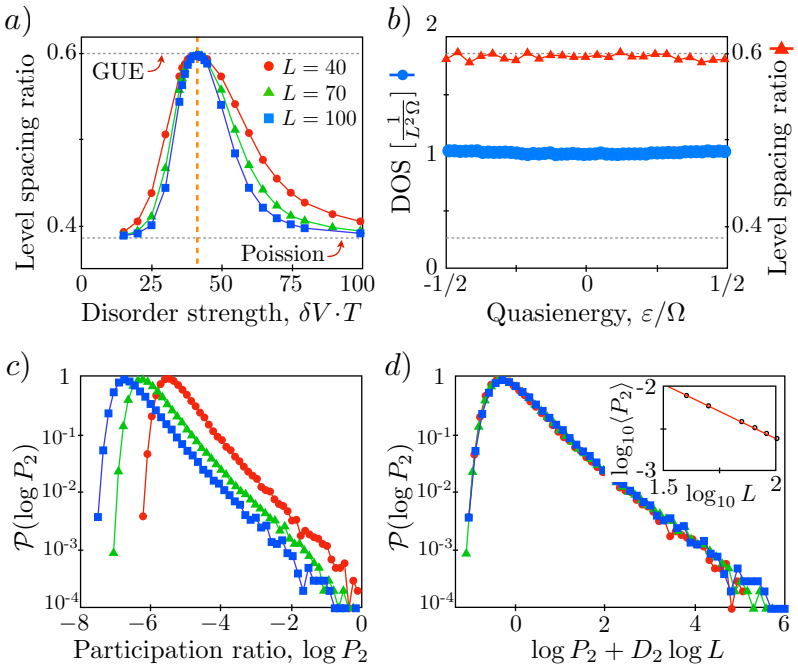

Figure 8.6: Transition from the AFAI into a trivial phase at strong disorder. (a) Average level spacing ratio as a function of disorder strength. On increasing disorder strength, a transition is observed between two localized phases with delocalized levels at $\delta V \cdot T \approx 40$. Here, the level-spacing ratio has been averaged over all quasi energies. (b) Level spacing ratio as a function of quasienergy and its comparison with the DOS, indicating that the entire Floquet band is delocalized. (c) Effect of finite size of on the distribution of the participation of ratio, P_2, at a given disorder strength, $\delta V \cdot T = 40$. The system sizes used for the simulations are $L_x \times L_y = 40\times40$, 70×70, 100×100. The shape of the curve does not change, indicating a critical phase. (d) Scaling collapse of the three curves with $D_2 = 1.3$, where for a critical phase it is expected that $\langle P_2 \rangle \sim L^{-D_2}$.

we plot r, averaged over disorder realizations and all quasi-energies. We see that at disorder strength $\delta V_c \cdot T \approx 40$ the level spacing ratio reaches $r \approx 0.6$, indicating delocalization. On either side of this point, r approaches 0.39 as the system size increases, which indicates localization. The peak in the value of r as a function of disorder gets sharper for larger system size, which is a signature of a critical point of this transition. In Fig 8.6(b), we show that at disorder strength δV_c, the LSR is independent of the quasienergy with $r \approx 0.6$ (for disorder strengths close to V_c, we also find that the LSR is independent of the quasienergy, but with $r < 0.6$). This indicates that all of the Floquet states have a delocalized character at this disorder strength, which leads us to conclude that $\delta V_c = \delta V_c^- \approx \delta V_c^+$.

At the critical point, $\delta V = \delta V_c$, we expect the wavefunctions to have a fractal

character [74]. This behavior is manifested in the distribution of the inverse participation ratio (IPR), $P_2 = \sum_{\mathbf{r}} |\psi(\mathbf{r})|^4$. We study the distribution of the IPR, $\mathcal{P}(\log P_2)$, among all the Floquet eigenstates and averaged over disorder realizations. Fig. 8.6(c) shows the distribution for different system sizes. We note that the shapes of the distributions for different sizes are similar, a signature of criticality. In two dimensions, the average value of the IPR at a critical point is expected to scale like $\langle P_2 \rangle \sim L^{-D_2}$, with $D_2 < 2$ [74]. Fig. 8.6(d) shows the scaling collapse of all the distributions. From the collapse we find the fractal dimension, $D_2 = 1.3$. The inset in this figure also shows a linear scaling $\log \langle P_2 \rangle \sim -D_2 \log L$. The critical exponent D_2 we find in our numerical simulations is close to the value found for the universality class of quantum Hall plateau transitions [40, 74], $D_2 \approx 1.4$, indicating that the transition from the AFAI to the trivial phase may belong to this universality class. This is natural to expect, since, like the quantum Hall transition, in the transition out of the AFAI phase a delocalized state with a non-zero Chern number must "sweep" through every quasienergy, to erase the chiral edge states. We expect that the AFAI transition can be described in terms of "quantum percolation" in a disordered network model, similar to the Chalker-Coddington model for the plateau transitions [14]. We leave such investigations for future work.

8.6 Discussion

In this work we have demonstrated the existence of a new non-equilibrium phase of matter: the anomalous Floquet-Anderson insulator. The phase emerges in the presence of time-periodic driving and disorder in a two-dimensional system, and features a unique combination of chiral edge states and a fully localized bulk. Such a situation cannot occur in non-driven systems, where the presence of chiral edge states necessarily implies the existence of delocalized bulk states where the chiral branches of the spectrum can terminate. In a driven system, the periodicity of the quasienergy spectrum alleviates this constraint, allowing chiral states to "wrap around" the quasienergy zone and close on themselves.

One of the key physical manifestations of the AFAI is a new type of *non-adiabatic* quantized pumping, which occurs when all states near one edge of the system are filled. It is interesting to compare this phenomenon with Thouless' quantized *adiabatic* pumping, described in Ref. [105].

The complementary relationship between pumping in the AFAI and the Thouless case is best revealed by first viewing the Thouless pump from the point of view of

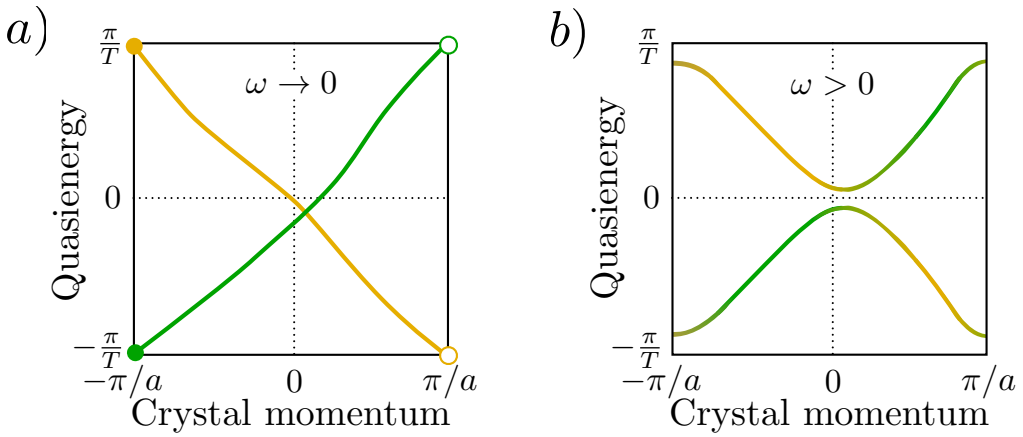

Figure 8.7: Floquet spectrum for Thouless' quantized adiabatic charge pump. a) Quantized adiabatic pumping in a 1D system is manifested in chiral Floquet bands that wind around the quasienergy Brillouin zone (right and left movers are shown in green and orange, respectively). b) Outside of the adiabatic limit, $\omega > 0$, counterpropagating states hybridize, and all Floquet bands obtain trivial winding numbers; quantized pumping is destroyed.

its Floquet spectrum. In Thouless' one-dimensional pump, a periodic potential is deformed adiabatically such that in each time cycle a quantized amount of charge is pumped through the system. In the adiabatic limit, the quasienergy spectrum of the pump exhibits one pair of counter propagating one-dimensional chiral Floquet-Bloch bands, which wrap around the quasienergy Brillouin [see Fig. 8.7(a)]. The (nonzero) quasienergy winding number of each band gives the associated quantized pumped charge [52]. Importantly, for any finite cycle time the two counter-propagating states hybridize and destroy the perfect quantization of the charge pumped per cycle [Fig. 8.7(b)].

In a strip geometry, the AFAI can be viewed as a quasi-one-dimensional system. As discussed in Sec. 8.3, the system hosts chiral edge states that run in opposite directions on opposite edges. Furthermore, as shown by the spectral flow (see Fig. 8.2), these counterpropagating chiral modes cover the entire quasienergy zone, analogous to the counter-propagating modes of the Thouless pump [Fig. 8.7(a)]. Crucially, however, the counterpropagating modes of the AFAI are *spatially separated* and therefore their coupling is *exponentially suppressed*: no adiabaticity restriction is needed to protect quantization. Thus quantized pumping at finite frequency can be achieved in the AFAI phase.

How is the AFAI manifested in experiments? First, the localized bulk and chiral

propagating edge states could be directly imaged, for example in cold atomic or optical setups. More naturally for a solid state electronic system, the pumping current could be monitored in a two terminal setup. Unlike the case of an adiabatic pump, where a quantized charge is pumped at zero source-drain bias, to observe quantized charge pumping in the AFAI the chiral propagating states of one edge of the system would need to be completely filled at one end of the sample, and emptied at the opposite end. We speculate that this can be achieved using a large source-drain bias. A detailed analysis of such non-equilibrium transport in a two or multi-terminal setup, as well as an investigation of promising candidate systems, are important directions for future study. While the model presented in Sec. 8.2 can be implemented directly in a variety of systems, including all-optical, microwave resonator systems, and even cold-atomic systems, we expect that the AFAI to be realized using other classes of models, such as those based on standard bandstructures with a weak uniform drive.

Chapter 9

OUTLOOK AND FUTURE DIRECTIONS

In this part, we studied the various effects of disorder. We showed the robustness of the Floquet topological phases to disorder and the presence of novel phases that require both disorder and a drive to be topological. We showed the route to realizing a non-adiabatic Thouless pump, in a two dimensional set up in the presence of sufficiently strong disorder. In that case, Anderson localization protects the quantized nature of the pump.

There are several directions that would be of interest in continuation of the results described in this part. An important step to studying the critical properties of the localization transitions in the Floquet topological phases would be to develop a Chalker-Coddington network model for the Floquet topological insulator and the Anomalous Floquet topological phases.

As a generalization of our results, one can consider constructing topological and anomalous Floquet insulators in different dimensions and symmetry classes. Floquet-Bloch band structures, which generalize those of Ref. [94], can serve as a starting point for constructing such anomalous periodically driven systems.

Going beyond the single particle level, an important challenge is to understand how the properties of the AFAI change in the presence of interactions. An exciting possibility is to obtain a topologically non-trivial steady state for an interacting, periodically driven system [11, 17, 18, 42, 99]. The common wisdom dictates that a periodically system with dispersive modes is doomed to evolve into a highly random state which is essentially an infinite temperature state as far as any finite order correlation functions are concerned [16, 63, 64, 88, 89, 93]. In demonstrating the existence of the AFAI phase, we have shown that on the single particle level, it is possible to realize a topological Floquet spectrum with no delocalized states away from the edges of the system. It is therefore possible that such periodically driven systems can serve as a good starting point for constructing topologically non-trivial steady states for interacting, disorder (many-body localized) periodically driven systems [50]. The types of topological steady states that can be obtained by this method, and their observable signatures, will be interesting subjects for future work.

Part III

Wegner flow-equations to study Anderson transitions

The consequences of Anderson localization has been studied experimentally and numerically over the past several decades [22, 58]. Localization effects took center-stage recently, with theory, numerics and experiments in cold atoms probing weakly interacting disordered systems [7, 8, 41, 75, 87, 91, 98, 111]. The focus of these studies is the many-body localized state, where electron-electron interactions fail to thermalize the system, and the rules of statistical mechanics do not hold [41, 86, 111]. This state is predicted to exist even at infinite temperature where the analyses of highly excited states become relevant [83]. This implies a need to develop analytical tools that address the full spectrum of the Hamiltonian.

The daunting task of accounting for the behavior of excited states anywhere in the spectrum requires a scheme that extracts the important elements in the Hilbert space and the Hamiltonian. Such a task has been successfully accomplished, for instance, with the SDRG-X technique [87], a generalization of the Ma and Dasgupta's proposal [12, 76], and recently applied to a variety of disordered systems [2, 118]. Another path to such a scheme could be the flow equation technique. This technique was introduced by Wegner [114], in the context of condensed matter, and, concomitantly, by Glasek and Wilson [28, 29], in the high energy physics. We focus on employing this technique to address localization (Anderson) transitions.

In this part, we describe the adaptation of the flow equation technique to study Anderson transitions in non-interacting one dimensional systems with long-range hopping. As discussed in Chapter 1, scaling analysis [1] shows that the typical wave function of disordered system in one or two dimensions decays exponentially in a non-interacting system with short-range hopping. Three-dimensional systems, however, possesses a highly interesting delocalization transition, exhibiting multi-fractal wavefunctions [22]. Interestingly, such a transition could also occur in one dimension as long as the hopping could be longer ranged [21, 66, 81]. In particular, consider hopping terms with a random magnitude, and a variance that decays as a power law with distance. The metal-to-insulator transition is obtained by tuning the power-law exponent, α, with the critical point at $\alpha = 1$. The connectivity of the system makes it behave as effectively higher dimensional, with the dimension related to the power law exponent α. We discuss the details of this model in Chapter 11.

The flow analysis we develop allows us to study the full phase diagram of the power-law hopping system. We show that, for $\alpha < 0.5$, the distribution of hoppings flows to an attractive fixed point at $\alpha = 0$. This means that the phase for $\alpha < 0.5$ is in

the Gaussian Orthogonal Ensemble (GOE) with extended states. For $0.5 < \alpha < 1$, the states have critical and intermediate statistics. In this regime, we recast the flow as a controlled strong-bond RG procedure, and recover the full-spectrum with appropriate level statistics. The strong-bond RG flow produces the spectrum of energy differences from the largest to smallest, iteratively, while also generating a diffusion in the space of hopping strengths. The level repulsion for $\alpha < 1$ emerges as a consequence of a crossover of the hopping distribution function from power-law to uniform at the average level spacing scale. The method is even more successful for $\alpha > 1$, where localization emerges, associated with Poisson statistics of the level spacings.

We first introduce the flow equation method in Chapter 10. Then, in Chapter 11 we review the model of non-interacting particles with power-law hopping model, the Power-Law Banded Random Matrix (PBRM). We briefly explain the phases that have been previously found by Mirlin *et al.*[81] and Levitov [65, 66]. In Chapter 12, we introduce the flow equation (FE) method, focusing on its application to this model at $\alpha < 0.5$. The flow reveals an attractive fixed point at $\alpha = 0$. Then, we introduce the strong-bond RG scheme that consists of eliminating hopping in bonds (as opposed to sites, as proposed in Ref. [43]). We discuss the bond selection and how it can be derived from the two-site and 3-site flow equations. We explain the appearence of level repulsion as a function of the exponent, $\frac{1}{2} < \alpha < 1$.

Chapter 10

WEGNER FLOW EQUATIONS : INTRODUCTION

The flow equation technique (FET) was first introduced independently by Wegner [114], and Glasek and Wilson [28, 29]. It iteratively constructs a unitary transformation that continuously diagonalizes a Hamiltonian as a function of some RG flow time Γ. The advantage of utilizing this method to obtain the spectrum is that the entire Hilbert space of the Hamiltonian is preserved. Therefore, this method is useful when it is necessary to know the properties of highly excited states.

In the framework of conventional renormalization group, the largest energy scales in the problem (UV cutoff) is removed. The high-energy cutoff is reduced iteratively to the experimentally relevant energy scale. As one performs this procedure, the coupling constants in the Hamiltonian flow to different fixed points that characterize the ground states and low energy excited states. This procedure is schematically shown in Fig. 10.1. The bare Hamiltonian is shown as green matrix with the energy scale between 0 and Λ. The renormalization group procedure removes degrees of freedom associated with high energies (shown schematically as the grey region) in the range $[\Lambda - \delta\Lambda, \Lambda]$.

The basic idea of the flow equation technique is to retain the full Hilbert space. This is done by iteratively removing scales that connect energy differences larger than the running cutoff, Λ_{feq}. This procedure makes the Hamiltonian more band diagonal as the Hamiltonian flows in the RG time, Γ. We schematically show this in Fig. 10.1. In the following, we outline the method to generate this sequence of Hamiltonians, $H(\Gamma)$, as proposed by Wegner [114]. We have the following conditions on the sequence, (i) $H(\Gamma = 0)$ is the Hamiltonian in the original basis, and (ii) $H(\Gamma \to \infty)$ is diagonal, and is in the eigenbasis of the Hamiltonian.

In order to generate a sequence of Hamiltonians that are successively more band-diagonal, it is necessary to perform infinitesimal unitary transformations on the Hamiltonian. We represent the transformation from Γ to $\Gamma + \delta\Gamma$ as

$$H(\Gamma + \delta\Gamma) = \exp(\eta\delta\Gamma) H(\Gamma) \exp(-\eta\delta\Gamma), \tag{10.1}$$

where we have used an antihermitian generator, $\eta(\Gamma) = -\eta^{\dagger}(\Gamma)$, for the unitary tranformation. We can rewrite this as a function of the continuous parameter, Γ as

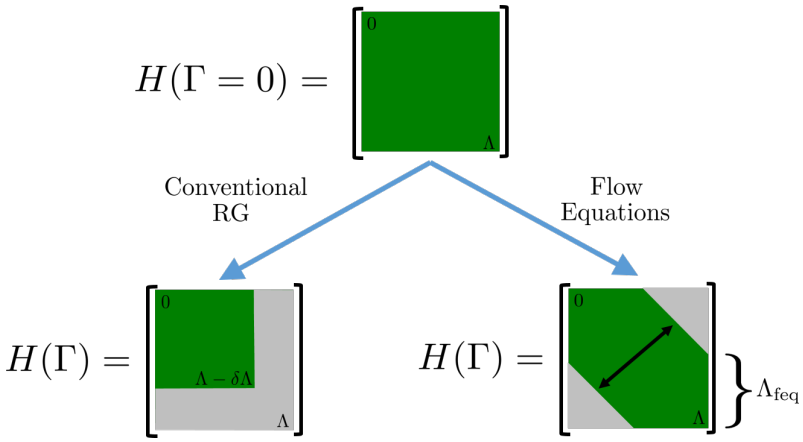

Figure 10.1: Schematic view of flow equations in comparison conventional RG. Both procedure can be viewed as a flow of the couplings as a function of a RG time, Γ. In conventional RG, the largest energy scales, Λ are eliminated. As the energy scale is reduced, $\Lambda \to \Lambda - d\Lambda$, the effective Hamiltonian describes the physics at this energy scale. In the flow equation approach, the Hamiltonian becomes successively more band diagonal, with a band width given by Λ_{feq}. We expect, $\Lambda \propto \Gamma^{-\frac{1}{2}}$.

the differential equation,

$$\frac{d}{d\Gamma} H(\Gamma) = [\eta(\Gamma), H(\Gamma)], \tag{10.2}$$

with the initial condition that $H(\Gamma = 0)$ is the Hamiltonian in the original basis. The unitary operator that diagonalizes the Hamiltonian becomes $U(\Gamma) = \mathcal{T}_\Gamma \exp\left(\int^\Gamma d\Gamma' \eta(\Gamma')\right)$, where $\mathcal{T}_\Gamma$ denotes RG-time ordering. The solution to the differential equation in Eq. 10.2, $H(\Gamma)$ are all unitarily equivalent to $H(\Gamma = 0)$ for all Γ. We still need to choose $\eta(\Gamma)$ carefully such that the Hamiltonian sequence satisfies the condition: $H(\Gamma \to \infty)$ must be diagonal.

We set the coupling constants in the bare Hamiltonian to be functions of the RG time and split it into two parts, $H_0(\Gamma)$ and $V(\Gamma)$:

$$H(\Gamma) = H_0(\Gamma) + V(\Gamma). \tag{10.3}$$

In order to obtain the infinitesimal rotation generator, the Hamiltonian is split into diagonal (H_0) and off-diagonal parts (V). Note that the choice of terms as diagonal and off-diagonal dependents on the choice of basis. Now, following Wegner [114], the canonical generator for the infinitesimal unitary transformations is defined as

$$\eta(\Gamma) = [H_0(\Gamma), V(\Gamma)]. \tag{10.4}$$

By definition the generator is antihermitian. The differential equation for the flow of the Hamiltonian is expressed through an Heisenberg equation of motion with respect to RG time which is the same as Eq. (10.2). The dimensions of $\eta(\Gamma) \sim [H^2] \sim (\text{Energy})^2$. Since the term, $\eta\delta\Gamma$ is dimensionless, the scaling of the RG time with energy is, $\Gamma \sim (\text{Energy})^{-2}$. This allows us to define the cutoff bandwidth (see Fig. 10.1) as a function of the RG time, $\Lambda_{\text{feq}} \propto \Gamma^{-1/2}$.

This generator ensures convergence to a diagonal Hamiltonian in the limit $\Gamma \to \infty$ if the condition $\text{Tr}\left(\frac{dH_0}{d\Gamma}V\right) = 0$ is fulfilled, where the trace is taken over all basis states in the Hilbert space. This condition is always true, when we split the Hamiltonian into (i) H_0 is diagonal, and does not change the quantum numbers of the basis states, and (ii) V is a term that changes the quantum number of the basis state. Now, using this condition, it becomes simple to prove that [49]

$$\frac{d}{d\Gamma}\text{Tr}\left[V\left(\Gamma\right)\right]^2 = -2\text{Tr}\left(\eta^\dagger\eta\right) \leq 0, \tag{10.5}$$

where we used that $\eta^\dagger\eta$ is positive. Consequently, as long as η does not vanish, we must have the off-diagonal terms vanish, $V\left(\Gamma\right) = 0$ as $\Gamma \to \infty$. In the following section, we apply the flow equation technique to study a simple Hamiltonian.

10.1 Simple Example: Spin-1/2 in Magnetic field

Let us diagonalize the Hamiltonian describing a spin-$\frac{1}{2}$ particle in a magnetic field. Consider a magnetic field parallel to the xz plane, the Hamiltonian is

$$H = h\sigma_z + J\sigma_x, \tag{10.6}$$

where J and h are such that $\sqrt{J^2 + h^2} = 1$. This Hamiltonian is 2×2 matrix which can be exactly diagonalized to obtain the eigenvalues which are ± 1. We now solve this eigenvalue problem using flow equations. We promote the constants, J and h to be a function of RG time, Γ. Define, $H_0(\Gamma) = h(\Gamma)\sigma_z$ and $V(\Gamma) = J(\Gamma)\sigma_x$. The generator is given by

$$\eta(\Gamma) \quad = \quad [H_0, V] = i2hJ\sigma_y, \tag{10.7}$$

where we drop the dependence on Γ on the variables J and h. The equation of motion for $H\left(\Gamma\right)$ (see Eq. (10.2)) becomes

$$\begin{aligned} \frac{dH}{d\Gamma} &= [\eta, H] \\ &= -4hJ\left(h\sigma_x - J\sigma_z\right) \end{aligned} \tag{10.8}$$

Using Eqs. (10.6) and (10.8), we find

$$\frac{d}{d\Gamma}h\left(\Gamma\right) = 4h\left(\Gamma\right)J\left(\Gamma\right)^2 \tag{10.9}$$

$$\frac{d}{d\Gamma}J\left(\Gamma\right) = -4h\left(\Gamma\right)^2 J\left(\Gamma\right) \tag{10.10}$$

with the initial conditions $h\left(0\right) = h$, and $J\left(0\right) = J$. We note the above equations have a conserved quantity, $h^2\left(\Gamma\right) + J^2\left(\Gamma\right) = \text{const.}=1$, which describes a circle in the parameter space. Parametrization in terms of trigonometric functions, $h\left(\Gamma\right) = \cos\theta\left(\Gamma\right)$, and $J\left(\Gamma\right) = \sin\theta\left(\Gamma\right)$, transform the FE into single variable problem,

$$\frac{d}{d\Gamma}\theta\left(\Gamma\right) = -2\sin\left(2\theta\left(\Gamma\right)\right), \tag{10.11}$$

which gives the solution,

$$\theta\left(\Gamma\right) = \arctan\left(\frac{J}{h}e^{-4\Gamma}\right). \tag{10.12}$$

We note that the time-scale for the decay of the angle, $\theta(\Gamma)$ is set by the conserved quantity, $\Gamma_{\text{decay}} \sim \frac{1}{J^2+h^2}$. This observation ties into the scaling between the RG time and the cutoff Λ_{feq}. In this case the cutoff scale is set by, $\Lambda_{\text{feq}} = \sqrt{J^2 + h^2}$. In the limit , $\Gamma \to \infty$, the parametric angle, $\theta\left(\Gamma\right)$ vanishes, which implies $h\left(\infty\right) = 1$ and $J\left(\infty\right) = 0$, so that the Hamiltonian is diagonal and the eigenvalues are ± 1.

Another equivalent way of finding the eigenvalues is using the unitary transformation explicitly

$$\begin{aligned} H\left(\Gamma\right) &= e^{\int_0^\Gamma d\Gamma'\eta}H\left(0\right)e^{-\int_0^\Gamma d\Gamma'\eta}, \\ \text{with}\int d\Gamma'\,\eta\left(\Gamma'\right) &= -i\sigma_y\frac{1}{2}\arctan\left(\frac{J}{h}\right), \end{aligned} \tag{10.13}$$

where the angular momentum operator is $S_y = \frac{1}{2}\sigma_y$, and so the rotation angle is $\theta = \arctan\left(\frac{J}{h}\right)$. This is exactly the rotation that diagonalizes the Hamiltonian

$$e^{-i\theta S_y}\left(h\sigma_z + J\sigma_x\right)e^{i\theta S_y} = \sigma_z, \tag{10.14}$$

which have the eigenvalues ± 1.

This simple example illustrates the basic steps of how to implement the flow equations for a generic Hamiltonian. The first step is to split H into H_0 and V such that $\text{Tr}\left(\frac{dH_0}{d\Gamma}V\right) = 0$. After that, the computation of $\eta = [H_0, V]$ and the flow equations is straightforward algebra. In this case the solution is exactly solvable. We have

shown the exponential decay in Γ of the off-diagonal operator V. In general, the flow equations are set of coupled differential equations and it is not possible to analytically solve them exactly. In the Chapter 12, we employ FET to study disordered Hamiltonians. The flow equations can be solved numerically, and we employ different approximations to study the solution in different limits of the problem.

Chapter 11

ANDERSON TRANSITIONS IN POWER-LAW RANDOM BANDED MATRICES

The system we seek to analyze consists of a one-dimensional chain of non-interacting particles with random on-site disorder and random hoppings whose typical strength decays algebraically as a power-law with site distance. This is the so-called Power-Law Banded Matrix (PBRM) model. It exhibits an Anderson transition despite its low dimensionality. The Hamiltonian in second-quantized notation is

$$H = \sum_{i,j} J_i^j c_i^\dagger c_j + \sum_i h_i c_i^\dagger c_i, \tag{11.1}$$

where h_i and J_i^j are random uncorrelated variables; the standard deviation of J_j^i decays with distance as $\sigma_{J_i^j} \sim \frac{1}{|i-j|^\alpha}$. No further assumptions regarding the distributions are necessary. The operators $c_i^\dagger$ (c_i) creates (annihilates) a particle at site i.

The exponent $\alpha > 0$, which describes power-law decay of long-range hopping, is the tuning parameter for a localization-delocalization transition (see Fig. 11.1). This model has been previously studied both by numerical techniques, such as exact diagonalization [21], and analytical techniques, such as super-symmetric methods [81] and real-space RG [65, 66, 80] . In the following, before proposing a new method to tackle the problem, we review some of the known properties of the model and give a qualitative description of the phase transition.

The localized and delocalized phases: Let us examine the model, defined in Eq. (11.1) for the two limiting cases, $\alpha = 0$ and $\alpha \to \infty$. In the limit $\alpha = 0$, the Hamiltonian corresponds to a random matrix in the Gaussian Orthogonal Ensemble (GOE). The properties of the eigenstates are given by Random Matrix Theory (RMT) and so, the eigenvalues experience level repulsion and the level spacing distributions obey the Wigner-Dyson statistics [79]. The phase is, therefore, delocalized and all the single-particle orbitals are extended. In the opposite limit, $\alpha \to \infty$, only nearest-neighbor interactions are non-zero and the Hamiltonian realizes an Anderson Insulator phase [4]. In such phase, all the orbitals are known to be localized. In contrast with the delocalized phase, the single-particle energies are uncorrelated and the level spacing exhibits Poisson statistics [9, 59].

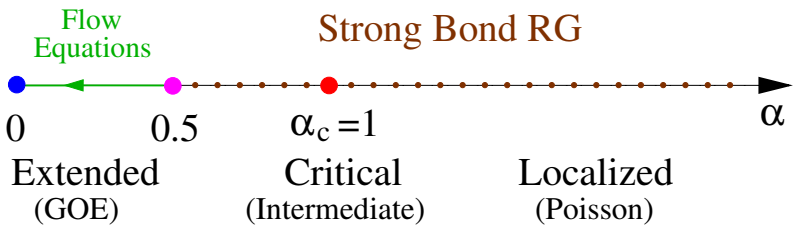

Figure 11.1: Phase diagram of PBRM model, Eq. (11.1), with disordered on-site potential and random hoppings decaying algebraically with range as $J_{ij} \sim \frac{1}{|i-j|^{\alpha}}$. For $\alpha < \frac{1}{2}$, the system is equivalent to the $\alpha = 0$ Gaussian Orthogonal Ensemble (GOE). This region is studied by the flow equation technique. For $\alpha > \frac{1}{2}$, a strong-bond RG flow scheme based on the flow equations allows us to accurately study the level statistics. This RG scheme does not eliminate any degrees of freedom, but consists of a sequence of unitaries. The critical point for the transition to a localized phase is at $\alpha_c = 1$. The level-spacing statistics in this phase transitions to Poisson statistics.

The Critical point: This model exhibits a critical point at the exponent $\alpha = 1$. The eigenstates exhibit multifractality, and the eigenvalues experience level repulsion with intermediate statistics. The transition from localized to extended states is mediated by a proliferation of resonances whose length scales with system size.

The localization-delocalization transition is driven by the proliferation of resonant sites at *arbitrarily* long length scales. Here, we say that two sites i and j to be in resonance when the parameters J_i^j, h_i and h_j satisfy $J_i^j > \left|h_i - h_j\right|$. Let the probability of a site in resonance with a site i, at a distance R, be $P(R)$. Assuming a constant density of states n, the characteristic level spacing in a shell of width dR is $\Delta \sim \frac{1}{n\, dR}$, while the hopping strength is $J \sim \frac{1}{R^{\alpha}}$. Therefore, the number of resonances between R and $R + dR$ is $P(R)\ dR \propto \frac{J}{\Delta} \sim \frac{1}{R^{\alpha}}\, dR$. Now, the total number of sites in resonance at any length larger than R is,

$$N_{\text{res}} = \int_R^L dR'\ P(R') \sim \begin{cases} \log\left(\frac{L}{R}\right) & , \text{ for } \alpha = 1 \\ \frac{1}{R^{\alpha-1}} & , \text{ for } \alpha > 1 \\ L^{1-\alpha} & , \text{ for } \alpha < 1 \end{cases}$$

where we keep terms at leading order in system size L. Therefore, in the delocalized phase ($\alpha < 1$), the number of resonances diverge and, conversely, in the localized phase ($\alpha > 1$), the number of resonances does not scale with system size, and, hence, is negligible at the thermodynamic limit. At the critical point $\alpha = 1$ N_{res} diverges logarithmically, which suggests a phase transition.In the following, we present a more careful derivation of the above result, following Levitov [65, 66].

Let us first outline the structure of the argument. Consider an arbitrary site at r_i. Since localized or delocalized phases are controlled by resonances, we investigate the probability of a resonance with site i, $P(R,k)$, at a distance, $r > R$, where $|r - r_i| = 2^k R$. We define a resonance as when the hopping and the fields of the two sites i and j are related by $J_i^j > \left|h_i - h_j\right|$. To prove that the system is delocalized, we must show that no matter how large R is, the probability $P(R,k)$ remains finite. Conversely, to prove localization, we must show that $\exists\ R > 0$ such that $P(R,k)$ vanishes.

Let us consider two concentric one-dimensional "spheres" with radius $2^k R < |r - r_i| < 2^{k+1} R$ for a given value of k. The volume of this shell is $V(k,R) = 2^k R$. The characteristic level spacing in this shell, $\Delta(k,R)$, and the typical hopping strength, $J(k,R)$, are

$$\Delta(k,R) \sim \frac{1}{nV(k,R)}, \tag{11.2}$$

$$J(k,R) \sim \frac{1}{(2^k R)^{\alpha}}, \tag{11.3}$$

where we have assumed a constant density of states n. The typical value of the probability distribution for a resonance with site i in this shell is

$$P(k,R) \propto \frac{J(k,R)}{\Delta(k,R)} = \frac{2^k R}{(2^k R)^{\alpha}} = \left(2^k R\right)^{\epsilon}, \tag{11.4}$$

where we defined $\epsilon = 1 - \alpha$. Notice that the volume of the system is $V_{tot} = 2^L R$. There are three possible cases, that must be considered separately. In all cases, we consider the probability of *not* finding a resonance beyond a R, P_{nr}. Delocalized phases, as well as the critical point, will have a vanishing P_{nr} for large R.

- Critical Regime, $\epsilon = 0:\ P(k,R) = b$ is a constant. The probability of not finding a resonance beyond a R is $P_{nr} = \prod_{k=1}^{N} [1 - P(k,R)] = (1-b)^L \to 0$ at the thermodynamic limit. Also, the total number of sites in resonance with site i is

$$\begin{aligned} N_{res} &= \sum_{k=0}^{N} P(k,R) = (L+1)\, b \\ &\sim \log(V_{tot}). \end{aligned} \tag{11.5}$$

- Delocalized Regime, $\epsilon > 0$: $P_{nr} = \prod_{k=0}^{N} \left(1 - C\left(2^k R\right)^{\epsilon}\right) \to 0$. This can be shown as follows, choose $\epsilon = 0^+$,

$$\begin{aligned} \log\left(P_{nr}\right) &= \sum_{k=0}^{N} \log\left(1 - \left(2^k R\right)^{\epsilon}\right) \\ &= -\sum_{k=0}^{N} \frac{1}{k}\left(2^k R\right)^{\epsilon} \sim -R^{\epsilon} 2^{\epsilon L} \qquad (11.6) \\ \Rightarrow \quad P_{nr} &\sim \exp\left(-R^{\epsilon} 2^{\epsilon L}\right) \to 0. \qquad (11.7) \end{aligned}$$

  Note that, in general, the probability of a resonance $P\left(k, R\right) = 1 - P_{rn}$ grows with R for $\epsilon > 0$ indicating a delocalized regime. Consequently, the number of sites at resonance is

$$\begin{aligned} N_{res} &= \sum_{k=0}^{N} \left(2^k R\right)^{\epsilon} = R^{\epsilon} \sum_{k=0}^{N} \left(2^{\epsilon}\right)^k \\ &= R^{\epsilon} \frac{\left(1 - 2^{\epsilon(N+1)}\right)}{1 - 2^{\epsilon}} \sim R^{\epsilon} 2^{\epsilon N} \text{ for } N \gg \frac{1}{\epsilon} \\ &\propto \left(V_{tot}\right)^{\epsilon}, \qquad (11.8) \end{aligned}$$

  which diverges at the thermodynamic limit. It should also be noticed that such divergence is not extensive in volume, but instead increases with power ϵ.

- Localized Regime, $\epsilon < 0$: Similar to the delocalized regime, we set $\epsilon = 0^-$, then $P_{nr} = \prod_{k=0}^{N} \left(1 - \left(2^k R\right)^{\epsilon}\right) \sim \exp\left(R^{\epsilon}\right)$. So for large enough R, $P_{nr} \to 1$, indicating a localized phase. Equivalently, if the number of sites in resonance,

$$N_{res} \sim \text{const}, \qquad (11.9)$$

  which also points to the fact that the phase is localized, since N_{res} does not scale with system size.

Chapter 12

WEGNER FLOW EQUATIONS APPLIED TO ANDERSON TRANSITION

12.1 Disordered Wegner's Flow Equations

The flow equation technique (FET) iteratively constructs a unitary transformation that continuously diagonalizes a Hamiltonian as a function of some flow "time" Γ. Here we generalize the flow equation method introduced in Chapter 10 to the power law random banded matrices introduced in Chapter 11. Going back to the model we previously introduced in Eq. (11.1), we set the coupling constants to be functions of Γ and split it into two parts, $H_0(\Gamma)$ and $V(\Gamma)$:

$$H(\Gamma) = \sum_i h_i(\Gamma)\, c_i^\dagger c_i + \sum_{i,j} J_i^j(\Gamma)\, c_i^\dagger c_j, \tag{12.1}$$

$$= H_0(\Gamma) + V(\Gamma). \tag{12.2}$$

We also require that the Γ-dependent Hamiltonian defined in Eq (12.1) satisfies $H(\Gamma = 0) = H$ (see Eq. (11.1)) and that $H(\Gamma \to \infty)$ becomes diagonal. We work in the number basis such that $c_i^\dagger c_i$ is diagonal. Now, following Wegner [114], the canonical generator for the infinitesimal unitary transformations is defined as, $\eta(\Gamma) = [H_0(\Gamma), V(\Gamma)]$.

The Hamiltonian flows under the operation of the generator, η, which is expressed through an Heisenberg equation of motion with respect to RG time (See Eq. (10.2)). The Heisenberg equation of motion leads to the following flow equations for the couplings,

$$\frac{dJ_i^j}{d\Gamma} = -J_i^j \left(x_j^i\right)^2 - \sum_{k=1}^{N} J_i^k J_k^j \left(x_k^j - x_i^k\right), \tag{12.3}$$

$$\frac{dh_i}{d\Gamma} = -2\sum_{k=1}^{N} \left(J_k^i\right)^2 x_i^k, \tag{12.4}$$

where we have defined, $x_j^i = h_i - h_j$. The initial conditions for the couplings are $J_i^j(\Gamma = 0) = J_i^j$ and $h_i(\Gamma = 0) = h_i$. As a consequence of the Hamiltonian becoming diagonal in the limit $\Gamma \to \infty$, we have $J_i^j(\Gamma \to \infty) = 0$. The single-particle energy spectrum of the Hamiltonian is obtained from the set of fields in

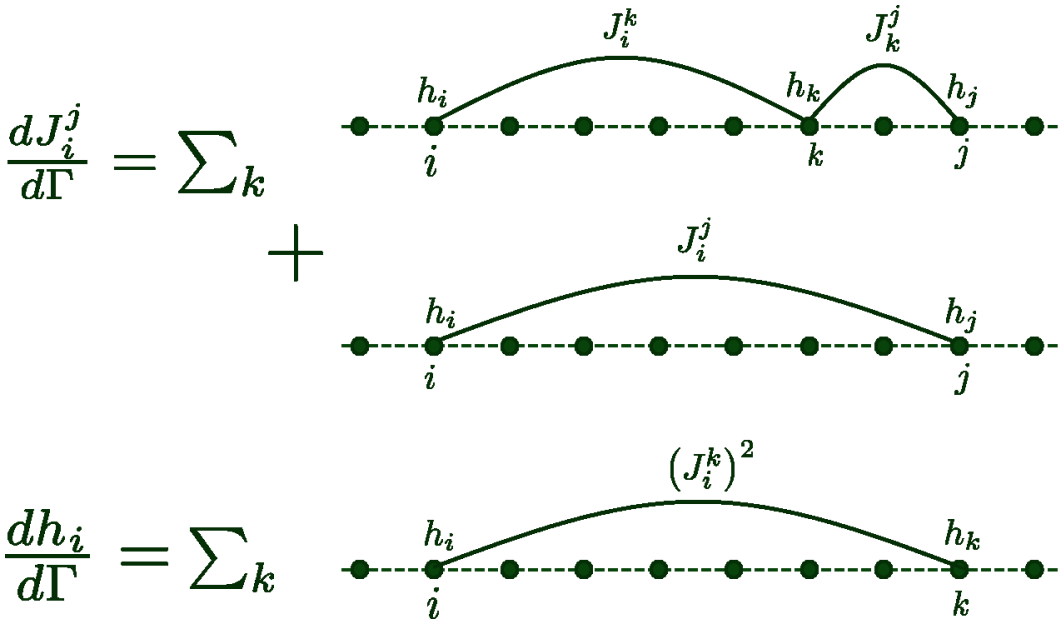

Figure 12.1: Pictorial representation of the flow equations for the hoppings and fields as calculated in Eqs. (12.3) and (12.4). All the contributions are product of three coupling constants. For the hoppings, the first contribution comes from a sum of terms of the type JJh, that is the product of two hoppings and one field, while the second contribution comes from Jhh, the product of two fields and one hopping. For the renormalization of hoppings, all contributions are of type JJh.

the end of the flow $\{h_i\,(\Gamma \to \infty)\}$. The many-body energies can be found by filling these levels. The flow equations are represented schematically in Fig. 12.1.

The flow equations can be solved numerically, by starting a chain with random couplings and evolving them numerically via Eqs. (12.3) and (12.4). In Fig. 12.2, we give a comparison of the spectrum obtained using the FE with exact diagonalization for a 5 site chain. The decay of J_i^j is controlled by the field difference, $h_i - h_j$. When the final values of h_i and h_j are close, the decay is much slower, as can be seen also be seen in the Figure.

The flow equations, Eqs. (12.3) and (12.4), also serve as an analytical tool. Next we exactly solve the flow of a two-site chain, which serves as the foundation for the strong bond RG flow (Sec. 12.2), useful to study the $\alpha > 0.5$ regime. Later, we explore the N-site problem by studying asymptotic behavior of the J-distributions under the flow equations. This reveals the universal flow of $\alpha < 0.5$ to the universal $\alpha = 0$ stable fixed point. This agrees with the phase diagram of this model, indicating that all states are in the GOE ensemble for $\alpha < 0.5$.

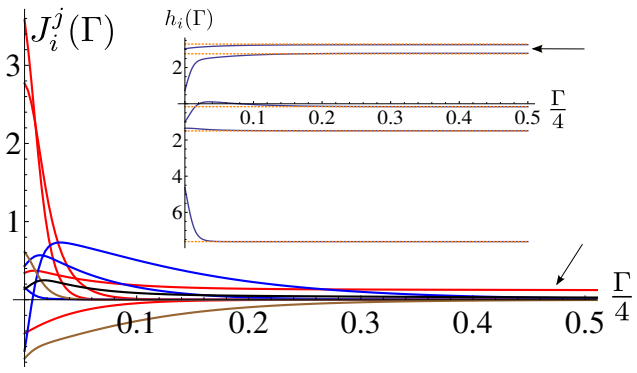

Figure 12.2: (Color online) Typical flow for the 5-site problem. The initial fields and hoppings are random variables. The distribution of hoppings is Gaussian, with a power-law decay with distance $|i-j|^{\alpha}$, $\alpha = 1$. The distinct colors represent the different distances $|i-j|$ (red, blue, brown, and black curves, in order of increasing distance). Notice that one of the red curves, indicated by the arrow, flows more slowly to zero. This is due to the fact that the decay term in the J flow is proportional to difference of the fields of the two sites connected by it [see Eq. (12.3) and the arrow in the inset curve]. Also shown in the inset is flow of fields (blue) and their asymptotic approach to the Hamiltonian eigenvalues (horizontal dashed orange lines).

Building block: Two-site solution

As a first step, let us solve the illustrative example of the two-site chain, with fields h_1 and h_2 and inter-site hopping, $J \equiv J_1^2$. It becomes convenient to define a new variable, $x = h_2 - h_1$. The flow equations, Eqs. (12.3) and (12.4), reduce to,

$$\frac{d}{d\Gamma}J(\Gamma) = -J(\Gamma)(x(\Gamma))^2, \tag{12.5}$$

$$\frac{d}{d\Gamma}x(\Gamma) = 4(J(\Gamma))^2 x(\Gamma). \tag{12.6}$$

These equations have a conserved quantity, which we denote as

$$r^2 = 4J(\Gamma)^2 + x(\Gamma)^2.$$

Defining polar coordinates, $J(\Gamma) = \frac{r}{2}\sin\theta(\Gamma)$ and $x(\Gamma) = r\cos\theta(\Gamma)$, we obtain the flow for $\theta(\Gamma)$:

$$\frac{d\theta}{d\Gamma} = -\frac{1}{2}r^2\sin 2\theta(\Gamma), \tag{12.7}$$

where the initial condition is $\theta_0 = \theta(0) = \arctan\left(\frac{2J}{x}\right)$. The solution of this equation is

$$\tan\theta(\Gamma) = \tan\theta_0 \exp\left(-r^2\Gamma\right). \tag{12.8}$$

Asymptotically, as $\Gamma \to \infty$, θ tends to zero: $\theta(\Gamma \to \infty) = 0$. The decay rate of $\tan\theta(\Gamma)$, gives us a natural RG time scale to achieve a nearly diagonal Hamiltonian:

$$\tau_\Gamma \sim \frac{1}{r^2}. \tag{12.9}$$

In this chain of two sites, the master equation for the distribution of couplings, $J(\Gamma)$ and $x(\Gamma)$, can also be exactly solved. The solution reveals that the distributions of $\log J(\Gamma)$ and $x(\Gamma)$ are correlated, what can be tracked back to the constraint that $x^2\Gamma = -\log(J)$.

It is important to note that the two-site flow gives rise to the following canonical transformation of the second-quantized creation opperators:

$$\begin{pmatrix} \tilde{c}_1 \\ \tilde{c}_2 \end{pmatrix} = \begin{pmatrix} \cos\alpha_{12} & \sin\alpha_{12} \\ -\sin\alpha_{12} & \cos\alpha_{12} \end{pmatrix} \begin{pmatrix} c_1 \\ c_2 \end{pmatrix}, \tag{12.10}$$

where $\alpha_{12} = \mathrm{sgn}(Jx)\frac{\theta_0}{2}$.

N-site problem

Now we consider the full coupled flow equations for the N-site problem. Let us start by defining new hopping variables, $G_i^j = J_i^j l^{-\alpha}$, where $l = |i-j|$. We consider the initial distributions for the couplings J ($l = |j-i|$) to have a variance that scales with length as $\sigma_J^2(l) \sim l^{-2\alpha}$, while the $G \equiv G_i^j$ distributions are distance independent. Without loss of generality, assume that $j > i$. The FE in Eq. (12.3) rewritten in terms of G is

$$-\frac{dG}{d\Gamma} = \sum_{k=1}^{N} X_k \left[\frac{l}{|k-i|\,|j-k|}\right]^\alpha + G\left(x_j^i\right)^2, \tag{12.11}$$

$$= \Delta(l) + G(x(l))^2 \tag{12.12}$$

where $X_k = G_i^k G_k^j \left(x_k^j - x_i^k\right)$. There are two terms in Eq. (12.11). The term $G(x(l))^2$ is responsible for the decay in the magnitude of G, and $\Delta(l)$ acts as a random-source term that generates hoppings distributions with changing power laws, which modifies the distribution of G. In order to unveil how this process happens, we ignore the decay term for a moment and consider the scaling of the variance of the distribution of $\Delta(l)$ at long distances, $\sigma_\Delta(l)$. Let us assume that X_k is a scale-independent uncorrelated random variable, $\langle X_k X_{k'}\rangle = \left\langle X^2\right\rangle \delta_{kk'}$. With this assumption, we end up with

$$\sigma_{\Delta}^{2}(l) = \left\langle X^{2}\right\rangle \left(\sum_{k=1;k\neq i,\ell+i}^{N} \frac{l^{2\alpha}}{|k-i|^{2\alpha}\,|l-(k-i)|^{2\alpha}} \right), \tag{12.13}$$

$$\approx \left\langle X^{2}\right\rangle l^{2\alpha} \int_{1}^{l} \frac{dx}{x^{2\alpha}\,(l-x)^{2\alpha}} + \left(\int_{1}^{i-1} + \int_{1}^{N-j} \right) \frac{dx}{x^{2\alpha}\,(l+x)^{2\alpha}}. \tag{12.14}$$

The integral is dominated by possible divergences at $x = 0$ and $x = l$. Consider first $\alpha < \frac{1}{2}$. It is clear that we can completely scale out l,

$$\int_{1}^{l} \frac{dx}{x^{2\alpha}\,(l-x)^{2\alpha}} \sim l^{1-4\alpha} \int_{\frac{1}{l}}^{1} \frac{dx}{x^{2\alpha}\,(1-x)^{2\alpha}} \propto l^{1-4\alpha},$$

and, therefore, we expect $\sigma_{\Delta}^{2}(l) \propto l^{1-2\alpha}$. In contrast, at $\alpha = \frac{1}{2}$, the variance is logarithmically dependent in l, $\sigma_{\Delta}^{2}(l) \propto \log l$, hinting a critical behavior. Finally, we note that for the case of $\alpha > \frac{1}{2}$, the variance is independent of the length scale, $\sigma_{\Delta}^{2}(l) \sim \text{const.}$

It is apparent from the scaling of the source terms that the l-dependence of the variance of the hopping distribution gets modified throughout the flow, since $l^{-2\alpha} \to l^{1-4\alpha}$ if $\alpha < 1/2$. The point $\alpha^{*} = 1/2$ is a scaling fixed point, which is also confirmed by the sub-leading logarithmic dependence of the variance of the source terms, σ_{Δ}^{2}. Considering parameters slightly away from this fixed point, $\alpha = \alpha^{*} - \epsilon$, the exponent generated by the source term is such that $\alpha^{*} - 2\epsilon < \alpha$. Qualitatively, this means that as the time scale Γ increases, the source term generates distributions with smaller exponents, which become the dominant contribution at long distances. Eventually, the distribution must flow to $\alpha = 0$, since $\alpha < 0$ is physically not allowed. In the regime $\alpha > 1/2$, on the other hand, we see that the source terms have a distribution with a variance that scales as $\bar{\sigma}_{\Delta}^{2} \sim l^{-2\alpha}$. This means that the source terms do not modify the long distance ($l \to \infty$) behavior of the distribution of $J(l)$ variables.

In order to check the above argument, we numerically solve Eqs. (12.3) and (12.4). The simulations are done at chains with $N = 45$ sites, and the Γ parameter flows from $\Gamma = 0$ until $\Gamma = \Gamma_{\max}$, where $\Gamma_{\max}$ is chosen according to the disorder strength of the hoppings in such a way that at $\Gamma_{\max}$ the energies converge to a fixed value, up to machine precision. We follow the evolution of both J_{i}^{j} and h_{i} as function of Γ, for chains of $N = 45$ sites, and average the results over 100 disorder realizations.

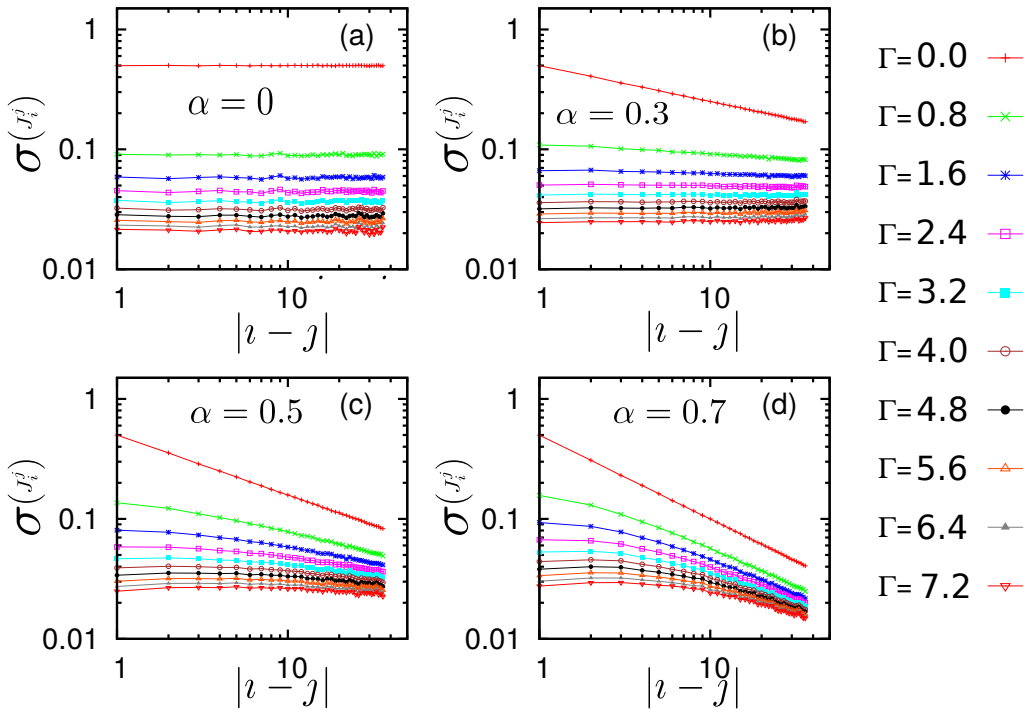

Figure 12.3: (Color Online) The standard deviation of distributions of J_i^j, $\sigma\left(J_i^j\right)$, as a function of distance $l = |i - j|$ for different RG times Γ. The simulations were run for system size $N = 45$ and averaged over 100 realizations. The initial distribution of the bonds are Gaussian with standard deviation, $\sigma\left(J_i^j\right)_{\Gamma=0} = \frac{1}{2|i-j|}$ (red straight lines in log-log scale). The fields h_i are chosen to be uniformly distributed between 0 and 1. For initial distributions with exponents $\alpha < 0.5$, the exponent changes and flows to $\alpha = 0$ as Γ increases. For exponents, $\alpha > 0.5$, the long-distance tails are not altered by the flow.

The standard deviation of the distribution $P_{l,\Gamma}(J)$, $\sigma_{J,\Gamma}(l)$, as a function of l for several RG times Γ is shown for distinct exponents in Fig. 12.3. Parts (a) and (b) of Fig. 12.3 illustrate that distributions with exponents $\alpha < \frac{1}{2}$ flow to distributions with a constant standard deviation, that is, $\sigma_{J,\Gamma}(l) \sim$ const, which corresponds to the behavior of $\alpha = 0$. At $\alpha = \frac{1}{2}$, the subleading $\log l$ contribution cannot be seen due to the limitations of the system size. In contrast, for $\alpha = 0.7$, the long distance behavior of the standard deviation is unchanged,$\sigma_J(l) \sim l^{-\alpha}$, as shown in Fig. 12.3(d), which agrees with the previous scaling analysis.

Operator Flow

Localization of single particle wavefunctions can be probed by studying the flow of single particle operators. One case of particular interest is the number operator,

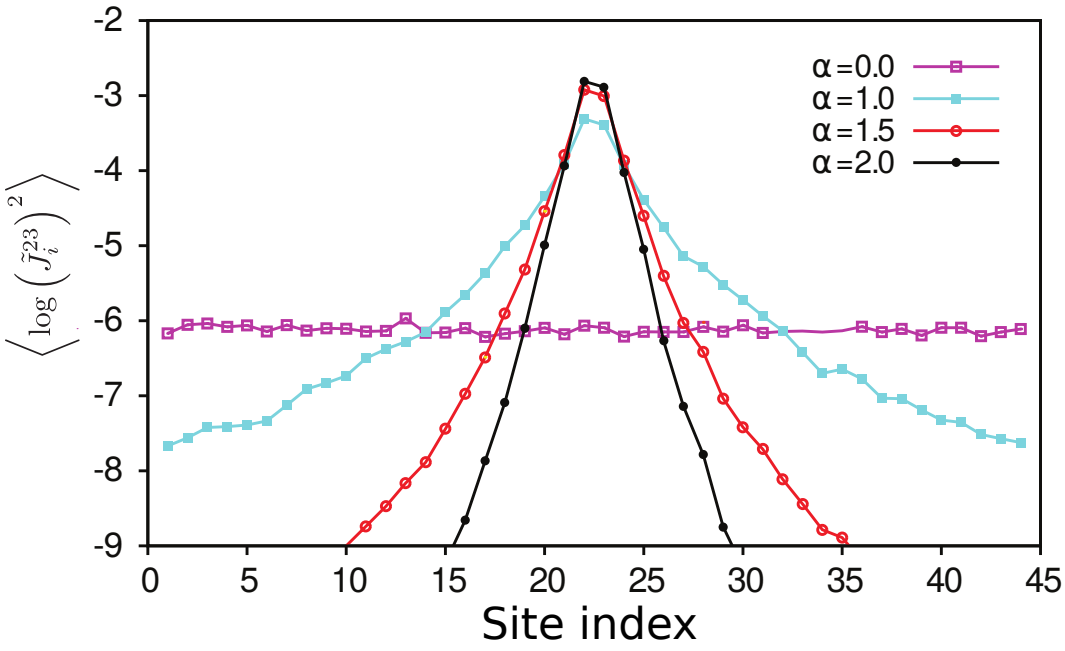

Figure 12.4: Final evolution ($\Gamma \to \infty$) of the number operator initialized in the middle of a 45-site chain, at site number 23, $\tilde{n}_{23}(\Gamma = 0) = c_{23}^\dagger c_{23}$, for some representative exponents. At $\Gamma = 0$, all $\tilde{J}_{23}^i$ are zero, and only $\tilde{h}_{23}$ is equal to one.The asymptotic values are obtained by measuring the final values of $\left(\tilde{J}_{23}^i\right)^2$ (see Eq. (12.16)). The tilde indicates the set of variables related to decomposition of the operator flow in terms of an instantaneous basis (Eq. (12.15)). Our results are averaged over 20 disorder realizations.

$c_i^\dagger c_i$, that measures the diffusive character of particles in the chain. We show next that it is possible to study the localized or extended nature of the system studying the evolution of such operators.

As the generator η evolves with Γ according to Eq. (10.4), any arbitrary operator in the Hilbert space also flows, respecting a Heisenberg equation that is analogous to Eq. (10.2). Let us consider that the number operator at a site, k, changes as a function of RG time as a result of the evolution. Writing the local density operator as, $\tilde{n}_k(\Gamma)$, the decomposition in terms of the instantaneous states of $n_k(\Gamma) = c_k^\dagger(\Gamma)\, c_k(\Gamma)$ is

$$\tilde{n}_k(\Gamma) = \sum_i \tilde{h}_i(\Gamma)\, n_j + \sum_{\langle i,j\rangle} \tilde{J}_i^j(\Gamma)\, c_i^\dagger c_j, \tag{12.15}$$

with the initial condition that a particle is started in site k, $\tilde{h}_i(\Gamma = 0) = \delta_{ik}$ and

$\tilde{J}_i^j\ (\Gamma = 0) = 0$. We find the general flow equations for the tilde variables to be

$$\frac{d\tilde{J}_i^j}{d\Gamma} = -J_i^j x_j^i \tilde{x}_j^i - \sum_{k=1}^{N} \tilde{J}_i^k J_k^j x_k^j + \sum_{k=1}^{N} J_i^k \tilde{J}_k^j \left(x_i^k\right), \tag{12.16}$$

$$\frac{d\tilde{h}_i}{d\Gamma} = -2 \sum_{k=1}^{N} J_k^i \tilde{J}_k^i x_i^k, \tag{12.17}$$

where $\tilde{x}_i^j = \tilde{h}_j - \tilde{h}_i$. As $\Gamma \to \infty$, we obtain $\tilde{n}_k$ expressed in the basis of the eigenfunctions of the Hamiltonian. Since the evolution of the operator variables is intrinsically constraint to the couplings of the Hamiltonian, their flow correlates with the flow of the set $\left\{h_i, J_i^j\right\}$.

The flow equations, Eqs. (12.16) and (12.17) can be solved numerically. We choose the initial point k to be the midpoint of the chain ($N = 22$), and plot the value of $\left(\tilde{J}_i^k\right)^2$ as a function of the distance $|i - k|$, averaged over 20 disorder realizations. The results are shown in Fig. 12.4 for different exponents α. For large exponents, $\alpha > 1$, the decay is exponential (linear in log scale), indicating that the density operator stays localized or, equivalently, that the initial particle fails to diffuse as a consequence of the localization of the wavefunctions. For small exponents, $\alpha < 1$, the operator reaches a significant value even at sites arbitrarily far from the middle, indicating the possibility of long-ranged resonances. The precise transition point cannot be found due to the restriction of the system size, but the existence of two phases can already be inferred. The precise critical point is going to be discussed later, via other numerical and analytic methods.

One of the handicaps of the flow equation technique, is that it requires the solution of $O\left(N^2\right)$ coupled differential equations. This is generally time consuming; the advantage over exact diagonalization, however, lies with the ability to extract universal features of the system directly from the flow. In the next section, we simplify the flow equations further, into a set of decoupled equations, solved sequentially. This strong-bond RG method, allows us to solve the full set of equations efficiently (although still at an $O(N^3)$ cost). It works in the regime, $\alpha > \frac{1}{2}$, where we show that our assumptions are correct and the errors accumulated are vanishing in the thermodynamic limit. This method will also allow further insights into the delocalization transition.

12.2 Strong-bond RG method

The exact two-site solution allows us to devise an RG-scheme of sequential transformations. These transformations produce an alternative scheme for constructing

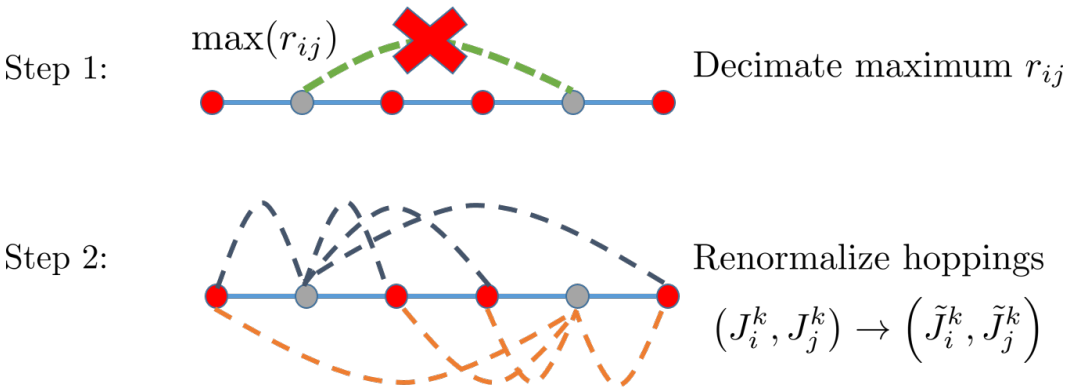

Figure 12.5: Schematic of the steps in the flow-RG method. The first part consists of finding the bond (i, j) with the maximum r_{ij}. Using an appropriate unitary, the hopping on the bond is transformed to zero. Hoppings connecting to the bond, $\left(\tilde{J}_i^k, \tilde{J}_j^k\right)$, and fields on its sites $\left(\tilde{h}_i, \tilde{h}_j\right)$, are renormalized. This procedure is iterated until all bonds are set to zero. The strong disorder allows is to make a crucial simplification: Once a bond is set to zero, we neglect its regeneration in subsequent steps. This produces a negligible error if the generated $\tilde{r}_{ik}$ and $\tilde{r}_{jk}$ are smaller than the removed r_{ij}. After $O\left(N^2\right)$ steps, where N is the system size, the Hamiltonian is diagonal.

the unitary that diagonalizes the Hamiltonian, and it can also efficiently yield an approximate solution of the flow in Eqs. (12.3) and (12.4). As we noted in Section 12.1, the FE diagonalizes the two-site problem with a characteristic RG timescale, $\tau_\Gamma \sim \frac{1}{r^2}$. This suggests an approximate solution to the N-site problem by breaking it into a sequence of two-site rotations ordered by the magnitude of r. Each rotation sets the hopping across the bond to zero. At every RG step, we transform the bond given with the largest value of r and renormalize the bonds connected to sites of the decimated bond. In Fig. 12.5, we schematically show the RG procedure.

This RG procedure can be interpreted as an ordered sequence of two-site rotations, analogous to the Jacobi algorithm used to diagonalize matrices [30]. The difference from the Jacobi rotation method is that the FE provides a natural ordering the decimations, the descending value of r.

The strong-bond RG procedure relies on the two-site transformation, Section 12.1. In practice, we employ the 2-site transformation as a Jacobi rotation on the entire Hamiltonian. The guidance provided from the flow-equations is the order in which we should pursue the transformations. We provide here the resulting RG procedure steps:

1. Find the largest non-decimated r, say $r_{\max} = r_{ij}$, between sites (i, j).

2. Compute the corresponding bond angle $\alpha_{ij} = \text{sgn}\left(J_i^j x_i^j\right) \frac{\theta_0}{2}$, where $x_i^j = h_j - h_i$ and $\theta_0 = \arctan\left|\frac{2J_i^j}{x_i^j}\right|$.

3. Set the corresponding J_i^j to zero.

4. Renormalize all bonds connected to sites i or j according to:

$$\tilde{J}_i^k = J_i^k \cos\left(\alpha_{ij}\right) + J_k^j \sin\left(\alpha_{ij}\right), \tag{12.18}$$

$$\tilde{J}_j^k = -J_i^k \sin\left(\alpha_{ij}\right) + J_j^k \cos\left(\alpha_{ij}\right). \tag{12.19}$$

5. Renormalize the fields h_i and h_j according to

$$\tilde{h}_{i,j} = \frac{1}{2}\left[H_{ij} \pm r_{\max}\text{sgn}\left(x_i^j\right)\right], \tag{12.20}$$

   where $H_{ij} = h_i + h_j$.

6. Compute the renormalized values of r, $\tilde{r}_{ik}$ and $\tilde{r}_{jk}$.

The number of steps until the Hamiltonian becomes diagonal scales with N^2, where N is the system size. In this RG proposal, each diagonal element, that converges to the approximate eigenvalue, is renormalized $O(N)$ times. This is an advantage in comparison to other proposals, like the one by Javan Mard et al.[43], for example, if one is interested in level spacing. In the latter RG proposal, sites, and not bonds, are removed from the chain. This procedure also coincides with the procedure in Ref. [91], which was developed simultaneously, and applied to many-body systems.

Universal properties from the strong-bond RG

The strong bond renormalization group approach primarily provides a new perspective from which the universal properties of disordered quantum systems could be extracted. First, the successive RG transformations suggest representing the problem as a 2-dimensional scatter plot on the $x - J$ plane. Each point in the plot corresponds to a particular bond connecting two sites, say i and j. Its 'y' value is the bond strength J_i^j, and its 'x' value is the difference of the on-site fields $\left\{h_i, h_j\right\}$, $x_i^j = h_j - h_i$. A diagonal Hamiltonian, for example, would correspond to having all points on the x_i^j axis.

The emerging picture provides a convenient way to represent the RG flow of the coupling distribution under the scheme of the previous Section, 12.2. As shown

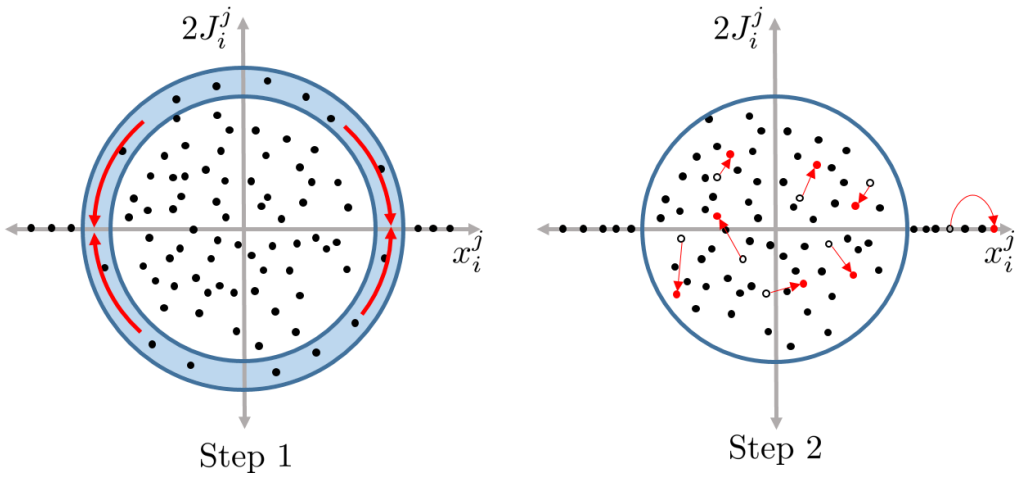

Figure 12.6: The representation strong bond RG procedure in the $x - J$ space. Each point represents a bond, and its distance from the origin is r_{ij}. the strong bond RG rotates the bonds within a large-r shell. In the first step, the bonds with largest r_i^j are rotated to the x_i^j axis. Next, the bonds connected to the decimated bond undergo a scattering via Eqs. (12.18), (12.19), and (12.20). We perform one approximation: once eliminated, a bond is not allowed to assume finite values again, and these points which lie on the x-axis beyond the r-cutoff move horizontally only.

schematically in Fig. 12.6, a decimation corresponds to rotating bonds in the largest circular shell, bringing them to the x_i^j axis. In the later steps, the points within the circle get modified according to the Eqs. (12.18), (12.19), and (12.20). Let us call it $P_\Gamma(x)$ the distribution of x_i^j at scale Γ. As one decimates all the bonds in the Hamiltonian, the final distribution of points on the x_i^j axis is obtained. The final distribution, $P_{\Gamma\to\infty}(x)$, is the distribution of the level differences for all the eigenvalues of the Hamiltonian. It is proportional to the level correlation function [79] which, in the limit $x \to 0$, is identical with the level spacing statistics. For simple localized and extended states it is given by

$$\lim_{x\to 0} P_{\Gamma\to\infty}(x) \propto \begin{cases} \text{const.}, & \text{if the phase is localized} \\ x, & \text{if the phase is extended} \end{cases} \tag{12.21}$$

Examining the long RG-time fixed points of the flow of the distributions, therefore, allows us to identify the different phases of a system, and extract their universal properties.

The $x - J$ space gives an intuitive picture for how the level-spacing distributions emerge in the two fixed points of the PBRM model : the localized and extended phases. A level repulsion, as in the extended phase, is obtained from a uniform

distribution of bonds in the $x - J$ space of Fig. 12.6. In contrast, for localized states that do not repel each other, the joint distribution has a finite range in the phase space with a length scale $\xi \ll r_{\max}$. As a simplification, we assume that the effect of the scattering, which is schematically represented in Fig. 12.6, can be ignored. First consider the case of a uniformly distributed bonds in the phase space, $P_\Gamma(J, x) \sim$ const. In this case, the number of decimations in a circular shell of radius $r_{\max}$ and width $dr\max$ is $N_{\text{dec}} \propto 2\pi r_{\max} dr_{\max}$. The number of decimations fixes the distribution of bonds at $x = r_{\max}$. Therefore, we have the distribution

$$P_\Gamma(x)\, dx \sim r_{\max} dr_{\max} \sim x dx, \tag{12.22}$$

which correctly reproduces the Wigner-Dyson statistics in the limit of small level spacing. Now, we can repeat the same analysis for $P_\Gamma(J, x) \sim e^{-J/\xi}$. In this case, the number of decimations goes as $N_{\text{dec}} \propto \xi dr_{\max}$. Consequently, we have for the distribution of level differences

$$P_\Gamma(x = r_{\max}) \sim \text{const}, \tag{12.23}$$

consistent with Poisson statistics for localized states at the small level spacing limit. We note that this analysis relies on the assumption that the scattering of the bonds do not significantly alter the marginal distribution of J. In the following, we show that this approximation is reasonable. Note that the bond distribution function in the $x - J$ space typically separates into a product distribution, with a uniform distribution on the x-axis at late stages of the flow. The J-distribution then arbitrates the level statistics: If it is uniform, we obtain Wigner-Dyson statistics, and if it is concentrated near $J = 0$, a Poisson like distribution emerges.

Strong-bond RG and the delocalization transition

Let us consider the effects of scattering on the marginal bond distribution, $P_\Gamma(J)$ of the PBRM model. Examining Eqs. (12.18) and (12.19), the evolution of the bonds J may be interpreted as a random walk with an amplitude proportional to J. To be more precise, the variance of the bonds change under scattering as

$$\sigma^2\left(\tilde{J}_i^k\right) \approx \left\langle \left(J_i^k\right)^2 \right\rangle + \left\langle \left(J_j^k\right)^2 - \left(J_i^k\right)^2 \right\rangle \sin^2 \alpha_{ij}, \tag{12.24}$$

where we have assumed that the product $J_i^k J_j^k$ is uncorrelated, $\left\langle J_i^k J_j^k \right\rangle \sim \left\langle J_i^k \right\rangle \left\langle J_j^k \right\rangle = 0$.

The change of the standard deviation is reminiscent of a one-dimensional random walk with a variable amplitude for each of the steps. Furthermore, we can assume that the two bonds that are renormalized, $J_i^k,\ J_j^k$ are of comparable range, and, thus, of comparable magnitude. The change in variance is then

$$\left|\Delta\left\langle\left(J_i^k\right)^2\right\rangle\right| \sim \left\langle\left|\left(J_i^k\right)^2-\left(J_j^k\right)^2\right|\right\rangle \sim \left\langle\left(J_i^k\right)^2\right\rangle \tag{12.25}$$

So the random change in the magnitude of the bond is proportional to the bond strength itself. Relying on this insight, we can model the flow of the J distribution as a diffusion equation with a J-dependent diffusion constant, $D\left(J\right)=D_0J^2$. Before writing the equation, we note that the sum $\sum\limits_{i,\,j,\,i\neq j}\left(J_i^j\right)^2$ must remain constant. We account for that by adding a rescaling term in the diffusion equation. The combined equation is then

$$\frac{\partial P_\Gamma\left(J\right)}{\partial\Gamma}=\frac{\partial}{\partial J}\left(D_0J^2\frac{\partial P_\Gamma\left(J\right)}{\partial J}-\gamma JP_\Gamma\left(J\right)\right), \tag{12.26}$$

where the values of the diffusion constant D_0 depend on the details of the distributions of J and x at the renormalized scale. γ is a Lagrange multiplier which is adjusted to maintain the variance of the problem constant.

The steady states of Eq. (12.26) are easy to infer. From the structure of the diffusion equation we see that the solutions must be scale invariant, i.e., power-law distributions. For any power law distribution,

$$P_\Gamma\left(J\right)\sim C\left(\Gamma\right)J^{-\beta}, \tag{12.27}$$

the exponent β would remain invariant. Furthermore, since γ is adjusted to maintain the variance of J constant, the γ rescaling term would actually make any power-law distribution a fixed point.

The discussion above makes us consider what appears to be the most crucial feature of the PRBM. The initial hopping distribution $P_{\Gamma=0}(J)$ for the power-law decaying random hopping is already a power law for almost all J's. Therefore, it is a fixed-point distribution from the start. In more detail, the initial marginal bond distribution of all bonds $P_{\Gamma=0}\left(J\right)$ for a length N chain has two distinct behaviors. At small J's, with $J<J_c=\frac{1}{N^\alpha}$ it is uniform, and for $J>J_c$, it is a power law:

$$P_{\Gamma=0}\left(J\right)\propto\begin{cases}\frac{1}{J^{1+1/\alpha}} & ,\text{for } J>J_c\\ N^\alpha & ,\text{for } J<J_c.\end{cases} \tag{12.28}$$

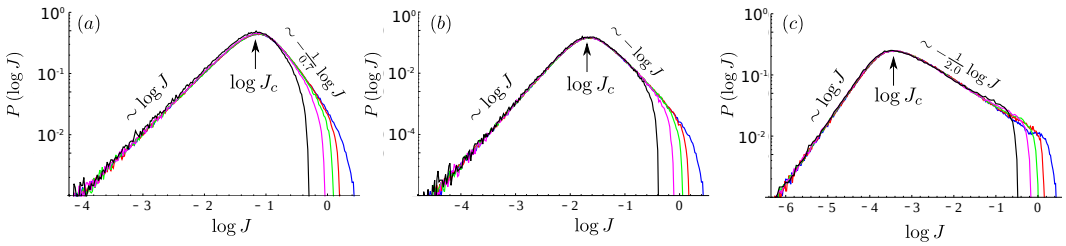

Figure 12.7: (Color Online) Marginal distribution $P_\Gamma(\log J)$ in the log scale for different RG steps Γ. From (a) to (c), we plot the evolution of the marginal distribution for exponents $\alpha = 0.7$, $\alpha = 1.0$ and $\alpha = 2.0$. Different colors represents different RG steps; $\Gamma = 1$, 1000, 2000, 3000 are represented by blue, red, green, magenta, and black, respectively. As seen from Eq. (12.28) there are two distinct regimes in the probability distribution. The crossover scale is given by J_c. Below this, $J < J_c$, $P_\Gamma(\log J) \sim \log J$ and above the scale, for $J > J_c$, $P_\Gamma(\log J) \sim -\frac{1}{\alpha}\log J$. We note that as the bonds are decimated, the behavior of the distribution below and above the crossover remains unchanged. The system has size $N = 100$ and we average over 20 disorder realizations.

This is calculated and numerically verified in Appendix A.2. Since each of the two segments is a power-law, both remain invariant. The crossover range, however, may change in the flow. Any changes of J_c during the flow, however, are bound to result in a scale-invariant change. Therefore, we assume that $J_c \sim 1/N^\alpha$ throughout the flow. This expectation is confirmed by our numerics, as discussed in the next section.

Now we can address the critical behavior of the power-law hopping problem. The fact that any power-law marginal J distribution is also marginal in the RG sense implies that the entire $\alpha > 0.5$ parameter range is critical. The transition, we show, emanates from the size dependence of the marginal distribution. The two regimes of $P_\Gamma(J)$ also imply two regimes of level spacings. After very little flow, the marginal x distribution flattens, and the full x-J bond density is

$$P(x, J) \approx c\frac{r_{\max}}{r_0}N^2 P_\Gamma(J), \tag{12.29}$$

where c is a constant, and $r_{\max}$ is the RG cutoff. As we transform away bond in the arc $r_{\max} - dr < r < r_{\max}$, and reduce $r_{\max}$, the number of bonds affected, and hence the density of level spacings is

$$\rho(x) \sim \begin{cases} \text{const}, & r > J_c \\ cr & r < J_c. \end{cases} \tag{12.30}$$

Next, we need to find out how the mean level spacing, $\bar{\delta}$, scales. For $\alpha > 1/2$, we expect $\bar{\delta}_N \sim \frac{1}{N}$, since the system's bandwidth is size independent. In Appendix A.3 we demonstrate this result using flow-equations. Alternatively, we can use the fact that the bandwidth of the Hamiltonian, W, is bounded by the norm of the off-diagonal terms, added to the disorder width w_0 :

$$W \leq w_0 + \sqrt{\int_0^N dl\ J^2\left(l\right)} \propto N^{1-2\alpha} + \text{const.},$$

where $J\left(l\right) \propto \frac{1}{l^\alpha}$, are the length-dependent hopping terms. In the thermodynamic limit, when $\alpha > 1/2$, the length-dependent correction vanishes.

The phase of the system, and the delocalization transition, is inferred from the level-spacing statistics, expressed in terms of the rescaled level spacing. We denote the rescaled level spacing as $\bar{\epsilon} = \epsilon/\bar{\delta}_N$. As Eq. (12.30) shows, level repulsion appears below the energy difference J_c. In terms of the scaled level spacing, this implies that level-repulsion sets in for rescaled energy difference

$$\bar{\epsilon}_c(N) \approx \frac{J_c}{\bar{\delta}_N} \sim N^{1-\alpha}. \tag{12.31}$$

For $\alpha > 1$, $\bar{\epsilon}_c$ vanishes in the thermodynamic limit. When $\alpha \leq 1$, the crossover point J_c is non-negligible in the thermodynamic limit. When the decimation scale reaches $J_c \sim 1/N^\alpha$, the distribution of bonds becomes uniform in the $J - x$ phase space. For $\alpha < 1$, the level repulsion emerges at $\epsilon_c \sim N^{1-\alpha}\bar{\delta}_N$, which is much larger than the average level spacing. On the other hand, for $\alpha > 1$, $\epsilon_c \ll \bar{\delta}_N$ and, therefore, the distribution of level spacings is Poissonian. The phase diagram of Fig. 11.1 emerges naturally from the strong-bond RG analysis.

The strong-bond RG picture also yields the correlation length scaling of the transition. Let us define ξ as the chain length that allows us to determine the phase of the system from the level-statistics distribution. In the delocalized phase, $\alpha < 1$, we would require $\epsilon_c(\xi) > a\bar{\delta}_\xi$, with $a > 1$ being some constant, which we could set to be $a = 2$ without loss of generality. This would imply $\xi^{1-\alpha} = a$, and

$$\xi_{del} \sim a^{1/(1-\alpha)}. \tag{12.32}$$

Similarly, in the localized phase, $\alpha > 1$, level repulsion will always emerge at some finite energy scale, as the scaling of $\epsilon_c(N)$ suggests. This scale, however, must be well below the average level spacing. We would then require $\epsilon_c(\xi) < \bar{\delta}_\xi/a$. This leads to:

$$\xi_{loc} \sim a^{1/(\alpha-1)}. \tag{12.33}$$

Together, Eqs. (12.32) and (12.33) imply:

$$\ln \xi \sim \frac{1}{|\alpha - 1|}, \tag{12.34}$$

which is consistent with the results of Ref. [81].

Numerical results

The scaling statements made above in Sec. 12.2 are confirmed numerically. In Fig. 12.7, we plot the marginal distribution $P(J)$ for different RG steps. Clearly, when $r_{\max} > J_c$, the exponent of the initial power law remains unchanged, i.e., the exponent of the power law remains fixed. In contrast, below the cutoff the bonds are uniformly distributed.

The numerical implementation of our RG method can also be used to obtain the eigenvalues of particular realizations of the problem. Before exploring the results obtained from this direct application of the RG to the spectrum, let us discuss the validity of the approach.

As we argue below, the method is reliable for $\alpha > 0.5$, it is asymptotically accurate as $\alpha \to \infty$ when all states are localized, and it fails miserably in the strongly delocalized regime, $\alpha < 0.5$. The failure in the $\alpha < 0.5$ region can be traced to the approximation that a transformed bond is not regenerated: once removed, the corrections to a transformed bond are neglected in later RG steps. This assumption is crucial for the formulation of an RG flow, since such flow rely on a decreasing scale, r. This approximation, however, breaks down when one of the renormalized bonds, $\tilde{r}_{ik}$ or $\tilde{r}_{jk}$, is greater than r_{ij}. Such 'bad decimations' correspond to cases when delocalized clusters of three or more sites should be diagonalized simultaneously. Fig. 12.8 contrasts the evolution of $r_{\max}$ during the RG flow for the different phases. For $\alpha < \frac{1}{2}$, the r values of transformed bonds increase as a function of the decimation step (Fig. 12.8a). Indeed, in this regime the two-site solution is not applicable, and the full flow equations, (12.1), which could describe macroscopically large clusters, are needed. This effect, however, is absent for $\alpha > 0.5$, including at the transition point, $\alpha = 1$. In those cases, RG steps occasionally generate a family of large r's. But these r's are promptly eliminated, and $r_{\max}$ continues to monotonically decrease, and the method is controlled.

We also considered the number of bad decimations as a function of system size. Remarkably, the fraction of bad decimations vanishes in the thermodynamic limit for all $\alpha > 0.5$, as shown in Fig. (12.9). Our plot shows a crossing at $\alpha = \frac{1}{2}$, which

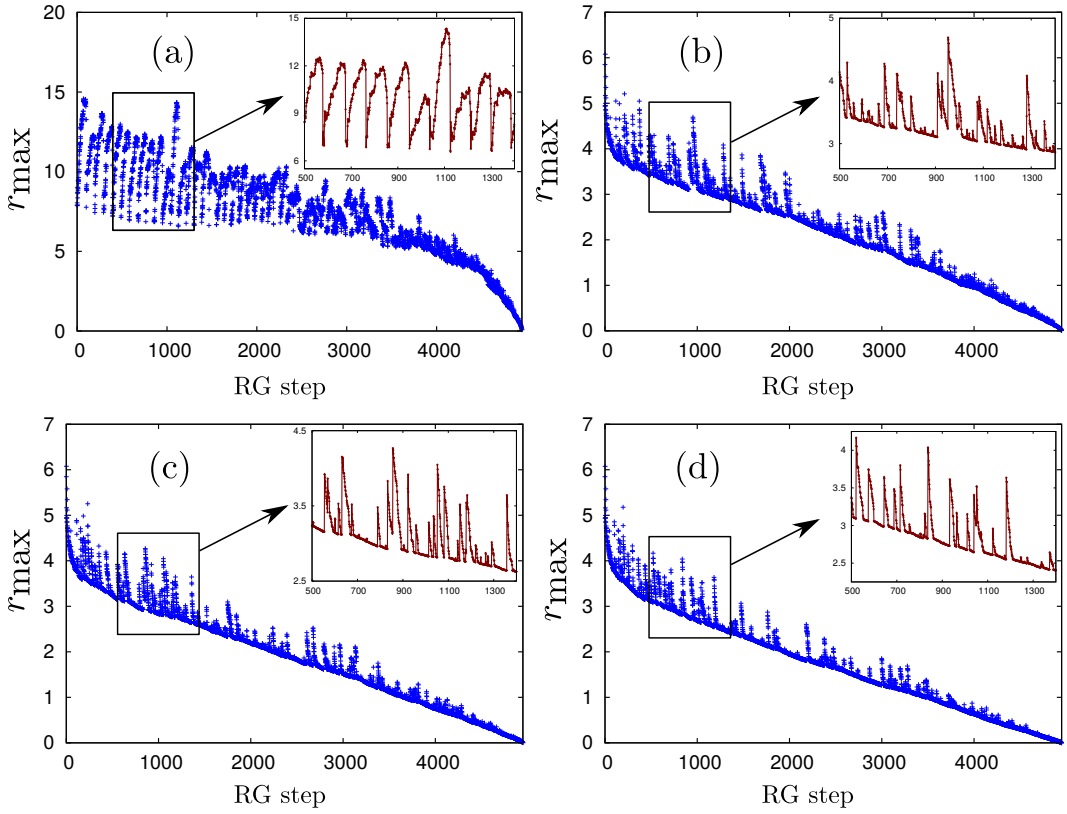

Figure 12.8: Decimated $r = r_{\max}$ as function of the RG step in a given disorder realization, for two distinct exponents, (a) $\alpha = 0.1$ and (b) $\alpha = 1.0$. The behavior of the slopes of the peaks in the curves differs significantly, as in (a) r increases in several consecutive RG steps, while in (b) a bond that is generated with r than in the removed bond is immediately removed. Notice additionally that in (b) the average decimated r decreases during the RG flow.

is the transition point from intermediate level statistics to GOE level statistics. This figure reveals that the method fails only for the strongly delocalized part of the phase diagram. The RG procedure is valid at and around the localization-delocalization critical point, $\alpha = 1$ and therefore provides an accurate description of the critically delocalized wavefunctions.

In Appendix A.1 we compare the single particle spectrum obtained from exact diagonalization and the RG procedure in the regime of applicability, $\alpha > 0.5$. We see a decent agreement between the strong-bond RG results and exact diagonalization for a variety of α values. We considered chains of 400 sites, and averaged over 500 disorder realizations. The level spacings, δ, are computed in units of their mean value. It is well known [9, 59, 82] that random matrices in the GOE ensemble have a universal distribution for the level spacing , $P(\delta) = \frac{\pi\delta}{2}\exp\left(-\frac{\pi}{4}\delta^2\right)$. In

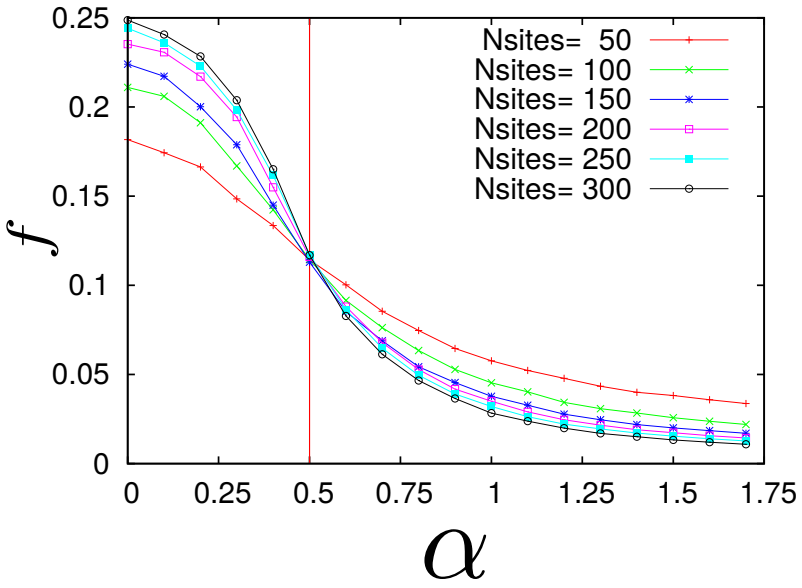

Figure 12.9: Fraction of decimations (f) that does not lower the energy scale r, in the flow RG scheme. There is a transition at $\alpha = 0.5$, indicating the failure of the flow-RG for $\alpha < 0.5$. The flow-RG has vanishing fraction of decimations in the thermodynamic limit for $\alpha > 0.5$.

contrast localized Hamiltonians exhibit no level repulsion and hence the level-spacing statistics are Poissonian, $P(\delta) = \exp(-\delta)$. As discussed in Chapter 11, the critical point of the PRBM at $\alpha = 1$, exhibit intermediate level-statistics that are neither Poisson nor Wigner-Dyson. This feature in the level-spacing statistics can be reproduced using the flow-RG, as shown in Fig. 12.10 (b) for the critical point. In contrast, for $\alpha = 5$, the system is localized at all eigenvalues, and hence the level-spacing statistics are Poisson as shown in Fig. 12.10 (d). Slightly away from the critical point at $\alpha = 0.7$, in Fig. 12.10 (a), we see that there is a deviation for small δ, in the level repulsion obtained using exact diagonalization and the RG procedure. We attribute this deviation to finite size effect, which were anticipated in Sec. 12.2. Indeed, we find strong support for all aspects of the strong-bond RG analysis from the numerical results.

We also observe some universal behavior of the distributions under the RG procedure. The exponent of decay, α for the standard deviation of the distributions remains fixed under the RG procedure. Consequently, we can study the behavior of the distributions of $G_i^j = |i - j| J_i^j$. In Fig. (12.11), we plot the distribution of these bonds, $P\left(G_i^j\right)$ as a function of the decimation step. We illustrate the case when the initial distributions of the bonds, G_i^j, was uniform. Under the RG procedure, after a

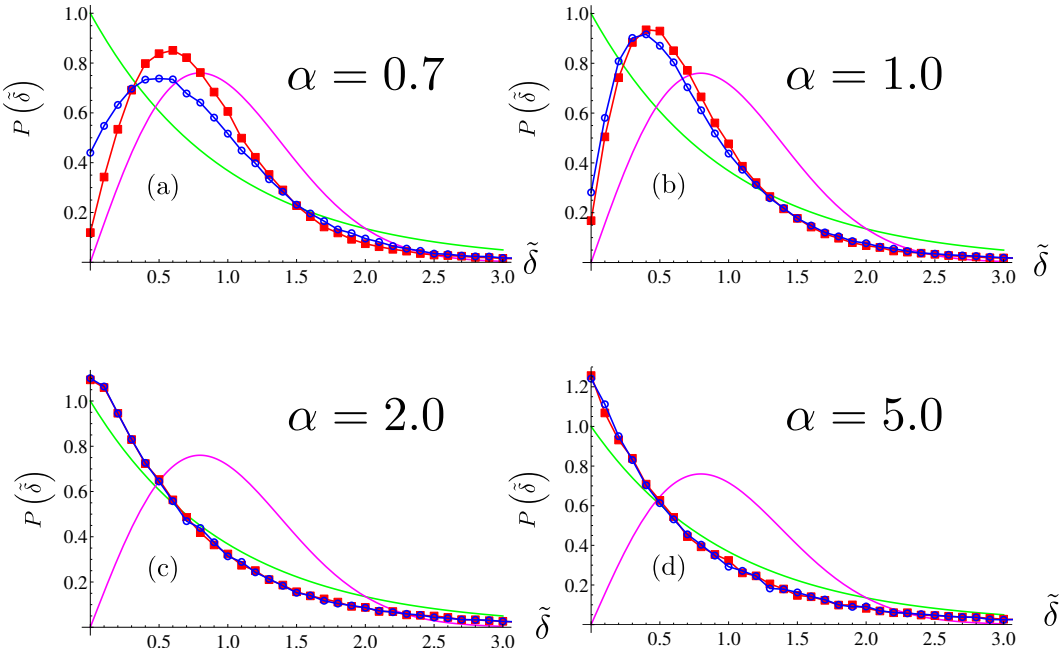

Figure 12.10: Level spacing comparison for eigenvalues obtained through flow-RG(blue circles) and exact diagonalization(red squares). (a), (b), (c), (d) correspond to exponents $\alpha = 0.7, 1, 2, 5$. For comparison, we also plot the analytical expressions for Poisson(green) and Wigner-Dyson (magenta) statistics.

large number of steps, the bonds become normally distributed. This is a feature not only at the critical point but also slightly away from it. We note that Levitov [65] predicted that the fixed point distribution of bonds is a normal distribution using the real space RG scheme. We see that the same holds true for the strong-bond RG procedure. In the following section, we gain some intuition for the RG procedure by analyzing the decimation procedure analytically.

This method also provides us the eigenfunctions of the Hamiltonian. Since each decimation corresponds to a rotation of the basis, the full unitary matrix for diagonalizaing the Hamiltonian can be obtained from the product of all the two site decimations. The eigenfunctions obtained using this method have remarkably close behavior to the exact eigenstates. In the Appendix A.4, we outline the procedure to obtain the full eigenfunctions of the system. We also calculate the critical, fractal dimensions from the IPR statistics. This indicates that the method is quite controlled and gives us the correct behavior at the critical point.

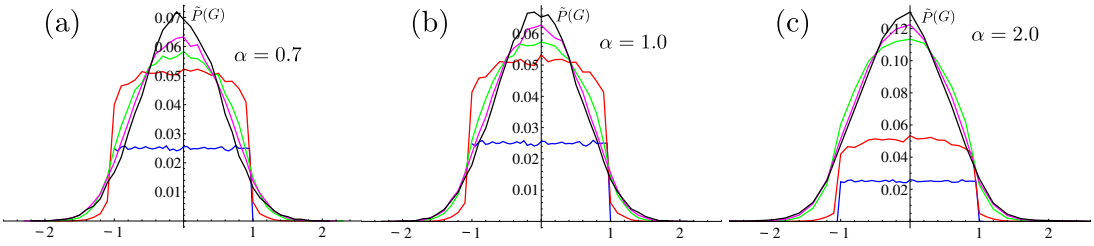

Figure 12.11: Distribution of non-decimated $G = J_i^j\,|i-j|^\alpha$, $\tilde{P}\,(G)$, as the RG flows, at RG steps $N_{steps} = 1$ (blue), 100 (red), 1000 (green), 2000 (magenta), and 3000 (black). The number of sites is $N_{sites} = 100$, and the total number of steps to diagonalize the Hamiltonian is $N_{steps} = 4950$. The exponents shown are (a)$\alpha = 0.7$, (b) $\alpha = 1.0$, (c) $\alpha = 2$. In all cases, the initial distribution of G is uniform, from -1 to 1 (blue curve). At later RG steps, the G distribution becomes Gaussian at the critical point $\alpha = 1$.

12.3 Conclusions

In this work we have shown that the Wegner's flow equations are a very useful tool to study metal-to-insulator transitions. We chose, for concreteness, the example of non-interacting systems with power-law decaying hoppings. By using the method, we were able to map out the entire phase diagram of this model. The flow equations reveal a unstable fixed point at $\alpha = \frac{1}{2}$ and an attractive fixed point at $\alpha = 0$, which corresponds to the GOE phase. Rather surprisingly, for $\alpha > \frac{1}{2}$, we observe a line of fixed points. The emergence of a localization transition is observed in the distribution of the level spacing. The flow-equation inspired RG procedure provides a simple and intuitive description of the intermediate level statistics.

The results discussed in this work can be generalized to study other systems. The particular advantage of this method is that it preserves the *full spectrum* of the Hamiltonian. This has implications in studying localization-thermalization transitions in interacting and disordered systems. Many-body localized systems are pseudo-integrable, in the sense that they have a large number of conserved charges with local support [41, 100]. There has been some recent work on studying these conserved quantities using various methods (for instance, see [91]). We argue that these conserved quantities can be obtained directly using flow equations, and therefore this method provides a promising tool to study fully-localized interacting phases.

In this work, we have also shown that the strong-bond RG procedure is suitable to study critically *delocalized* phases. We expect that a similar generalized method should be useful to study the system across the MBL-ergodic phase transition.

Yet another direction to consider are the phases of disordered and interacting systems with power-law decays. In these systems, the strong-disorder renormalization techniques developed so far fails. A strong-disorder renormalization group suitable to handle such systems is still missing. We expect the flow equation technique to be more useful in that task to study the both zero- and high- temperature phases.

Appendix A

A.1 Additional numerical results.

Numerically, we can compare the spectrum obtained from exact diagonalization and the RG procedure. In Fig. A.1, we compare all the single-particle levels from the two methods for a single disorder realization. We plot for exponents, $\alpha = 0.7$, 1.0, 2.0, and 5.0. Clearly we obtain very good agreement between the two procedures in all the cases,

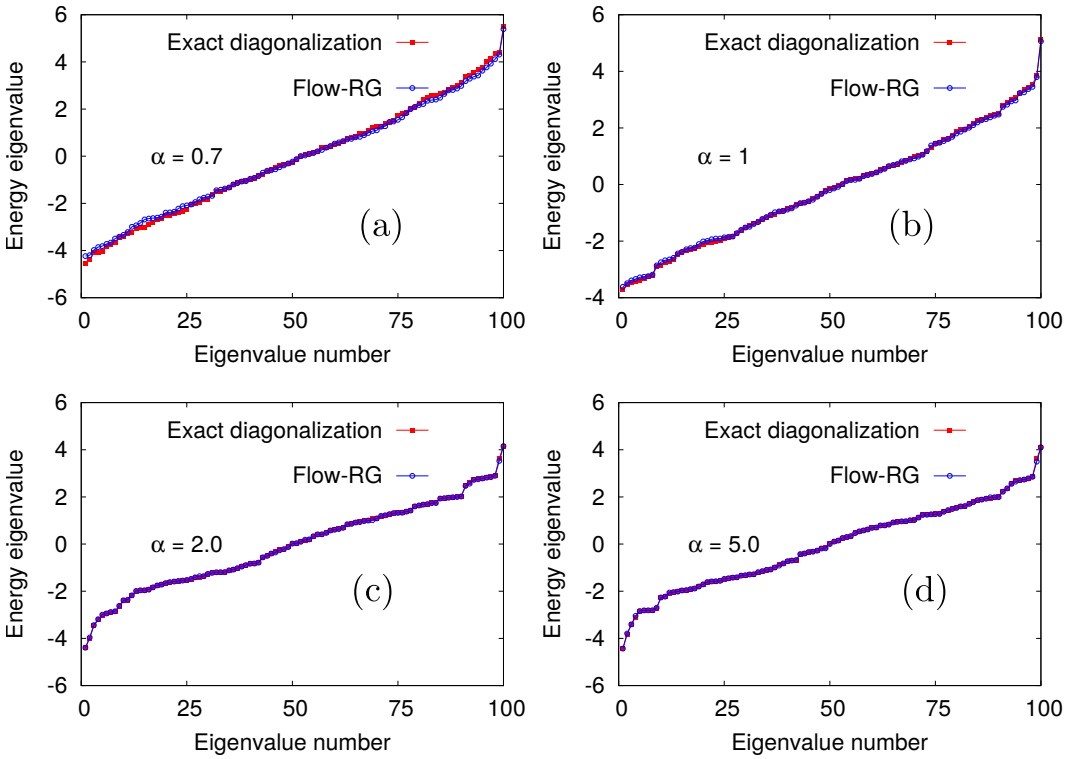

Figure A.1: Comparison of the single particle spectrum obtained from exact-diagonalization with the one obtained from the flow-RG technique. (a)-(d) in order correspond to different exponents, $\alpha = 0$, 0.7, 2.0, 5.0, respectively. In all cases, both spectra look reasonably similar. A careful inspection of the level-spacing statistics, however, reveals that the eigenvalues obtained in case (a), $\alpha = 0$, does not experience repulsion, like a delocalized phase should.

A.2 Initial Distribution of hoppings

In this Section, we derive the form of the initial marginal distribution for all hoppings, $P(J)$. Consider the distribution of all bonds connected to single site, say i, to be

$$P(J) = \frac{1}{N}\sum_{j=1}^{N-1} P_{|i-j|}\left(J_i^j\right)\delta\left(J - J_i^j\right), \tag{A.1}$$

where $P_{|i-j|}\left(J_i^j\right)$ corresponds to the distribution of bonds of a particular length. Note that the left-hand size is independent of i. We restrict ourselves to the case where each of the bonds are normally distributed. This assumption is sufficient, as we have shown in Section 12.2 that all initial distributions of hoppings J_i^j flow to normal distributions under the RG procedure. Setting $|i-j| = n$ we have

$$P_n\left(J_i^j\right) = \frac{1}{\sqrt{2\pi\sigma_n^2}}\exp\left(-\frac{\left(J_i^j\right)^2}{2\sigma_n^2}\right), \tag{A.2}$$

where $\sigma_n = \sigma_0/n^\alpha$. In the numerical simulations, we have set $\sigma_0 = 1$. Now we evaluate the approximate form of $P(J)$ by taking the continuum limit

$$\begin{aligned} P(J) &= \frac{1}{N}\int_0^N dx \frac{1}{\sqrt{2\pi}}\exp\left(-\frac{J^2x^{2\alpha}}{2}\right)x^\alpha, \\ &= \frac{1}{N\sqrt{2\pi}}\int_0^N dx \exp\left(-\frac{J^2x^{2\alpha}}{2} + \alpha\ln x\right). \end{aligned} \tag{A.3}$$

We can evaluate Eq. (A.3) using the saddle point approximation. The saddle point for the function $f(x) = -\frac{J^2x^{2\alpha}}{2} + \alpha\ln x$ is given by the condition $f'(x) = 0$, that is, $x = J^{-1/\alpha}$. This is a maximum as evidenced by $f''\left(x = J^{-1/\alpha}\right) = -2\alpha^2/x^2 < 0$. Now, evaluating Eq. (A.3) by expanding around the saddle point, we obtain

$$\begin{aligned} P(J) &= \frac{\exp\left(-\frac{1}{2}\right)}{N\sqrt{2\pi}J}\int_0^N dx \exp\left(-2J^{\frac{2}{\alpha}}\alpha^2\left(x - J^{-\frac{1}{\alpha}}\right)^2\right) \\ &\sim \frac{\exp\left(-\frac{1}{2}\right)}{4N\alpha\sqrt{2\pi}J^{1+\frac{1}{\alpha}}}, \end{aligned} \tag{A.4}$$

where in the second step we used the limit of large N, to approximate $\mathrm{erf}\left(N\alpha\sqrt{2}J^{\frac{1}{\alpha}}\right) \approx 1$. Ultimately, the distribution of the bonds becomes

$$P(J) = \frac{C_\alpha}{J^{1+\frac{1}{\alpha}}}. \tag{A.5}$$

The validity of the saddle point introduces a finite-size cutoff, dependent on the system size N. For the saddle-point approximation to be valid, we require $J^{-1/\alpha} <$

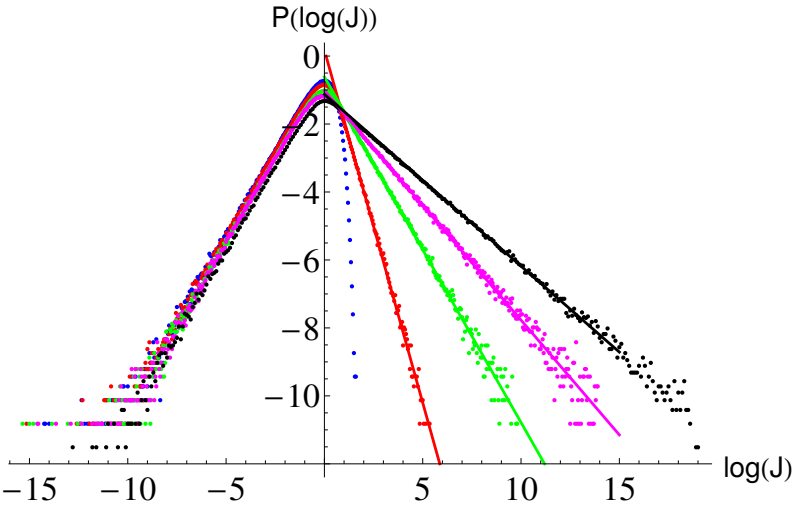

Figure A.2: Probability distribution $\log P_{\log}(y)$, of couplings connected to an arbitrary test site, in log scale. The distributions have been shifted horizontally so that the maximum of all the curves are located at $y = 0$. For $y < 0$, the uniform part of the distribution $P(J)$, corresponding to $\log P_{\log}(y) \sim -y$. For $y > 0$, the angular coefficient, expected to result in $\frac{1}{\alpha}$, gives -2.07 ($\alpha = \frac{1}{2}$, red), -1.01 ($\alpha = 1$, purple) and -0.51 ($\alpha = 2$, black). The blue line corresponds to $\alpha = 0$, where the saddle point approximation fails (see main text for details).

N, which means it fails for $J < J_{\text{cutoff}} \equiv \frac{1}{N^{\alpha}}$. For, the bonds below J_{cutoff} we set $J = 0$. The distribution becomes uniformly distributed,

$$\begin{aligned} P(J) &\approx \frac{1}{N}\int_0^N dx \frac{1}{\sqrt{2\pi}} x^{\alpha}, \\ &= \frac{N^{\alpha}}{(\alpha+1)\sqrt{2\pi}}. \end{aligned} \tag{A.6}$$

An example of the distribution $P(J)$ is given in Fig.A.2, where we consider a site connected to 100 neighbors (average over 70 realizations). Working in log scale, we find the following behavior of $\log P_{\log}(y)$,

$$\log P_{\log}(y) \sim \begin{cases} y & , y < 0 \\ -\frac{y}{\alpha} & , y > 0 \end{cases}, \tag{A.7}$$

where we have also shifted the distribution so that the crossover point is at $y = 0$.

We note that the calculation done here is approximate. The distribution clearly is incorrect in the limit of $\alpha \to 0$ and $\alpha \to \infty$. In the limit $\alpha \to 0$, the saddle point calculation is not trustworthy, while in the limit $\alpha \to \infty$ the continuum approximation done to Eq. (A.1) is no longer valid. We have also obtained the marginal

distribution to bonds connected to a single site, i. We expect this distribution to be identical to the full distribution of all bonds in a finite chain of size N, where N is large.

A.3 Effect of hoppings on bandwidth

In light of the fact that the power law exponent of the distribution of J_i^j does not flow, we rewrite its evolution as

$$J_i^j(\Gamma) = C_0^i f_\Gamma\left(x_i^j\right) \frac{1}{|i-j|^\alpha}, \tag{A.8}$$

where C_0^i is a random number and $f_\Gamma\left(x_i^j\right)$ takes into account effects of the x variables into the J evolution. At the starting point, $f_{\Gamma=0}\left(x_i^j\right) = 1$. The equation for the evolution of $f_\Gamma(x)$ follows from Eq. 12.4

$$\frac{df_\Gamma}{d\Gamma}(x) = -x^2 f_\Gamma(x), \tag{A.9}$$

whose solution is $f_\Gamma(x) = e^{-\Gamma x^2}$. Going back to the evolution of h_i, we compute $\Delta h_i = h_i(\infty) - h_i(0)$, which represents the effects of hoppings in the final fields - which are the energy levels,

$$\Delta h_i \approx N^{1-2\alpha} \frac{1}{2\Gamma} \int^{\frac{1}{N^\alpha}} e^{-\Gamma x^2} \tag{A.10}$$

$$\sim N^{1-2\alpha} \log N. \tag{A.11}$$

If $\alpha \leq \frac{1}{2}$, the bandwidth diverges, while at $\alpha > \frac{1}{2}$ it stays of $O(1)$. This is the result quoted in the main text.

A.4 Wavefunction and IPR from RG

In this section, we discuss the properties of the eigenfunctions obtained form the RG procedure. The RG procedure, performs a rotation of the basis states at each decimation step. Let the set of eigenfunctions of the Hamiltonian be, $\psi_k(i)$, where i denotes the site index and k the eigenfunction label. We define a function for the intermediate RG steps, $\psi_k^m(i)$, where m denotes the decimation steps. The initial condition before any decimation steps is chosen as, $\psi_k^0(i) = \delta_{ik}$. The eigenfunctions from the RG procedure are obtained at the end of all the steps, $\psi_k^{N_{\text{tot}}}(i) = \psi_k(i)$. Now, consider at a particular decimation step, m, the bond between sites(i, j),

is decimated. As discussed in Section 12.2, the corresponding rotation angle is $\alpha_{ij} = \frac{1}{2}\text{sgn}\left(J_i^j x_i^j\right) \text{atan}\left|\frac{2J_i^j}{x_i^h}\right|$. In this step, all the intermediate functions, $\psi_k^m(i)$ are modified according to,

$$\psi_k^{m+1}(i) = \cos\left(\alpha_{ij}\right)\psi_k^m(i) + \sin\left(\alpha_{ij}\right)\psi_k^m(j), \tag{A.12}$$

$$\psi_k^{m+1}(j) = -\sin\left(\alpha_{ij}\right)\psi_k^m(i) + \cos\left(\alpha_{ij}\right)\psi_k^m(j). \tag{A.13}$$

We can obtain the approximate IPR. We plot the comparison of the IPR obtained from the RG procedure and exact diagonalization in the Figure. The IPR obtained from the RG reproduces the critical behavior [21] when the exponent, $\alpha = 1$. The IPR scales as $P_2 = \int_r |\psi(r)|^4 \sim L^{-D_2}$ where $D_2 = 0$ for localized states, $D_2 = d$ for GOE extended states and $D_2 < d$ for critical states. Furthermore, at the critical point, the distribution $\log(P_2)$ is postulated to only shift and not change shape as a function of system size. We can obtain a scaling collapse by making the appropriate rescaling , $\log P_2 \to \log P_2 + D_2 \log N$.

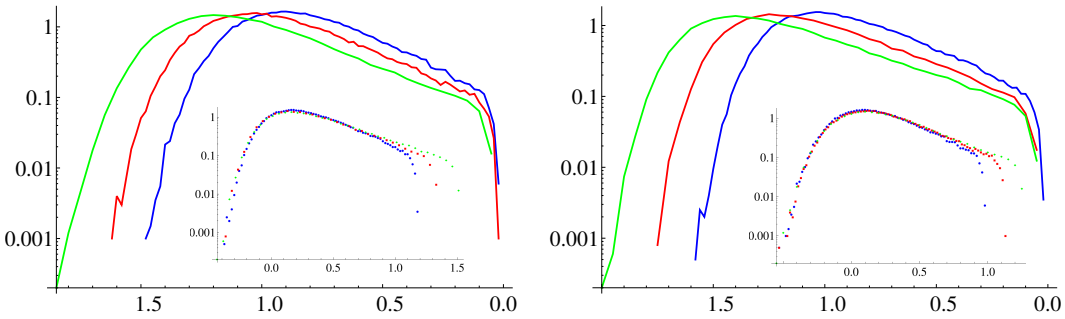

Figure A.3: Finite size scaling of the IPR for different system sizes $L = 100$ (blue), $L = 200$ (red) and $L = 400$ (green), obtained from (a) the proposed RG procedure and (b) exact diagonalization. The data is taken for the critical point, $\alpha = 1$, for different system sizes, $N = 100$ (blue), $N = 200$ (red), $N = 400$ (green). The fractal dimensions are $d_2 = 0.5$ for the RG case (a), and $d_2 = 0.6$ for the case of exact diagonalization (b).

BIBLIOGRAPHY

[1] E. Abrahams et al. "Scaling Theory of Localization: Absence of Quantum Diffusion in Two Dimensions". In: *Phys. Rev. Lett.* 42 (10 Mar. 1979), pp. 673–676. DOI: 10.1103/PhysRevLett.42.673.

[2] Kartiek Agarwal, Eugene Demler, and Ivar Martin. "$1/f^{\alpha}$ noise and generalized diffusion in random Heisenberg spin systems". In: *Phys. Rev. B* 92 (18 Nov. 2015), p. 184203. DOI: 10.1103/PhysRevB.92.184203.

[3] Alexander Altland and Martin R. Zirnbauer. "Nonstandard symmetry classes in mesoscopic normal-superconducting hybrid structures". In: *Phys. Rev. B* 55 (2 Jan. 1997), pp. 1142–1161. DOI: 10.1103/PhysRevB.55.1142.

[4] P. W. Anderson. "Absence of Diffusion in Certain Random Lattices". In: *Phys. Rev.* 109 (5 Mar. 1958), pp. 1492–1505. DOI: 10.1103/PhysRev.109.1492.

[5] Y. Y. Atas et al. "Distribution of the Ratio of Consecutive Level Spacings in Random Matrix Ensembles". In: *Phys. Rev. Lett.* 110 (8 Feb. 2013), p. 084101.

[6] Joseph E. Avron and Ruedi Seiler. "Quantization of the Hall Conductance for General, Multiparticle Schrödinger Hamiltonians". In: *Phys. Rev. Lett.* 54 (4 Jan. 1985), pp. 259–262. DOI: 10.1103/PhysRevLett.54.259.

[7] Jens H. Bardarson, Frank Pollmann, and Joel E. Moore. "Unbounded Growth of Entanglement in Models of Many-Body Localization". In: *Phys. Rev. Lett.* 109 (1 July 2012), p. 017202. DOI: 10.1103/PhysRevLett.109.017202.

[8] D.M. Basko, I.L. Aleiner, and B.L. Altshuler. "Metal-insulator transition in a weakly interacting many-electron system with localized single-particle states". In: *Annals of Physics* 321.5 (2006), pp. 1126–1205. DOI: http://dx.doi.org/10.1016/j.aop.2005.11.014.

[9] C. W. J. Beenakker. "Random-matrix theory of quantum transport". In: *Rev. Mod. Phys.* 69 (3 July 1997), pp. 731–808. DOI: 10.1103/RevModPhys.69.731.

[10] B. Andrei Bernevig, Taylor L. Hughes, and Shou-Cheng Zhang. "Quantum Spin Hall Effect and Topological Phase Transition in HgTe Quantum Wells". In: *Science* 314.5806 (2006), pp. 1757–1761. DOI: 10.1126/science.1133734.

[11] Thomas Bilitewski and Nigel R. Cooper. "Scattering Theory for Floquet-Bloch States". In: *arXiv:1410.5364* (2014).

[12] C. Dasgupta and S.-k. Ma. "Low-temperature properties of the random Heisenberg antiferromagnetic chain". In: *Phys. Rev. B* 22 (1980), p. 1305. DOI: 10.1103/PhysRevB.22.1305.

[13] A. H. Castro Neto et al. “The electronic properties of graphene”. In: *Rev. Mod. Phys.* 81 (1 Jan. 2009), pp. 109–162. DOI: 10.1103/RevModPhys.81.109.

[14] J T Chalker and P D Coddington. “Percolation, quantum tunnelling and the integer Hall effect”. In: *Journal of Physics C: Solid State Physics* 21.14 (1988), p. 2665.

[15] Yidong Chong. “Optical devices: Photonic insulators with a twist”. In: *Nature* 496 (Apr. 2013), pp. 173–174. DOI: 10.1038/496173a.

[16] Luca D’Alessio and Marcos Rigol. “Long-time behavior of isolated periodically driven interacting lattice systems”. In: *Phys. Rev. X* 4 (2014), p. 041048.

[17] Hossein Dehghani, Takashi Oka, and Aditi Mitra. “Dissipative Floquet Topological Systems”. In: *Phys. Rev. B* 90 (2014), p. 195429.

[18] Hossein Dehghani, Takashi Oka, and Aditi Mitra. “Out of equilibrium electrons and the Hall conductance of a Floquet topological insulator”. In: *arXiv:1412.8469* (2014).

[19] Pierre Delplace, Álvaro Gómez-León, and Gloria Platero. “Merging of Dirac points and Floquet topological transitions in ac-driven graphene”. In: *Phys. Rev. B* 88 (24 Dec. 2013), p. 245422. DOI: 10.1103/PhysRevB.88.245422.

[20] Freeman J. Dyson. “Statistical Theory of the Energy Levels of Complex Systems. I”. In: *Journal of Mathematical Physics* 3.1 (1962), pp. 140–156. DOI: http://dx.doi.org/10.1063/1.1703773.

[21] F. Evers and A. D. Mirlin. “Fluctuations of the Inverse Participation Ratio at the Anderson Transition”. In: *Phys. Rev. Lett.* 84 (16 Apr. 2000), pp. 3690–3693. DOI: 10.1103/PhysRevLett.84.3690.

[22] Ferdinand Evers and Alexander D. Mirlin. “Anderson transitions”. In: *Rev. Mod. Phys.* 80 (4 Oct. 2008), pp. 1355–1417. DOI: 10.1103/RevModPhys.80.1355.

[23] Aaron Farrell and T. Pereg-Barnea. “Edge State Transport in Floquet Topological Insulators”. In: *arXiv:1505.05584* (2015).

[24] Aaron Farrell and T. Pereg-Barnea. “Photon Inhibited Topological Transport in Quantum Well Heterostructures”. In: *arXiv:1505.05578* (2015).

[25] L. E. F. Foa Torres et al. “Multiterminal Conductance of a Floquet Topological Insulator”. In: *Phys. Rev. Lett.* 113 (2014), p. 266801.

[26] Liang Fu, C. L. Kane, and E. J. Mele. “Topological Insulators in Three Dimensions”. In: *Phys. Rev. Lett.* 98 (10 Mar. 2007), p. 106803. DOI: 10.1103/PhysRevLett.98.106803.

[27] F. Gao et al. “Probing the limits of topological protection in a designer surface plasmon structure”. In: *arXiv:1504.07809* (2015).

[28] Stanislaw D. Glazek and Kenneth G. Wilson. “Perturbative renormalization group for Hamiltonians”. In: *Phys. Rev. D* 49 (8 Apr. 1994), pp. 4214–4218. DOI: 10.1103/PhysRevD.49.4214.

[29] Stanislaw D. Glazek and Kenneth G. Wilson. “Renormalization of Hamiltonians”. In: *Phys. Rev. D* 48 (12 Dec. 1993), pp. 5863–5872. DOI: 10.1103/PhysRevD.48.5863.

[30] Gene H. Golub and Charles F. Van Loan. *Matrix Computations*. Johns Hopkins University Press, 2012.

[31] A. Gómez-León and G. Platero. “Floquet-Bloch Theory and Topology in Periodically Driven Lattices”. In: *Phys. Rev. Lett.* 110 (20 May 2013), p. 200403. DOI: 10.1103/PhysRevLett.110.200403.

[32] Álvaro Gómez-León, Pierre Delplace, and Gloria Platero. “Engineering anomalous quantum Hall plateaus and antichiral states with ac fields”. In: *Phys. Rev. B* 89 (20 May 2014), p. 205408. DOI: 10.1103/PhysRevB.89.205408.

[33] C. W. Groth et al. “Theory of the Topological Anderson Insulator”. In: *Phys. Rev. Lett.* 103 (19 Nov. 2009), p. 196805. DOI: 10.1103/PhysRevLett.103.196805.

[34] Zhenghao Gu et al. “Floquet Spectrum and Transport through an Irradiated Graphene Ribbon”. In: *Phys. Rev. Lett.* 107 (21 Nov. 2011), p. 216601. DOI: 10.1103/PhysRevLett.107.216601.

[35] F. D. M. Haldane. “Model for a Quantum Hall Effect without Landau Levels: Condensed-Matter Realization of the "Parity Anomaly"”. In: *Phys. Rev. Lett.* 61 (18 Oct. 1988), pp. 2015–2018. DOI: 10.1103/PhysRevLett.61.2015.

[36] B. I. Halperin. “Quantized Hall conductance, current-carrying edge states, and the existence of extended states in a two-dimensional disordered potential”. In: *Phys. Rev. B* 25 (4 Feb. 1982), pp. 2185–2190. DOI: 10.1103/PhysRevB.25.2185.

[37] Matthew B. Hastings and Terry A. Loring. “Almost commuting matrices, localized Wannier functions, and the quantum Hall effect”. In: *Journal of Mathematical Physics* 51.1, 015214 (2010).

[38] D. Hsieh et al. “A topological Dirac insulator in a quantum spin Hall phase”. In: *Nature* 452 (Apr. 2008), pp. 970–974. DOI: 10.1038/nature06843.

[39] Wenchao Hu et al. “Measurement of a Topological Edge Invariant in a Microwave Network”. In: *Phys. Rev. X* 5 (1 Feb. 2015), p. 011012. DOI: 10.1103/PhysRevX.5.011012.

[40] B. Huckestein, B. Kramer, and L. Schweitzer. "Characterization of the electronic states near the centres of the Landau bands under quantum Hall conditions". In: *Surface Science* 263 (1992), pp. 125–128.

[41] David A. Huse, Rahul Nandkishore, and Vadim Oganesyan. "Phenomenology of fully many-body-localized systems". In: *Phys. Rev. B* 90 (17 Nov. 2014), p. 174202. DOI: 10.1103/PhysRevB.90.174202.

[42] T. Iadecola, T. Neupert, and C. Chamon. "Occupation of topological Floquet bands in open systems". In: *arXiv:1502.05047* (2015).

[43] H. Javan Mard et al. "Strong-disorder renormalization-group study of the one-dimensional tight-binding model". In: *Phys. Rev. B* 90 (12 Sept. 2014), p. 125141. DOI: 10.1103/PhysRevB.90.125141.

[44] Liang Jiang et al. "Majorana Fermions in Equilibrium and in Driven Cold-Atom Quantum Wires". In: *Phys. Rev. Lett.* 106 (22 June 2011), p. 220402. DOI: 10.1103/PhysRevLett.106.220402.

[45] Gregor Jotzu et al. "Experimental realization of the topological Haldane model with ultracold fermions". In: *Nature* 515 (Nov. 2014), pp. 237–240. DOI: 10.1038/nature13915.

[46] C. L. Kane and E. J. Mele. "Z_2 Topological Order and the Quantum Spin Hall Effect". In: *Phys. Rev. Lett.* 95 (14 Sept. 2005), p. 146802. DOI: 10.1103/PhysRevLett.95.146802.

[47] Yaniv Tenenbaum Katan and Daniel Podolsky. "Modulated Floquet Topological Insulators". In: *Phys. Rev. Lett.* 110 (2013), p. 016802.

[48] K. Kawano and T. Kitoh. *Introduction to Optical Waveguide Analysis*. Wiley, New York, (2001).

[49] Stefan Kehrein. *The Flow Equation Approach to Many-Particle Systems*. Springer-Verlag Berlin Heidelberg, 2006. DOI: 10.1007/3-540-34068-8.

[50] V. Khemani et al. "On the phase structure of driven quantum systems". In: *arXiv:1508.03344* (Aug. 2015).

[51] Alexei Kitaev. "Periodic table for topological insulators and superconductors". In: *AIP Conference Proceedings* 1134.1 (2009), pp. 22–30. DOI: http://dx.doi.org/10.1063/1.3149495.

[52] Takuya Kitagawa et al. "Topological characterization of periodically driven quantum systems". In: *Phys. Rev. B* 82 (23 2010), p. 235114.

[53] Takuya Kitagawa et al. "Transport properties of nonequilibrium systems under the application of light: Photoinduced quantum Hall insulators without Landau levels". In: *Phys. Rev. B* 84 (23 Dec. 2011), p. 235108. DOI: 10.1103/PhysRevB.84.235108.

[54] K. v. Klitzing, G. Dorda, and M. Pepper. "New Method for High-Accuracy Determination of the Fine-Structure Constant Based on Quantized Hall Resistance". In: *Phys. Rev. Lett.* 45 (6 Aug. 1980), pp. 494–497. DOI: 10.1103/PhysRevLett.45.494.

[55] S. Koch et al. "Size-dependent analysis of the metal-insulator transition in the integral quantum Hall effect". In: *Phys. Rev. Lett.* 67 (7 Aug. 1991), pp. 883–886. DOI: 10.1103/PhysRevLett.67.883.

[56] Markus König et al. "Quantum Spin Hall Insulator State in HgTe Quantum Wells". In: *Science* 318.5851 (2007), pp. 766–770. DOI: 10.1126/science.1148047.

[57] B Kramer and A MacKinnon. "Localization: theory and experiment". In: *Reports on Progress in Physics* 56.12 (1993), p. 1469.

[58] B Kramer and A MacKinnon. "Localization: theory and experiment". In: *Reports on Progress in Physics* 56.12 (1993), p. 1469.

[59] VE Kravtsov. "Random matrix theory: Wigner-Dyson statistics and beyond". In: *arXiv:0911.0639* (2009).

[60] Arijit Kundu, A. Fertig H., and Babak Seradjeh. "Effective Theory of Floquet Topological Transitions". In: *Phys. Rev. Lett.* 113 (23 2014), p. 236803.

[61] Arijit Kundu and Babak Seradjeh. "Transport Signatures of Floquet Majorana Fermions in Driven Topological Superconductors". In: *Phys. Rev. Lett.* 111 (13 2013), p. 136402.

[62] R. B. Laughlin. "Quantized Hall conductivity in two dimensions". In: *Phys. Rev. B* 23 (10 May 1981), pp. 5632–5633. DOI: 10.1103/PhysRevB.23.5632.

[63] Achilleas Lazarides, Arnab Das, and Roderich Moessner. "Equilibrium states of generic quantum systems subject to periodic driving". In: *Phys. Rev. E* 90 (1 July 2014), p. 012110.

[64] Achilleas Lazarides, Arnab Das, and Roderich Moessner. "Fate of Many-Body Localization Under Periodic Driving". In: *Phys. Rev. Lett.* 115 (3 July 2015), p. 030402. DOI: 10.1103/PhysRevLett.115.030402.

[65] L. S. Levitov. "Absence of Localization of Vibrational Modes Due to Dipole-Dipole Interaction". In: *EPL (Europhysics Letters)* 9.1 (1989), p. 83.

[66] L. S. Levitov. "Delocalization of vibrational modes caused by electric dipole interaction". In: *Phys. Rev. Lett.* 64 (5 Jan. 1990), pp. 547–550. DOI: 10.1103/PhysRevLett.64.547.

[67] Jian Li et al. "Topological Anderson Insulator". In: *Phys. Rev. Lett.* 102 (13 Apr. 2009), p. 136806. DOI: 10.1103/PhysRevLett.102.136806.

[68] Yantao Li et al. "Tunable Floquet Majorana fermions in driven coupled quantum dots". In: *Phys. Rev. B* 90 (12 Sept. 2014), p. 121401.

[69] N. H. Lindner, G. Refael, and V. Galitski. “Floquet topological insulator in semiconductor quantum wells”. In: *Nat. Phys.* 7 (Mar. 2011), pp. 490–495. DOI: 10.1038/nphys1926.

[70] Netanel H. Lindner et al. “Topological Floquet spectrum in three dimensions via a two-photon resonance”. In: *Phys. Rev. B* 87 (23 June 2013), p. 235131. DOI: 10.1103/PhysRevB.87.235131.

[71] Chao-Xing Liu, Shou-Cheng Zhang, and Xiao-Liang Qi. “The Quantum Anomalous Hall Effect: Theory and Experiment”. English. In: Annual Review of Condensed Matter Physics 7 (2016). Ed. by Marchetti, MC and Sachdev, S, 301–321. DOI: {10.1146/annurev-conmatphys-031115-011417}.

[72] Dong E. Liu, Alex Levchenko, and Harold U. Baranger. “Floquet Majorana Fermions for Topological Qubits in Superconducting Devices and Cold-Atom Systems”. In: *Phys. Rev. Lett.* 111 (2013), p. 047002.

[73] T. A. Loring and M. B. Hastings. “Disordered topological insulators via C * -algebras”. In: *EPL (Europhysics Letters)* 92.6 (2010), p. 67004.

[74] Andreas W. W. Ludwig et al. “Integer quantum Hall transition: An alternative approach and exact results”. In: *Phys. Rev. B* 50 (1994), pp. 7526–7552.

[75] David J. Luitz, Nicolas Laflorencie, and Fabien Alet. “Many-body localization edge in the random-field Heisenberg chain”. In: *Phys. Rev. B* 91 (8 Feb. 2015), p. 081103. DOI: 10.1103/PhysRevB.91.081103.

[76] S. -k. Ma, C. Dasgupta, and C. -k. Hu. “Random Antiferromagnetic Chain”. In: *Phys. Rev. Lett.* 43 (1979), p. 1434. DOI: 10.1103/PhysRevLett.43.1434.

[77] A. MacKinnon and B. Kramer. “One-Parameter Scaling of Localization Length and Conductance in Disordered Systems”. In: *Phys. Rev. Lett.* 47 (21 Nov. 1981), pp. 1546–1549. DOI: 10.1103/PhysRevLett.47.1546.

[78] D F Martinez. “Floquet Green function formalism for harmonically driven Hamiltonians”. In: *Journal of Physics A: Mathematical and General* 36.38 (2003), p. 9827.

[79] M.L. Mehta. *Random Matrices, Pure and Applied Mathematics*. 3rd ed. Vol. 142. Amsterdam, Netherlands: Elsevier/Academic Press, 2004.

[80] A. D. Mirlin and F. Evers. “Multifractality and critical fluctuations at the Anderson transition”. In: *Phys. Rev. B* 62 (12 Sept. 2000), pp. 7920–7933. DOI: 10.1103/PhysRevB.62.7920.

[81] Alexander D. Mirlin et al. “Transition from localized to extended eigenstates in the ensemble of power-law random banded matrices”. In: *Phys. Rev. E* 54 (4 Oct. 1996), pp. 3221–3230. DOI: 10.1103/PhysRevE.54.3221.

[82] A.Boutet de Monvel, L. Pastur, and M. Shcherbina. "On the statistical mechanics approach in the random matrix theory: Integrated density of states". English. In: *Journal of Statistical Physics* 79.3-4 (1995), pp. 585–611. DOI: 10.1007/BF02184872.

[83] Vadim Oganesyan and David A. Huse. "Localization of interacting fermions at high temperature". In: *Phys. Rev. B* 75 (15 Apr. 2007), p. 155111. DOI: 10.1103/PhysRevB.75.155111.

[84] Takashi Oka and Hideo Aoki. "Photovoltaic Hall effect in graphene". In: *Phys. Rev. B* 79 (8 Feb. 2009), p. 081406. DOI: 10.1103/PhysRevB.79.081406.

[85] Masaru Onoda, Yshai Avishai, and Naoto Nagaosa. "Localization in a Quantum Spin Hall System". In: *Phys. Rev. Lett.* 98 (7 Feb. 2007), p. 076802. DOI: 10.1103/PhysRevLett.98.076802.

[86] Arijeet Pal and David A. Huse. "Many-body localization phase transition". In: *Phys. Rev. B* 82 (17 Nov. 2010), p. 174411. DOI: 10.1103/PhysRevB.82.174411.

[87] David Pekker et al. "Hilbert-Glass Transition: New Universality of Temperature-Tuned Many-Body Dynamical Quantum Criticality". In: *Phys. Rev. X* 4 (1 Mar. 2014), p. 011052. DOI: 10.1103/PhysRevX.4.011052.

[88] Pedro Ponte et al. "Many-Body Localization in Periodically Driven Systems". In: *Phys. Rev. Lett.* 114 (2015), p. 140401.

[89] Pedro Ponte et al. "Periodically driven ergodic and many-body localized quantum systems". In: *Annals of Physics* 353 (Nov. 2014), pp. 196–204. DOI: 10.1016/j.aop.2014.11.008.

[90] A. M. M. Pruisken. "Dilute instanton gas as the precursor to the integral quantum Hall effect". In: *Phys. Rev. B* 32 (4 Aug. 1985), pp. 2636–2639.

[91] Louk Rademaker and Miguel Ortuno. "Explicit Local Integrals of Motion for the Many-Body Localized State". In: *Phys. Rev. Lett.* 116 (1 Jan. 2016), p. 010404. DOI: 10.1103/PhysRevLett.116.010404.

[92] M. C. Rechtsman et al. "Photonic Floquet topological insulators". In: *Nature* 496 (Apr. 2013), pp. 196–200. DOI: 10.1038/nature12066.

[93] N. Regnault and R. Nandkishore. "Floquet Thermalization: Symmetries and Random Matrix Ensembles". In: *arXiv:1510.07653* (Oct. 2015).

[94] Mark S. Rudner et al. "Anomalous Edge States and the Bulk-Edge Correspondence for Periodically Driven Two-Dimensional Systems". In: *Phys. Rev. X* 3 (3 July 2013), p. 031005. DOI: 10.1103/PhysRevX.3.031005.

[95] Shinsei Ryu et al. "The $\mathbb{Z}_2$ network model for the quantum spin Hall effect: two-dimensional Dirac fermions, topological quantum numbers and corner multifractality". In: *New Journal of Physics* 12.6 (2010), p. 065005.

[96] Shinsei Ryu et al. “Topological insulators and superconductors: tenfold way and dimensional hierarchy”. In: *New Journal of Physics* 12.6 (2010), p. 065010.

[97] Andreas P. Schnyder et al. “Classification of topological insulators and superconductors in three spatial dimensions”. In: *Phys. Rev. B* 78 (19 Nov. 2008), p. 195125. DOI: 10.1103/PhysRevB.78.195125.

[98] Michael Schreiber et al. “Observation of many-body localization of interacting fermions in a quasirandom optical lattice”. In: *Science* 349.6250 (2015), pp. 842–845. DOI: 10.1126/science.aaa7432.

[99] Karthik I. Seetharam et al. “Controlled Population of Floquet-Bloch States via Coupling to Bose and Fermi Baths”. In: *arXiv:1502.02664v1* (2015).

[100] Maksym Serbyn, Z. Papi ć, and Dmitry A. Abanin. “Local Conservation Laws and the Structure of the Many-Body Localized States”. In: *Phys. Rev. Lett.* 111 (12 Sept. 2013), p. 127201. DOI: 10.1103/PhysRevLett.111.127201.

[101] N.H. Shon and T. Ando. “Quantum Transport in Two-Dimensional Graphite System”. In: *Journal of the Physical Society of Japan* 67.7 (1998), pp. 2421–2429. DOI: 10.1143/JPSJ.67.2421.

[102] Juntao Song et al. “Dependence of topological Anderson insulator on the type of disorder”. In: *Phys. Rev. B* 85 (19 May 2012), p. 195125. DOI: 10.1103/PhysRevB.85.195125.

[103] Alexander Szameit and Stefan Nolte. “Discrete optics in femtosecond-laser-written photonic structures”. In: *Journal of Physics B: Atomic, Molecular and Optical Physics* 43.16 (2010), p. 163001.

[104] T. Thonhauser and David Vanderbilt. “Insulator/Chern-insulator transition in the Haldane model”. In: *Phys. Rev. B* 74 (23 Dec. 2006), p. 235111.

[105] D. J. Thouless. “Quantization of particle transport”. In: *Phys. Rev. B* 27 (10 May 1983), pp. 6083–6087.

[106] D J Thouless. “Wannier functions for magnetic sub-bands”. In: *Journal of Physics C: Solid State Physics* 17.12 (1984), p. L325.

[107] D. J. Thouless et al. “Quantized Hall Conductance in a Two-Dimensional Periodic Potential”. In: *Phys. Rev. Lett.* 49 (6 Aug. 1982), pp. 405–408. DOI: 10.1103/PhysRevLett.49.405.

[108] Paraj Titum et al. “Anomalous Floquet-Anderson Insulator as a Nonadiabatic Quantized Charge Pump”. In: *Phys. Rev. X* 6 (2 May 2016), p. 021013. DOI: 10.1103/PhysRevX.6.021013.

[109] Paraj Titum et al. “Disorder-Induced Floquet Topological Insulators”. In: *Phys. Rev. Lett.* 114 (2015), p. 056801.

[110] Gonzalo Usaj et al. “Irradiated graphene as a tunable Floquet topological insulator”. In: *Phys. Rev. B* 90 (2014), p. 115423.

[111] Ronen Vosk, David A. Huse, and Ehud Altman. “Theory of the Many-Body Localization Transition in One-Dimensional Systems”. In: *Phys. Rev. X* 5 (3 Sept. 2015), p. 031032. DOI: 10.1103/PhysRevX.5.031032.

[112] Pei Wang, Qing-feng Sun, and X. C. Xie. “Transport properties of Floquet topological superconductors at the transition from the topological phase to the Anderson localized phase”. In: *Phys. Rev. B* 90 (2014), p. 155407.

[113] Y. H. Wang et al. “Observation of Floquet-Bloch States on the Surface of a Topological Insulator”. In: *Science* 342.6157 (2013), pp. 453–457. DOI: 10.1126/science.1239834.

[114] Franz Wegner. “Flow-equations for Hamiltonians”. In: *Ann. Physik* 3.77 (1994).

[115] E. P. Wigner. “On a Class of Analytic Functions from the Quantum Theory of Collisions”. In: *Annals of Mathematics* 53.1 (1951), pp. 36–67. DOI: 10.2307/1969342.

[116] Edward Witten. “Three Lectures On Topological Phases Of Matter”. In: *arXiv:1510.07698* (2015).

[117] Yanxia Xing, Lei Zhang, and Jian Wang. “Topological Anderson insulator phenomena”. In: *Phys. Rev. B* 84 (3 July 2011), p. 035110. DOI: 10.1103/PhysRevB.84.035110.

[118] Yi-Zhuang You, Xiao-Liang Qi, and Cenke Xu. “Entanglement holographic mapping of many-body localized system by spectrum bifurcation renormalization group”. In: *Phys. Rev. B* 93 (10 Mar. 2016), p. 104205. DOI: 10.1103/PhysRevB.93.104205.

Appendix B

QUESTIONNAIRE

Appendix C

CONSENT FORM

INDEX

[1]Endnotes are notes that you can use to explain text in a document.